A SEARCH FOR $D^0 - \overline{D}^0$ MIXING IN THE SEMILEPTONIC DECAY OF $D^0 \rightarrow K^* e\nu$

by

SEAN McGEE

DISSERTATION

Submitted to the Graduate School

of Wayne State University,

Detroit, Michigan

in partial fulfillment of the requirements

for the degree of

DOCTOR OF PHILOSOPHY

2002

MAJOR: PHYSICS

Approved by:

____
Advisor **Date**

____

____

____

DEDICATION

For Kara

for everything

ACKNOWLEDGMENTS

First and foremost, I would like to thank my advisor, Dave Cinabro, for five great years. In addition to always being available and having the answer to any question at his fingertips, he has never failed to know exactly when I needed either to be gently prodded forward or simply left to my own devices. He never lost faith in my abilities, even when, and especially when, I was sure that the light at the end of the tunnel was receding instead of approaching. Simply put, Dave has set a standard as a physicist and a mentor that I will strive to attain for the rest of my career.

I would also like to thank some of the other physicists on the 3rd floor of the physics building at Wayne State University, Giovanni Bonvicini, Rene Bellwied, Claude Pruneau, and Sean Gavin, who have not only shown me what it means to be a physicist, but made me realize it's just as much pleasure as it is work. Also, I'd like to thank some of the great teachers I've had at WSU: Bill Rolnick, Talbert Stein and Paul Karchin.

Thanks also to all the people who have passed through the main office of the Physics building at WSU while I was there. Especially De Cowen for her patience in dealing with all my last minute requests.

Here's to all my fellow graduate students at Wayne State and also at Cornell: Eugene Surdutovich, Mircea Pantea, and Stan Smith without whom I would never have passed the qualifiers and especially to Jonathon Farr, without whom I probably wouldn't have passed many classes. Thanks also to Charles Plager for dragging me away from the computer terminal at regular intervals for discussions on innumerable topics.

Thanks also to all the D Mixing Group leaders that helped along the way. Namely and in chronological order only; Tony Hill, Randal Hans, and Alex Smith. Also, thanks to David Asner for his assistance with some of the finer points of a D mixing analysis. I would also like to gratefully acknowledge the effort of the CLEO and CESR staff.

Thanks to everyone in Cutter's triathlon class at Cornell for all the miles of therapy.

Thanks to my mother and father and brothers, Mike and Ryan, and Pat Ott for their constant encouragement and unwavering faith.

Also, endless amounts of love and gratitude to Angie and Rene for keeping it all in perspective and making it so much fun. There will always be a full glass for both of you at my table.

Last but never the least, I would like to thank my wife for planting the seed, nurturing it, and seeing it through to fruition. It's all because of you, Kara.

Contents

List of Figures

List of Tables

Chapter 1

Introduction

Before I discuss $D^0 - \overline{D}^0$ mixing and why it is of interest to particle physicists, I would like to introduce some of the fundamental ideas that will be used throughout this work. In doing so, it is almost unavoidable to mention the current theory that physicists believe describes the properties and relationships of the fundamental building blocks of the universe: The Standard Model.

1.1 Particle physics and the Standard Model

"Who ordered that?"[1] was I. I. Rabi's exclamation when presented with evidence of a heretofore unknown particle. This discovery of the muon called into question the way physicists believed the entire universe was ordered. Physicists, long before they were even termed as such, have wanted to know what the universe is made of. From Thales of Miletus, who considered water to be the substance from which all things arose[2], through the atomists and on down along the development of the periodic table, there is a continuous line of thought maintaining that all things we see are comprised of yet more basic constituents. Remarkably, a cycle has been repeated throughout the history of the development of physics. From the atoms that make up the water molecule, to the nucleons in the heart of the atom, to the quarks concealed therein, one generation's fundamental particles have been shown to be simply the most abundant of a large class of particles existing as compounds of a later generation's[1]. Thus Rabi's lament and the raising of doubt as to whether we are actually looking at the fundamentals or yet more composites.

The Standard Model is a collection of fundamental particles and the rules that define their interactions. The particles are broken down into two main groups; quarks and leptons. Each group contains three generations, and each generation, two flavors.

$$\underbrace{\begin{pmatrix} u \\ d \end{pmatrix}\begin{pmatrix} c \\ s \end{pmatrix}\begin{pmatrix} t \\ b \end{pmatrix}}_{quarks} \qquad \underbrace{\begin{pmatrix} \nu_e \\ e \end{pmatrix}\begin{pmatrix} \nu_\mu \\ \mu \end{pmatrix}\begin{pmatrix} \nu_\tau \\ \tau \end{pmatrix}}_{leptons}$$

The physical properties of these particles are well known and summarized in Table 1.1 and Table 1.2.

In addition to the fundamental particles, there are four fundamental forces, *strong, electromagnetic, weak,* and *gravitational*, listed in decreasing apparent strength. I use the word "apparent" because the strength of the force is really determined by a combination of the type of particles and the distance between them. This ordering, however, is standard (see Table 1.3).

Table 1.1: Summary of physical properties of quarks.

Symbol	Name	Charge	≈Mass(MeV)[3]
u	Up	$+2/3$	3
d	Down	$-1/3$	7
c	Charm	$+2/3$	1250
s	Strange	$-1/3$	130
t	Top	$+2/3$	175000
b	Bottom	$-1/3$	4200

Table 1.2: Summary of physical properties of the leptons.

Symbol	Name	Charge	≈Mass(MeV)[3]
ν_e	Electron Neutrino	0	< 0.003
e	Electron	-1	0.511
ν_μ	Muon Neutrino	0	< 0.19
μ	Muon	-1	107
ν_τ	Tau Neutrino	0	< 18.2
τ	Tau	-1	1777

For the last quarter century, the Standard Model has reigned as the theory that not only describes almost all phenomena, but has successfully predicted the outcomes of many experiments[4]. For example, the seminal achievement of the Standard Model was it's ability to allow physicists to foresee the unification of the electromagnetic and

Table 1.3: Summary of strengths and ranges of the fundamental forces.

Force	Relative Strength	Range[1]
Strong	1	$\approx 10^{-15}$
Electromagnetic	10^{-2}	long($1/r^2$)
Weak	10^{-5}	$\approx 10^{-18}$
Gravitational	10^{-39}	long($1/r^2$)

Table 1.4: Summary of physical properties of the mediators of force described in the Standard Model.

Mediator	Force	Charge	≈Mass(MeV)[3]
photon(γ)	Electromagnetic	0	0
gluon	Strong	0	0
$W^{\pm}$	Weak	± 1	80
Z^0	Weak	0	91

weak force into a single "electroweak" force[5]. Predicted around 1960, it wasn't until 1983 that the electroweak force carriers were discovered with exactly the expected properties[6, 7]. Although it can boast many successes, the Standard Model is still considered incomplete.

As of yet, the gravitational force and its interaction is not contained in the Standard Model, much to the chagrin of particle physicists. Therefore, it is not listed in Table 1.4. Also, being almost 30 orders of magnitude[8] weaker than the misleadingly-named weak force, its affects are neglected by physicists when studying the interactions of the fundamental particles at high-energy experiments. Although, at the same time, it plays a more important role by acting as a constant reminder to those same physicists that the Standard Model is an incomplete representation of the universe and keeping them in their chairs.

Of the three remaining forces, each plays a significant role in this analysis. Albeit the main contributor, the role of the electromagnetic force is relegated to the details of the creation, acceleration, detection and storage of the particles used and the data taken to study the strong and the weak forces. These contributions are described in detail in Chapter 3 so for now let's move on to the strong force.

1.2 The strong force

In addition to the properties listed in Table 1.1, each quark will carry one of three "colors"; *red, green* or *blue.* Chromodynamics, or the laws governing the strong force, details the interaction of quarks through their "color charge" much the same way electromagnetics describes the interaction between electric charges. This nomenclature is borrowed from the study of optics with the intention of being illustrative of the fact that quarks are observable only in colorless combinations. The known possibilities are combinations of two or three quarks; collectively known as hadrons. Three-quark combinations are called *baryons* and must contain one of each color: $red + green + blue =$ white or, arguably, colorless. Two-quark combinations are called *mesons* and contain a quark and an anti-quark: $red + \overline{red} =$ colorless. Some exotic combinations of six or more quarks called dibaryons, such as "strangelets", are hypothesized but are as yet unseen[9, 10].

1.3 The weak force

With the possible exception of the proton (uud)[3], all free hadrons eventually decay into combinations of lighter hadrons, leptons, and/or photons. The possible daughters in a decay depend on the force that acts as the mediator. The strong and electromagnetic forces act as mediators to hadron and photon daughters, respectively. The interactions between the forces and the particles of the Standard Model can be described by the set of vertices shown in Figure 1.1. The interesting thing to note is that the vertex describing the weak force interaction is the only one that allows for the transition of quarks to lighter quarks and leptons to lighter leptons at the vertex.

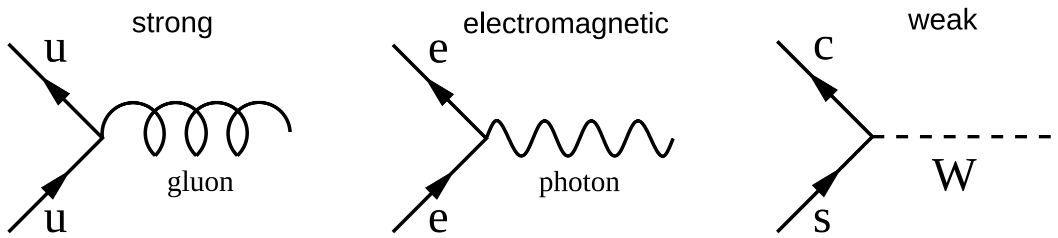

Figure 1.1: Of the three forces included in the Standard Model, only the weak force allows for quarks or leptons to change flavor and generation at the vertex.

This property of the weak force accounts for that fact that all stable matter in the universe is comprised of only first generation quarks and leptons. This is because the weak force not only couples particles within a generation but also allows for cross-generational transitions. For quarks, these couplings are summarized in the Cabibbo-Kobayashi-Maskawa(CKM) matrix.

$$\begin{pmatrix} d' \\ s' \\ b' \end{pmatrix} = \underbrace{\begin{pmatrix} V_{ud} & V_{us} & V_{ub} \\ V_{cd} & V_{cs} & V_{cb} \\ V_{td} & V_{ts} & V_{tb} \end{pmatrix}}_{CKM\ matrix} \begin{pmatrix} d \\ s \\ b \end{pmatrix} \tag{1.1}$$

In other words, the weak force does not see a simple s quark, but an s' which is a linear combination of d, s, and b.

$$s' = V_{cd}d + V_{cs}s + V_{cb}b \tag{1.2}$$

The magnitude of these matrix elements $|V_{ij}|$ is related to the quantum mechanical amplitude with which say, an "up-type" quark i will transition into the "down-type" quark j within its own generation or in another. At present, these magnitudes are uncalculable from fundamental principles and must be determined through experiment. Interestingly, these experiments have revealed a pattern in the CKM matrix. The elements on the diagonal are approximately equal to one (i.e., a quark will most likely make a transition within it's own generation) and become smaller, quite symmetrically, as they move off the diagonal[11]. The current 90% confidence limits on the magnitude of each element can be summarized as follows[3]:

$$|V_{ij}| = \begin{pmatrix} 0.9742 - 0.9757 & 0.219 - 0.226 & 0.002 - 0.005 \\ 0.219 - 0.225 & 0.9734 - 0.9749 & 0.037 - 0.043 \\ 0.004 - 0.014 & 0.035 - 0.043 & 0.9990 - 0.9993 \end{pmatrix} \tag{1.3}$$

Commonly, interactions that involve matrix elements that lie on the diagonal are considered "Cabibbo Favored" while those that involve off-diagonal elements are termed "Cabibbo Suppressed."

Chapter 2

Motivation

Before discussing $D^0 - \overline{D}^0$ mixing specifically, I would like to introduce mixing in general with the well known and well measured cases of mixing in the neutral B and neutral K meson systems. I will then move on to discuss the formalism of mixing theory.

2.1 Mixing

Mixing is the spontaneous transition of a neutral meson to its anti-particle in which the weak force and the CKM matrix mentioned in the previous chapter play fundamental roles. Mixing is possible because of the weak force mediators ability to couple to quarks across generations. This is clearly illustrated in the most frequent representation of mixing, the box diagram (Figure 2.1). Mixing has been studied for decades in the $K^0(d\overline{s})$ system and vigorously of late in the $B^0(d\overline{b})$ system. Measurements from these systems have provided not only the foundation of the Standard

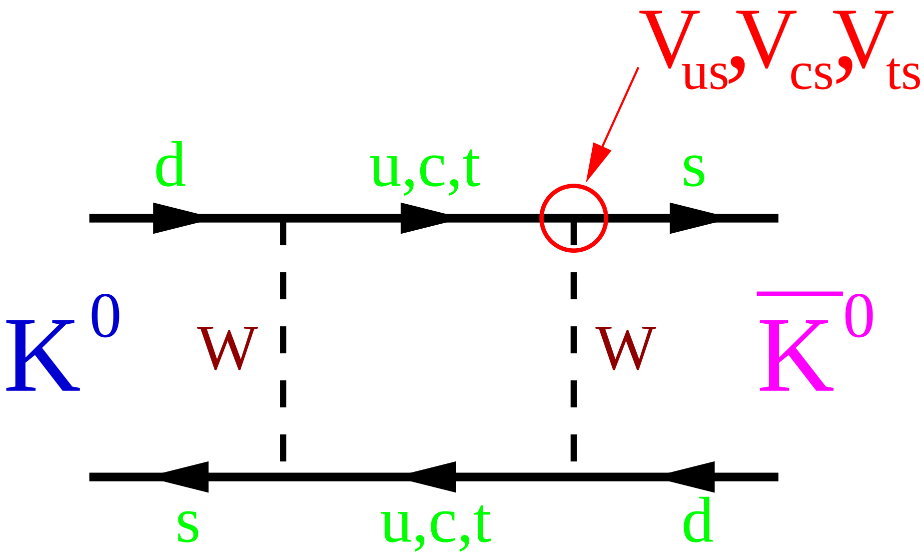

Figure 2.1: The spontaneous transformation of a $K^0(d\overline{s})$ to a $\overline{K}^0(\overline{d}s)$, or mixing, is most commonly represented with a box diagram. The frequency of mixing is calculated by summing over all values of coupling constants allowed.

Model, but have given us an indication as to why we exist to make the measurements in the first place. An explanation of the predominance of matter over anti-matter in the universe first came from the investigation of the K^0 system.

Most of the studies on spontaneous mixing have been carried out on neutral mesons of the lighter down-type quarks; $K^0(d\overline{s})$, $B^0_s(s\overline{b})$, and $B^0_d(d\overline{b})$[14, 15, 16, 17, 18]. The Standard Model reveals that the coupling of the *strange* and *bottom* quarks to the heavier *top* quark makes the transition through virtual intermediate states relatively common for these systems[19, 16, 17].

The rate of mixing, R_{mix}, is dependent on the mass of the quarks that travel around the loop in the box diagram. Therefore, when mixing was found to be large in the neutral B meson system, it was an indication that the t quark was

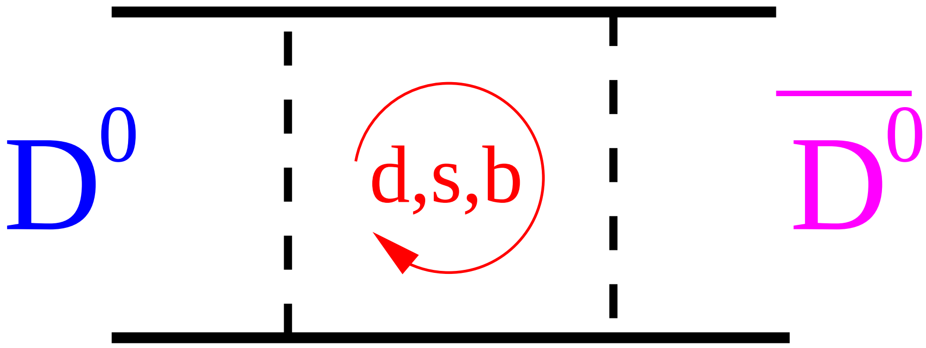

Figure 2.2: Physicists believe they know everything travelling around in the loop in the box diagram that represents $D^0 - \overline{D^0}$ mixing, therefore, the rate of these transitions in the $D^0(c\overline{u})$ system, with its coupling to the lighter *bottom* quark, is expected to be significantly lower than the rate for the $B^0(d\bar{b})$ system with its coupling to the massive *top* quark.

very massive[19].

2.2 Why is $D^0 - \overline{D^0}$ mixing interesting?

Physicists believe they know everything travelling around in the loop in the box diagram that represents $D^0 - \overline{D^0}$ mixing (Figure 2.2), therefore, the rate of these transitions in the $D^0(c\overline{u})$ system, with its coupling to the lighter *bottom* quark, is expected to be significantly lower than the rate for the $B^0(d\bar{b})$ system with its coupling to the massive *top* quark. Therefore, it is possible that evidence of a large rate of $D^0 - \overline{D^0}$ mixing is an indication of physics beyond the Standard Model.

Several theories extending the Standard Model[20, 23, 24, 25] predict $D^0 - \overline{D^0}$ mixing rates high enough to be measurable by existing experiments. To date, most of the mixing searches have been conducted with the hadronic decay channels (e.g.,

$D^0 \to K\pi$, $D^0 \to K\pi\pi^0$). Unlike the semileptonic decays, these channels have the advantage of being completely reconstructible but their final states may be reached through either mixing or a highly suppressed direct decay referred to as a doubly-Cabbibo suppressed decay (DCSD), Figure 2.3. This introduces an interference term into the mixing amplitude calculation. Therefore, analysis of the hadronic modes typically requires complex fits with multiple lifetime distributions. However, this interference term, being linearly dependent on the rate of the DCSD (see Section 2.3), is beneficial because it may provide a more prominent and more observable indication of mixing than the mixing amplitude itself [21]. The semileptonic decay channels of the D^0 are free from the interference of the DCSD modes, thus providing an unambiguous indication of mixing. I will expand on these points in the following section.

2.3 Mixing formalism

To begin the discussion of mixing, let's generalize all neutral mesons as eigenstates of flavor and then expand our wave function as a linear combination. I will take M^0 to represent any of the neutral mesons (e.g., K^0, D^0, B_s^0) and $\overline{M}^0$ the appropriate antiparticle. Considering the possible futures of these particles, the wave function of interest is some linear combination of these two states (which allows for mixing) and the possible decay states $|d\rangle$.

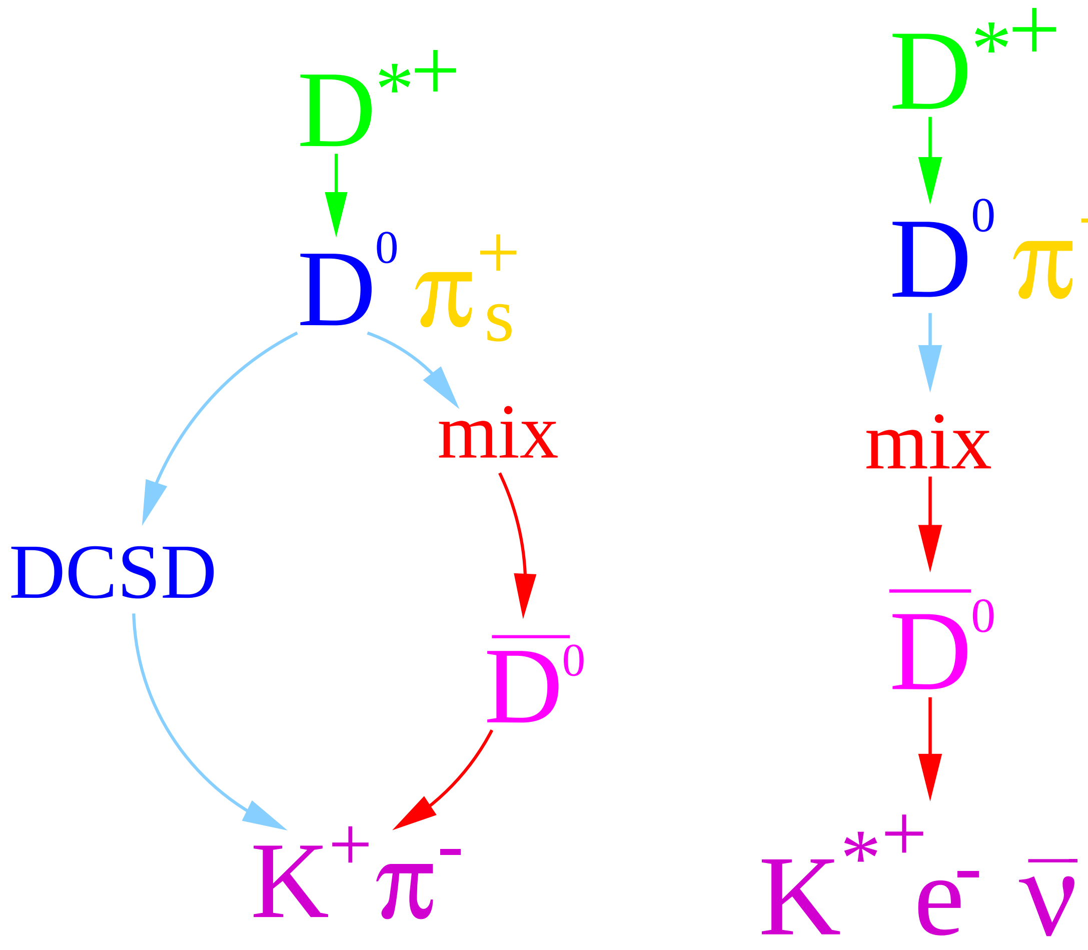

Figure 2.3: In hadronic decays of the D^0, real intermediate state paths to the same final state result in an interference term in the decay amplitude. Semileptonic decays proceed via a single path, avoiding an interference term but allowing us no knowledge of x and y; the variables that represent mixing through virtual and real intermediates, respectively.

$$|M'(t)\rangle = \alpha(t)|M^0\rangle + \beta(t)|\overline{M}^0\rangle + \sum_d \gamma_d |d\rangle \tag{2.1}$$

The complete Hamiltonian used to describe the time evolution of the neutral mesons can be written as the sum of two Hamiltonians,

$$\mathcal{H} = \mathcal{H}_{\mathbf{s,e}} + \mathcal{H}_{\mathbf{w}} \tag{2.2}$$

where $\mathcal{H}_{\mathbf{s,e}}$ contains the strong and electromagnetic interactions and $\mathcal{H}_{\mathbf{w}}$ the weak interactions. For simplicity, we will drop the last term in equation 2.1 and consider only $|M^0\rangle$ and $|\overline{M}^0\rangle$ as the basis set. This makes $\mathcal{H}$ non-Hermitian to continue to allow for the eventual decay of the meson. To allow for mixing, $\mathcal{H}_{\mathbf{w}}$ is not diagonal in this space. With these considerations, the time evolution of any neutral meson system may be written in terms of the Schrödinger equation as

$$i\frac{d}{dt}\begin{pmatrix} M^0 \\ \overline{M}^0 \end{pmatrix} = \mathcal{H}\begin{pmatrix} M^0 \\ \overline{M}^0 \end{pmatrix} = \begin{pmatrix} H_{11} & H_{12} \\ H_{21} & H_{22} \end{pmatrix}\begin{pmatrix} M^0 \\ \overline{M}^0 \end{pmatrix} \tag{2.3}$$

This can be rewritten terms of two Hermitian matrices: $\mathbf{M}$, the mass matrix and $\mathbf{\Gamma}$, the decay matrix.

$$i\frac{d}{dt}\begin{pmatrix} M^0 \\ \overline{M}^0 \end{pmatrix} = \left(\mathbf{M} - \frac{i}{2}\mathbf{\Gamma}\right)\begin{pmatrix} M^0 \\ \overline{M}^0 \end{pmatrix} \tag{2.4}$$

From the unitarity condition, the off-diagonal elements of $\mathbf{M}$ and $\mathbf{\Gamma}$ must be complex conjugates; $M_{21} = M_{12}^*$, $\Gamma_{21} = \Gamma_{12}^*$. In addition, we claim CPT invariance.

Therefore, the diagonal elements must be real and degenerate; $M_{11} = M_{22} = M$, $\Gamma_{11} = \Gamma_{22} = \Gamma$. With these constraints the full Hamiltonian simplifies to

$$\mathcal{H} = \begin{pmatrix} M & M_{12} \\ M_{12}^* & M \end{pmatrix} - \frac{i}{2} \begin{pmatrix} \Gamma & \Gamma_{12} \\ \Gamma_{12}^* & \Gamma \end{pmatrix} = \begin{pmatrix} M - \frac{i}{2}\Gamma & M_{12} - \frac{i}{2}\Gamma_{12} \\ M_{12}^* - \frac{i}{2}\Gamma_{12}^* & M - \frac{i}{2}\Gamma \end{pmatrix} \tag{2.5}$$

Let's take a moment to explore the elements of the mass and decay matrices. From a perturbation-theory analysis[26], to second order, the elements can be written

$$M_{ij} = m_0\delta_{ij} + \langle i|H_w|j\rangle + \mathcal{P}\sum_d \frac{\langle i|H_w|d\rangle\langle d|H_w|j\rangle}{m_0 - E_d} \tag{2.6}$$

$$\Gamma_{ij} = 2\pi\sum_d \langle i|H_w|d\rangle\langle d|H_w|j\rangle\delta(m_0 - E_d) \tag{2.7}$$

where m_0 is the mass of the M^0 meson and E_d is the total energy of the decay products. Delving deeper into these matrix elements reveals details about the possible mechanisms through which mixing may proceed. The mass matrix is dominated by the first term, $m_0\delta_{ij}$, which comes from the unperturbed Hamiltonian and describes the binding of the quarks into mesons. Colorful, yes, but it's the off-diagonal elements that describe mixing and are of primary interest here. Within the mass matrix, the transitions $M^0 \leftrightarrow \overline{M}^0$ are described via *virtual* (off-shell) intermediates. This is enforced by the principal-value prescription $\mathcal{P}$ summation over intermediate states $|d\rangle$ where $m_0 \neq E_d$. Within the decay matrix, the diagonal elements describe the decays $M^0 \to d$ and $\overline{M}^0 \to \overline{d}$ which are restricted to on-shell states by the factor $\delta(m_0 - E_d)$. Mixing in the decay matrix is again contained in the off-diagonal elements, but this time through *real*(on-shell) intermediate state transitions $M^0 \to d \to \overline{M}^0$. The term $\langle i|H_w|d\rangle$ refers to $\Delta S, \Delta C, \Delta B = 2$ interactions which occur in first order only outside the standard model[26].

These results are still generalized to all neutral mesons and finding the eigenstates of mixing boils down to diagonalization of $\mathcal{H}$. The resulting eigenstates are the mass (observable) eigenstates. Diagonalizing reveals the eigenvalues

$$\begin{aligned}\lambda_{1,2} &= M - \tfrac{i}{2}\Gamma \pm \sqrt{|H_{12}|^2} \\ &= M - \tfrac{i}{2}\Gamma \pm \sqrt{(M_{12}^* - \tfrac{i}{2}\Gamma_{12}^*)(M_{12} - \tfrac{i}{2}\Gamma_{12})}\end{aligned} \tag{2.8}$$

These can be rewritten as the masses and widths of the eigenstates $|M_{1,2}\rangle$

$$\begin{aligned}M_{1,2} &= Re(\lambda_{1,2}) \\ \Gamma_{1,2} &= 2Im(\lambda_{1,2})\end{aligned} \tag{2.9}$$

or

$$\begin{aligned}M_{1,2} &= M \pm Re\left(\sqrt{(M_{12}^* - \tfrac{i}{2}\Gamma_{12}^*)(M_{12} - \tfrac{i}{2}\Gamma_{12})}\right) \\ \Gamma_{1,2} &= \Gamma \mp 2Im\left(\sqrt{(M_{12}^* - \tfrac{i}{2}\Gamma_{12}^*)(M_{12} - \tfrac{i}{2}\Gamma_{12})}\right)\end{aligned} \tag{2.10}$$

Therefore, the masses and widths of the eigenstates are split around the mass and width of $|M^0\rangle$ by $\Delta M = 2Re\sqrt{|H_{12}|^2}$ and $\Delta\Gamma = 8Im\sqrt{|H_{12}|^2}$, respectively. The time-dependence may be pulled out to write the eigenstates of equation 2.3

$$|M_{1,2}(t)\rangle = e^{-iM_{1,2}t - \frac{1}{2}\Gamma_{1,2}t}|M_{1,2}(t=0)\rangle \tag{2.11}$$

CP violation may be considered in the formalism of mixing when the eigenstates are expanded in the basis state as

$$\begin{aligned} |M_1\rangle &= p|M^0\rangle + q|\overline{M}^0\rangle \\ |M_2\rangle &= p|M^0\rangle - q|\overline{M}^0\rangle \end{aligned} \tag{2.12}$$

and implies the following

$$\frac{p}{q} = \sqrt{\frac{M_{12}^* - \frac{i}{2}\Gamma_{12}^*}{M_{12} - \frac{i}{2}\Gamma_{12}}} \neq 1 \tag{2.13}$$

CP violation is an extremely interesting aspect of mixing in that it can provide the most direct evidence of possible New Physics. It has been studied and searched for extensively in the D^0 system[20, 21, 26, 27, 29, 30]. To date, no search has found an indication of CP violation in the D^0 system. However, the semileptonic decay channels do not allow for the ability to test CP conservation so for the remainder of this work, I will assume $p/q = 1$.

Turning to the D^0 system, the time-dependent Schrödinger equation relevant to mixing may be written

$$i\frac{\delta}{\delta t}\begin{pmatrix} D^0 \\ \overline{D}^0 \end{pmatrix} = \begin{pmatrix} 0 & M_{12} - \frac{i}{2}\Gamma_{12} \\ M_{12} - \frac{i}{2}\Gamma_{12} & 0 \end{pmatrix}\begin{pmatrix} D^0 \\ \overline{D}^0 \end{pmatrix} \tag{2.14}$$

The off-diagonal elements are now equal due to the assumption of CP symmetry. This is typically rewritten in terms of lifetime of the D^0 and two dimensionless variables, x and y.

$$\tau = \frac{t}{\tau_{D^0}}, \qquad x \equiv \frac{2\Delta M}{\Gamma_{D^0}}, \qquad y \equiv \frac{\Delta\Gamma}{\Gamma_{D^0}} \tag{2.15}$$

as

$$\frac{\delta}{\delta\tau}\begin{pmatrix} D^0 \\ \overline{D}^0 \end{pmatrix} = -\frac{1}{2}\begin{pmatrix} 0 & ix+y \\ ix+y & 0 \end{pmatrix}\begin{pmatrix} D^0 \\ \overline{D}^0 \end{pmatrix} \tag{2.16}$$

Assuming that mixing is small , $|ix+y| \ll 1$, equation 2.16 integrates to a mixing amplitude of

$$A_{mix}(\tau) = -\frac{1}{2}(ix+y)\tau \tag{2.17}$$

This is a good time to explain the fundamental difference between $D^0 - \overline{D}^0$ mixing searches involving hadronic decay modes and those with semileptonic decay modes. In the semileptonic channels there is only one path to the "wrong sign" (WS) final state, $D^0 \to K^{*+}e^-\overline{\nu}$; via mixing.

$$D^0 \xrightarrow{mix} \overline{D}^0 \to K^{*+}e^-\overline{\nu} \tag{2.18}$$

But in the hadronic channels, the WS final state can be reached via a doubly-Cabbibo suppressed decay as well as through mixing.

$$\begin{aligned} D^0 &\xrightarrow{DCSD} K^+\pi^- \\ D^0 &\xrightarrow{mix} \overline{D}^0 \to K^+\pi^- \end{aligned} \tag{2.19}$$

The ratio of amplitudes of these two decays I will note by $R_D e^{-i\delta}$, where δ is the phase difference between the right and wrong-sign decays which was recently measured at CLEO[31]. Therefore, the WS amplitude, including this affect, is

$$A_{WS} = A_D + A_{mix} = R_D e^{-i\delta} - \frac{1}{2}(ix+y)\tau \tag{2.20}$$

What we are interested in, though, is the relative WS decay rate

$$
\begin{aligned}
r_{WS}(\tau) = |A_{WS}|^2 &= |[R_D e^{-i\delta} - \tfrac{1}{2}(ix+y)\tau]e^{-\tau/2}|^2 \\
&= [R_D^2 - R_D(y\cos\delta - x\sin\delta)\tau + \tfrac{1}{4}(x^2+y^2)\tau^2]e^{-\tau} \\
&= [R_D^2 - R_D y'\tau + \tfrac{1}{4}(x'^2+y'^2)\tau^2]e^{-\tau}
\end{aligned}
\tag{2.21}
$$

where $x' \equiv x\cos\delta + y\sin\delta$ and $y' \equiv y\cos\delta - x\sin\delta$.

We are also interested in the time-integrated WS rate

$$R_{WS} = \int_0^\infty r_{WS}(\tau)d\tau \tag{2.22}$$

or

$$
\begin{aligned}
R_{WS} &= R_D^2 - R_D y' + \tfrac{1}{2}(x'^2+y'^2) \\
&= R_D^2 - R_D y' + R_{mix}
\end{aligned}
\tag{2.23}
$$

where $R_{mix} = \frac{1}{2}(x'^2+y'^2) = \frac{1}{2}(x^2+y^2)$.

Equation 2.23 reveals the main difference between searches in hadronic and semileptonic decay channels. For the semileptonic searches, $R_D = 0$. This means a measurement of R_{WS} is equivalent to a measurement of R_{mix}. However, being symmetric in x and y, a measurement of R_{WS} via these decays offer no information on the mechanisms through which the mixing occured; virtual or real intermediate states. For the hadronic channels, it's not so straightforward. Due to the dependence of the interfence term on y', we have some hope of gaining insight into the mixing mechanism. However, this task is complicated by the fact that the value of R_{mix} is folded into the measurement of R_{WS} and it's extraction requires an analysis involving multiple lifetime dependences.

Turning back to a consideration of semileptonic decays only, since a decay to the WS can have occurred only through mixing, it is necessary only to divide the number of WS events by the number of "right sign" (RS) events, $D^0 \to K^{*+}e^-\overline{\nu}$.

$$R_{mix} = \frac{N(D^0 \to \overline{D}^0 \to K^{*+}e^-\overline{\nu})}{N(D^0 \to K^{*-}e^+\nu)} \tag{2.24}$$

In addition, calculating an average lifetime for mixed states

$$\langle\tau\rangle = \frac{\int_0^\infty \tau r_{WS}(\tau)d\tau}{\int_0^\infty r_{WS}(\tau)d\tau} = 3 \tag{2.25}$$

reveals that mixed decays are expected to have an average lifetime that is three times the unmixed decays. This is due to the mixed state's amplitude dependence on $\tau^2 \cdot e^{-\tau}$ as shown in Figure 2.4. Therefore, a fit to the lifetime distribution of WS final states with the form

$$D^0_{mix}(\tau) = \frac{1}{2}R_{mix}\tau^2 \cdot e^{-\tau} \tag{2.26}$$

can yield information about R_{mix} as well.

And finally, for this analysis specifically, a search for mixing in the $K^*e\nu$ channel takes advantage of a mass cut on the K^* resonance and is eventually to be combined with the result from the search for mixing via the decay $D^0 \to Ke\nu$ currently in progress.

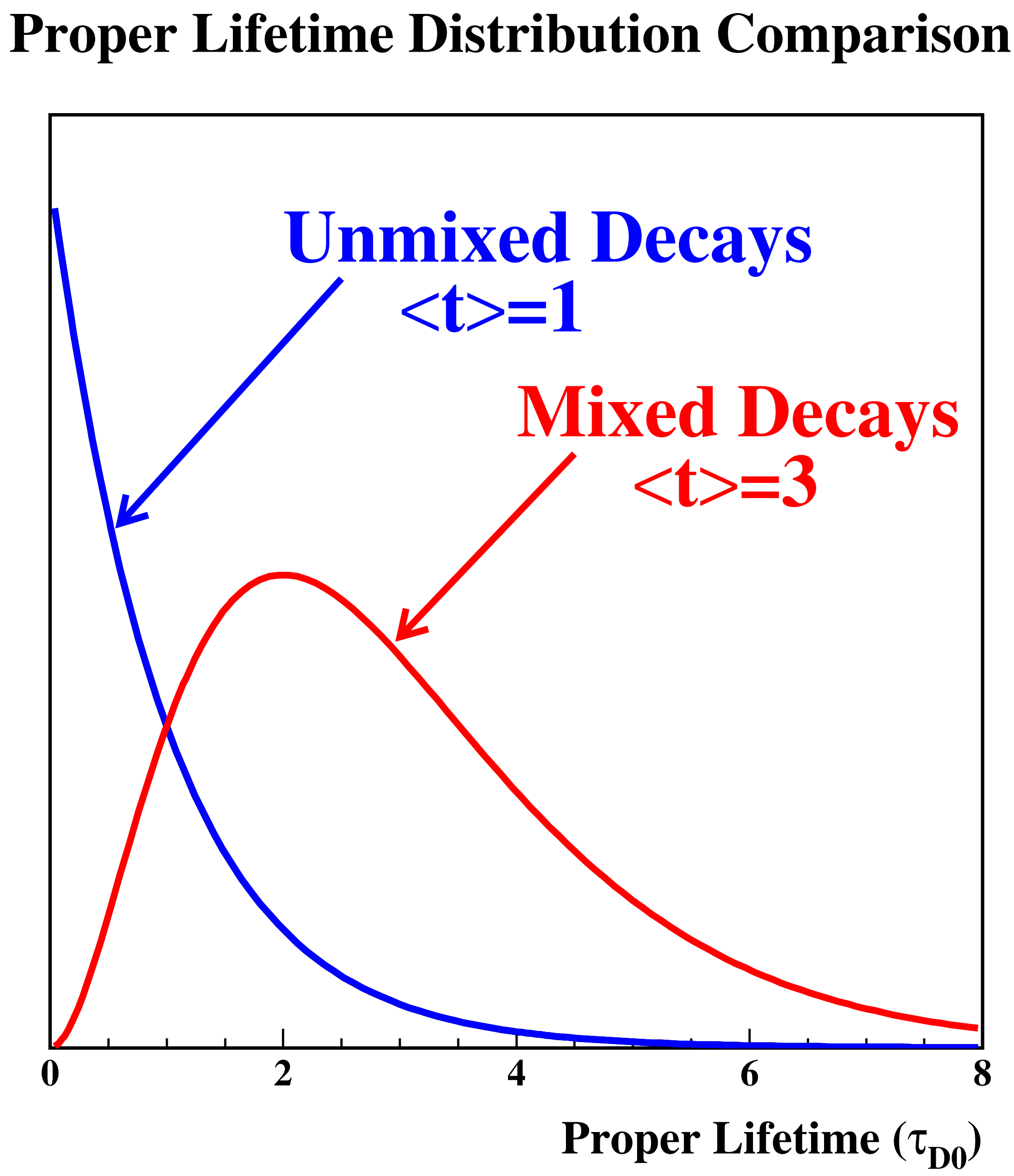

Figure 2.4: The lifetime of mixed states is expected to have a $t^2 \cdot e^{-t}$ dependence. This can be used as another fingerprint of mixed decays.

Chapter 3

The Experiment

The data used in this work was collected at the CLEOII.V detector at Cornell University in Ithaca, NY. The CLEO detector at the Wilson Synchrotron Laboratory has been used since 1979 to study e^+e^- collisions with electrons and positrons stored in the Cornell Electron Storage Ring (CESR). Wilson Lab is built into a hillside on the Cornell campus and CESR extends from within the lab in a 768 meter circumference loop 40 feet below Cornell's Alumni Fields[32].

3.1 The Cornell Electron Storage Ring - CESR

The storage of electrons and positrons in CESR is only the last step of multi-stage process to get particles to collide at the center of the CLEO detector. For most of the physics research being done at Wilson Lab in the CLEOII.V era, these particles must be generated and accelerated to the approximately 5.3 GeV operating energy demanded by the experimenters before they can be stored in CESR. Each par-

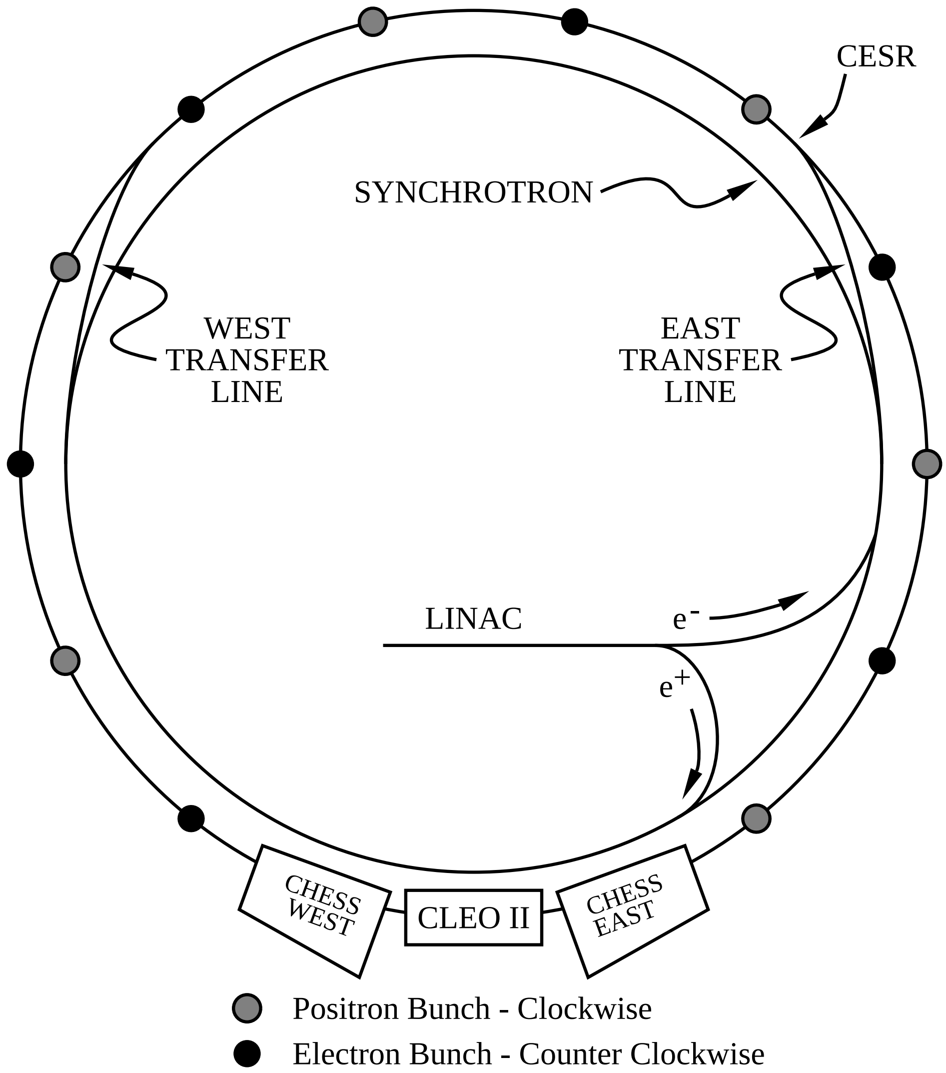

Figure 3.1: Schematic of CESR and the CLEO detector.

ticle species is created and accelerated separately before being dumped into CESR. Positrons comes first and then electrons.

3.1.1 LINAC

Electrons are easy enough to create. At CESR, the generated electrons are emitted from a heated filament not too much different from an average light bulb. They are then accelerated by microwave electric fields along the 30 meter length of vacuum pipe called the linear accelerator or LINAC to an energy of approximately 300 MeV[32].

Positrons are not so easy to create. Starting with the initial stream of electrons from the filament, a tungsten plate is placed in their path at a point when the electrons have an energy of about 140 MeV. Electron and X-rays and positrons are created by the impact of the energetic electrons on the tungsten. These positrons are selected and focused with magnetic fields and then accelerated down the remaining length of the LINAC to a final energy of about 200 MeV[32].

These streams of particles are initially in pulses of about three feet long. To prepare them for the next stage of acceleration, they are "prebunched" with a short series of cavities designed to compress the pulses down to about the width of a dime[32].

3.1.2 Synchrotron

At the end of the LINAC, the particles are now ready to enter the synchrotron for acceleration to the CESR operating energy.

The electrons and positrons are injected and travel in opposite directions around the synchrotron ring. Positrons travel clockwise when looking from above, electrons counterclockwise. Magnetic fields generated in the 192 3 meter long sections of bending magnets force the beams to stay in a circular path while four 3 meter long linear accelerators placed around the ring constantly increase their energies[32]. As the particle energies increase, the magnetic and electric field strengths in the magnets and cavities are increased in a synchronized fashion to further increase the particle's energies while keeping them within the circular beam pipe of the synchrotron. After about 4000 laps around the ring in a mere hundredth of a second, the particles are ready to be dumped into CESR[32].

This process is repeated about 60 times a second for 10 minutes until the required beam current is accumulated in the storage ring. At the end, both the positrons and electrons, traveling in opposite directions around the ring, are stored in bunches that resemble a line of trains. During most of CLEOII.V running, there were nine trains per bunch with three cars per train. Each car contained about 1.5×10^{11} particles and circled the ring with a cycle of 390 kHz[32]. This bunch train method was developed at CESR and subsequently copied in future accelerators at CERN, SLAC and KEK.

3.1.3 Storage Ring

Upon entering CESR the particles are traveling at 99.9999995% the speed of light with an energy of about 5 GeV and will circle for the the length of the data-taking run; usually about an hour[32]. For this reason, high precision is demanded of the vacuum system. The residual gas in the storage ring must be kept billions of times less dense than that of the normal atmosphere to severely limit the amount of e^+ and e^- scattering[32].

The magnet system consists of 86 dipole magnets that steer the bunches around the ring and 106 quadropole magnets to constantly refocus the beams[32]. Being tight bunches of similarly charged particles, they have a tendency to spread out. Numerous sextupole and octopole magnets placed around the ring provide more subtle corrections to the orbits.

As with any accelerated charged particles, the electrons and positrons in CESR are constantly radiating. This is called "synchrotron radiation" and the resulting energy loss is much greater in circular electron positron colliders than in machines that accelerate hadrons to similar energies. The electron and positron trains lose about 1.2 MeV per turn in the form of X-ray radiation[32]. Most of this impinges on the beam pipe in a narrow band around the outermost inside edge of the vacuum chamber. CESR is equipped with a water cooling system that circulates around the outer edge of the vacuum chamber to carry away the heat generated by this radiation. This lost energy is returned to the beams every cycle with two 500 MHz Radio Frequency(RF) Cavities[32].

Not all of this radiation goes to heating up the beam pipe. On opposing sides of the CLEO detector, breaks in the vacuum chamber allow some of the radiation to pass out of the beam pipe (see Figure 3.1). These high energy X-rays are used as probes in imaging experiments done at CHESS[33, 34].

Unavoidably, the beams pass each other in CESR at points other than the interaction region(IR). At these places, large capacitor plates called "horizontal separators" are placed to force the beams apart to allow them to pass without crossing paths. This results in pretzel-like orbits of the beams as they travel around the ring. A novel idea first implemented at CLEO.

At the heart of the CLEO detector, however, the beams are allowed to cross paths. At this point we are about to move out of the realm of CESR and into CLEO. Before we leave behind CESR completely, let me introduce the ultimately desired product of all the accelerations and steering and focusing done by CESR: the e^+e^- collision.

The collision of an electron and a positron results in their annihilation the creation of a massive "virtual" photon known as γ^*. Having mass, and therefore being unphysical, this photon must immediately decay. What avenues of decay are open to this photon depends on its energy. "Resonances" occur in certain energy ranges that are conducive to the creation of a bound state of a b and an $\overline{b}$, much like the hydrogen atom (see Figure 3.2). This family of resonances is known as the Upsilon system. The first three resonances in this family, the $\Upsilon(1S)$, $\Upsilon(2S)$, and $\Upsilon(3S)$, can decay only through the annihilation of the b and $\overline{b}$ into lepton and lighter quark combinations[3]. During the CLEOII.V era, CESR was run at an energy where the bound state of b and $\overline{b}$ had just enough energy to create a $B\overline{B}$ meson pair nearly at

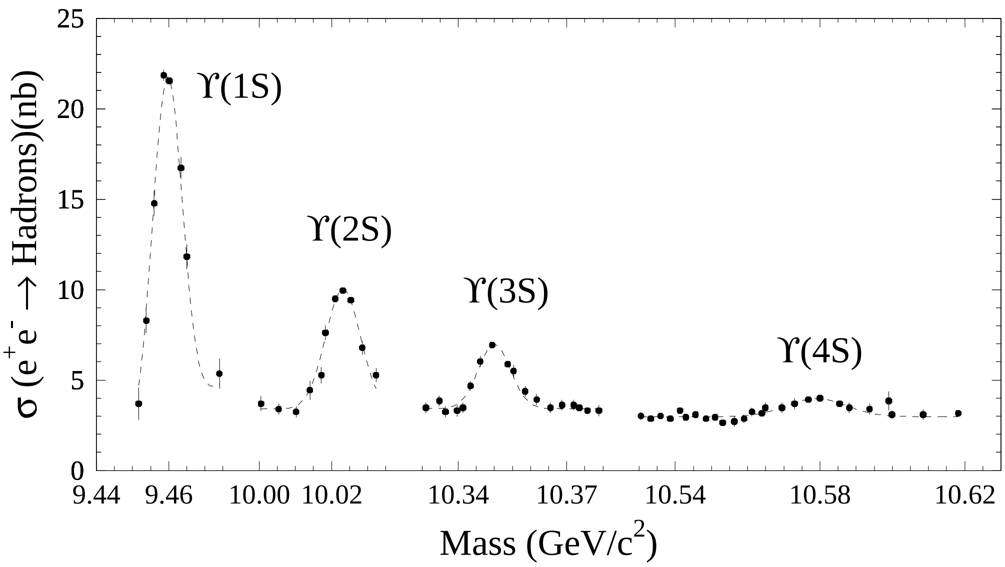

Figure 3.2: Continuum and resonant cross-sections of four Υ resonances. CLEOII.V collected data on the $\Upsilon(4S)$.

rest. This is the $\Upsilon(4S)$ resonance and occurs at an energy of about 10.58 GeV. CLEO was designed to study the decays of these B decays so CESR operating energies are typically run in an on to off-resonance ratio of 3:1. Off-resonance run energies were in the range between the $\Upsilon(3S)$ and the $\Upsilon(4S)$. Off-resonance events are typically used to gain information about backgrounds to $B\overline{B}$ production on-resonance. I will take full advantage of the 9 fb^{-1} CLEOII.V dataset since I am interested in extracting my signal from the continuum, the relatively constant cross section value seen between the resonances of Figure 3.2, where $c\overline{c}$ pairs are created with enough excess energy to make lifetime determinations of the resulting D mesons possible.

3.2 The CLEOII.V detector

Having generated electrons and positrons at the appropriate energies and directing them to interaction, the job of CESR is done. It becomes the task of the CLEO detector to record the subsequent decay products resulting from these high energy collisions.

3.2.1 Interaction Region

The interaction region of CLEO is defined by a short section of the beam pipe which, only in this area, is constructed of beryllium. Beryllium is electrically conductive like the rest of the beam pipe, but is used here for its low mass to minimize the amount of multiple scattering of the decay products as they pass out of the IR into the body of the CLEO detector.

The inner radius of the beam pipe here is 1.875 cm and the wall thickness is about 1mm. This thickness includes a double wall to allow for the passage of a cooling fluid along the length of the beam pipe to carry away the heat generated by the radiation in the IR[35].

My first task as a graduate student on the CLEO experiment was to conduct a test of a new cooling fluid for use with the beryllium beam pipe, PF^{TM}-200IG. Three small beryllium plates were immersed in de-ionized water, PF^{TM}-200IG and air to test the corrosive effects of PF^{TM}-200IG on beryllium. After three monthes of visual tests the

Table 3.1: Comparison of some of the physical properties of water and PF^{TM}-200IG[36].

Property	H_2O	PF^{TM}-200IG
Radiation Length (cm)	36.1	52
Specific Heat (J/kg·K)	4186	2300
Therm. Cond. (W/m·K)	0.6	0.159
Boiling Point (°F)	212	$380 - 470$
Specific Gravity	1	0.78
Viscosity at 25°C (cSt)	0.89	2.41
Auto-ignition (°F)	–	410
Flash Point (°F)	–	200

samples were taken to CESR and placed in an area of moderate radiation to see if this catalyzed any reaction. The samples absorbed a dose of 25 krads and still showed no visible sign of corrosion. The plates were then removed and any microscopic affects were sought with the use of a Scanning Electron Microscope. None were found[36]. Therefore it was determined that PF^{TM}-200IG is at least as chemically compatible with beryllium as the water it replaced at the end of the CLEOII.V run time. Table 3.1 summarizes the relevant properties of PF^{TM}-200IG and water. Of note is the longer radiation length of PF^{TM}-200IG compared to water. PF^{TM}-200IG is now used as a cooling fluid throughout the CLEO detector[36].

Before following the decay products out of the IR and into the body of the CLEO detector, I would like to mention one of the other maintenance jobs I performed while on CLEO. The "luminous region" or beam spot is the area where the electrons and positrons are allowed to directly interact. Within the interaction region the beams are

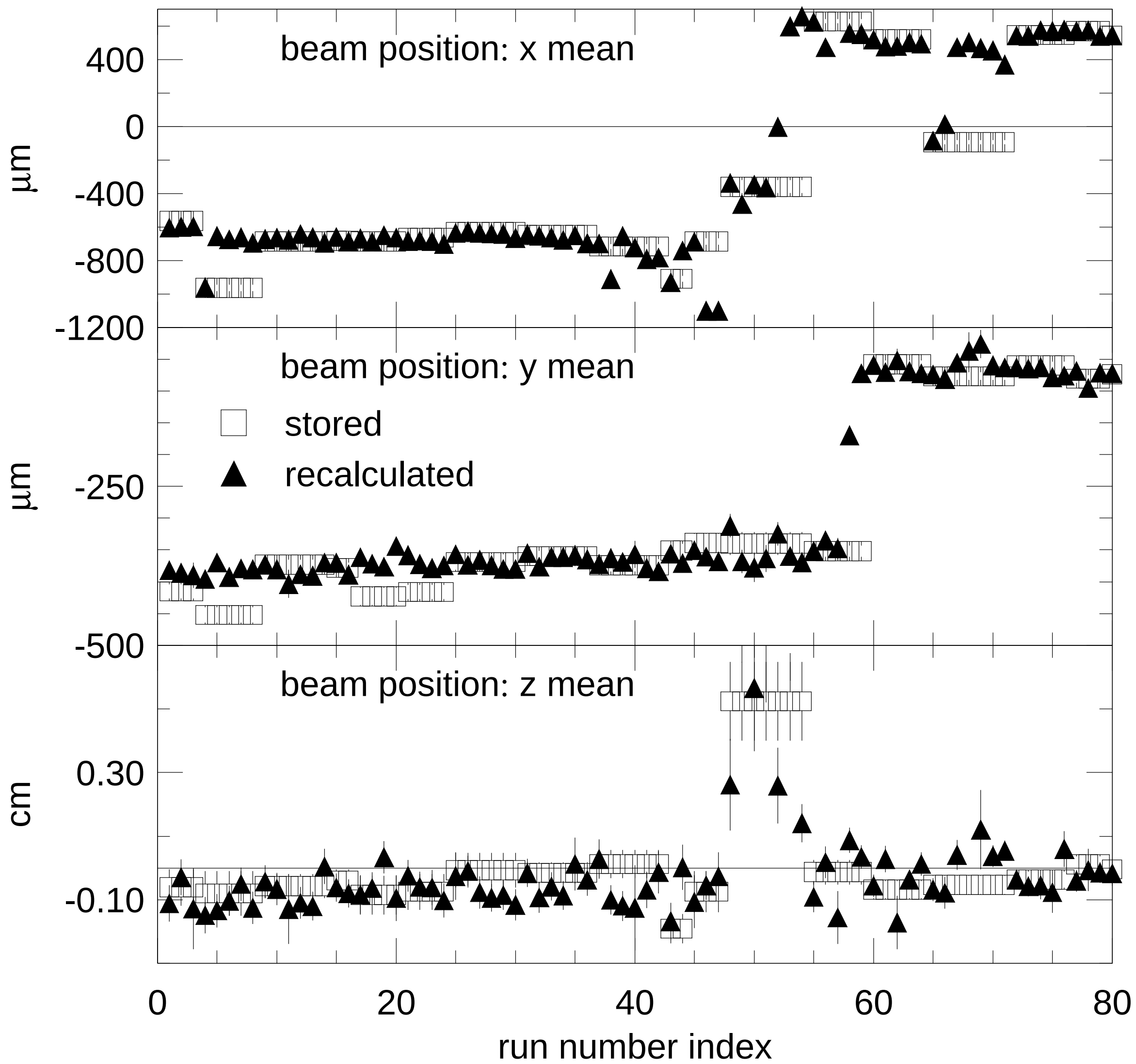

Figure 3.3: An example of the plots used to compare the stored beam spot position with those recalculated by vertexing the hadronic events of each run. This is an example of a time during CLEOII when beam spot positions were stored in blocks of runs of variable length. The accuracy of the recorded beam spot positions is seen to vary dramatically over the dataset as the beam spot shifts position midway through the extent of a block of stored positions. The coordinate system is centered on the geometric center of the CLEO detector.

directed at each other with a slight crossing angle to minimize "parasitic" interactions. The width of this beam spot is just over a centimeter long in the z-direction, 300 μm in the x-direction and only 8 μm in the y-direction. The narrowness of the luminous region in the y-direction and the accuracy with which the beam spot position is known is critical for the lifetime determination of the D^0 in this analysis (see Section 4.4). Using a routine that vertexed all the tracks of $e^+e^- \to \gamma^* \to hadrons$, my job was to double-check the beam spot position and width for all the runs of CLEOII and II.V. Early on in this task, I uncovered an error in the storage of the beam spot positions. The beam spot positions of each run, instead of being stored per run, were being stored in blocks of runs of variable length. Therefore, if the beam spot position were to change dramatically from one run to the next, which is known to happen, the assigned beam spot position could be hundreds of microns away from the actual position. Figure 3.3 shows an example of the block storage and the affect it has on the accuracy of the recorded beam spot position. It was revealed that this occurred only in runs during the CLEOII data-taking and had no affect on the lifetime measurements in $D^0 - \overline{D}^0$ mixing analyses since only data from CLEOII.V, with its Silicon Vertex Detector, is used.

Traveling radially outward from the interaction region, the detector is comprised of a Silicon Vertex Tracker(SVX), wire chambers, calorimeter, and a muon detector. Calorimeters are also placed at the endcaps allowing for almost 4π reconstruction of both charged and neutral tracks. All the detector elements within the muon de-

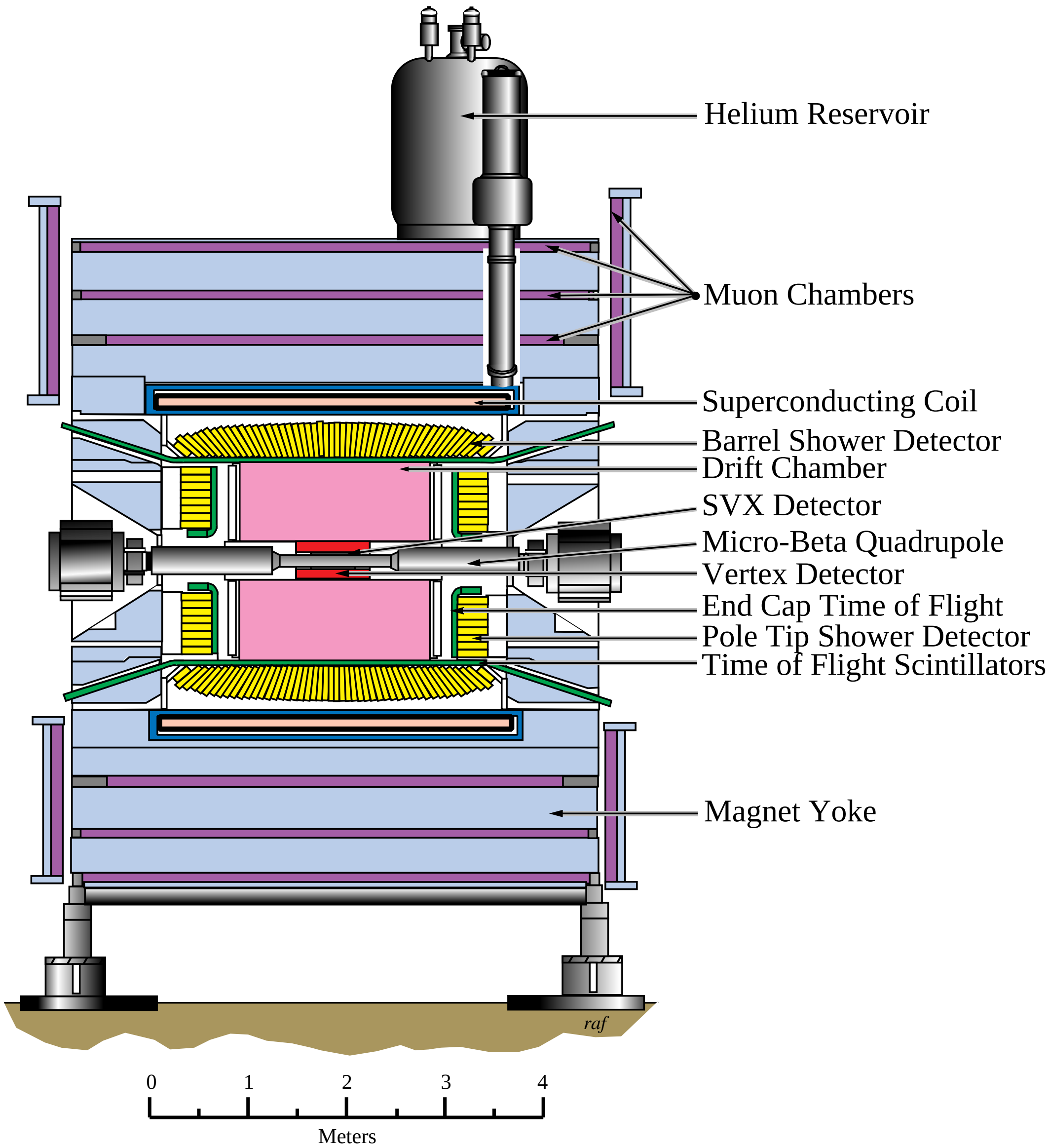

Figure 3.4: A side view of the CLEOII.V detector. Located at Cornell University in Ithaca, New York, it was a cylindrical, multipurpose detector with near 4π acceptance of both charged and neutral particles. It collected over 9 fb^{-1} of e^+e^- collisions on or near the $\Upsilon(4S)$, $\sqrt{s} = 10.6$ GeV, between November, 1995 and February, 1999.

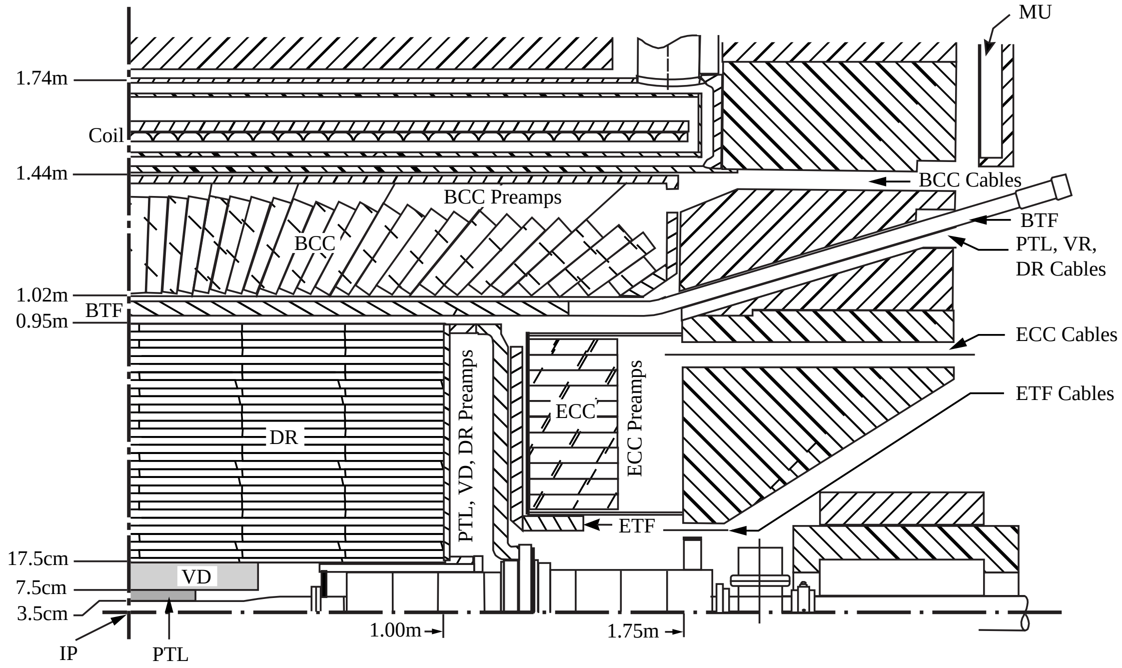

Figure 3.5: A side view of a quadrant from the CLEOII detector. The upgrade to CLEOII.V that took place in November, 1995, saw the replacement of the Precision Tracking Layers(PTL) with the Silicon Vertex Tracker.

tector are immersed in a 1.5 T magnetic field pointing in the negative z-direction (east) generated by a superconducting coil whose liquid He reservoir is clearly seen in Figure 3.4. The superconducting coil is 3.5 meters long and has an inner radius of 2.9 meters and its magnetic field is uniform to $\pm 0.2\%$[35]. This magnetic field bends the paths of charged particles in the wire chambers allowing for momentum determinations.

3.2.2 Silicon Vertex Tracker

The first piece of hardware particles encounter after passing through the beryllium beam pipe of the IR is the silicon vertex tracker (SVX). The SVX was installed as part of the CLEOII.V upgrade in November, 1995. It replaced a six layer straw tube array known as the Precision Tracker Layers(PTL) which can be seen in Figure 3.5. The SVX is a three layer device consisting of 96 300 μm thick silicon wafers[37]. The layers are arranged in octants with 12 wafers per octant. Each module is double-sided with an orthogonal arrangement of silicon strips. The innermost side runs parallel to the beam axis to provide z information about the track, while the outermost side runs perpendicularly to provide $r - \phi$ information. A total of 26,208 channels are read out[37]. The SVX allows for greater reconstruction of low momentum tracks and provides decay vertex information for lifetime determinations of particles like the D^0.

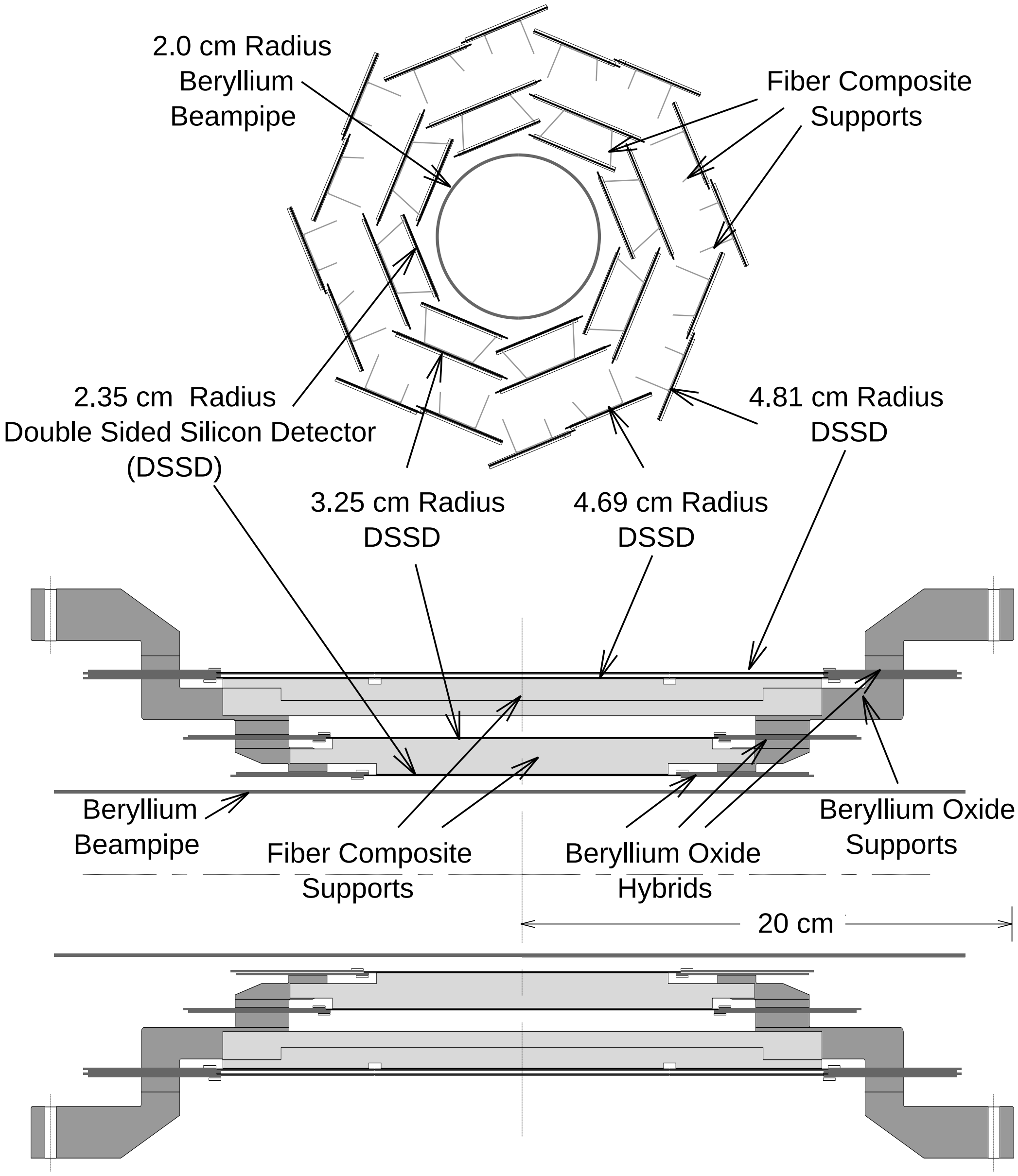

Figure 3.6: Details of the silicon vertex tracker(SVX) added to the CLEO detector in 1996. The SVX provides better reconstruction of low momentum particles and allows for vertexing of short-lived particles for lifetime determinations. The layers are instrumented to be read out one each side of the SVX, thus DSSD, double-sided silicon detector.

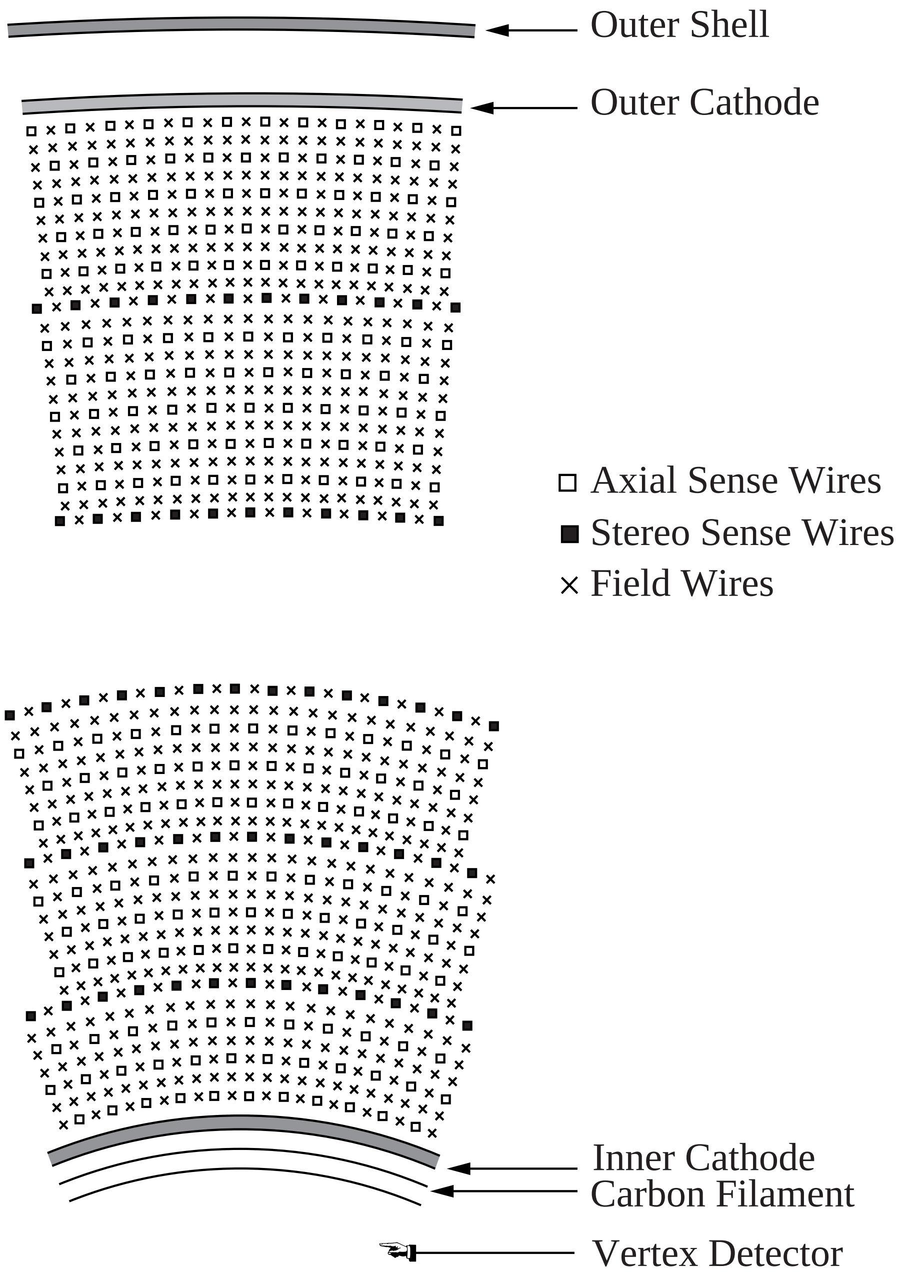

Figure 3.7: The arrangement of “field” and “sense” wires in the drift chamber.

3.2.3 Wire Chambers

The CLEO wire chambers are made of “field” and “sense” wires. Sense wires are maintained at a high voltage to generate the electric field throughout the chamber while the field wires are held at ground to shape the electric field in the vicinity of the sense wire to create “drift cells” centered on the sense wires[35]. Charged particles passing through the drift chamber ionize gas molecules in the 60%-40% helium-propane mixture that fills the wire chambers[35]. As the ionized electrons accelerate to the nearest sense wire, they gain energy and ionize more molecules causing an avalanche of electrons to converge on the wire in less than 1 nanosecond[35]. This is a “hit”. Current is collected and amplified on both ends of the detector. ADC’s measure the total charge accumulated and TDC’s measure the time of the hit. Calibrations map the ADC values onto specific ionization measurements (dE/dx)[39] to give some information about the particles mass. TDC values give an indication of the drift distance to measure how close the particle came to the sense wire.

There are two wire chambers in the CLEOII.V detector. The vertex detector(VD), which predates the SVX, is made of 800 sense wires in ten layers to provide $r-\phi$ and z information. Wires in the VD are 20 μm diameter nickel nichrome[35]. In addition, there are 2,272 field wires made of aluminum to minimize multiple scattering. The VD has a tracking resolution of 150 μm in $r-\phi$ and 750 μm in z[35]. The layout and geometries of the VD is shown in Figure 3.8.

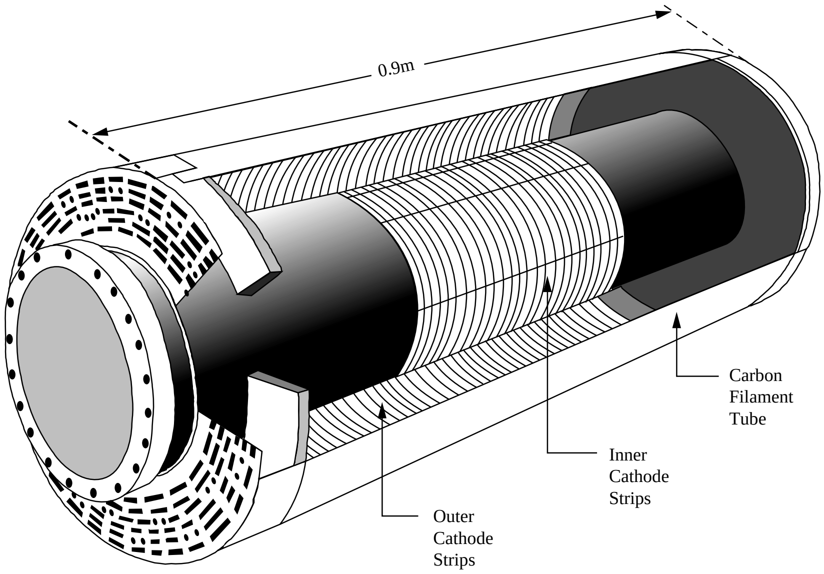

Figure 3.8: Geometry of the Vertex Detector.

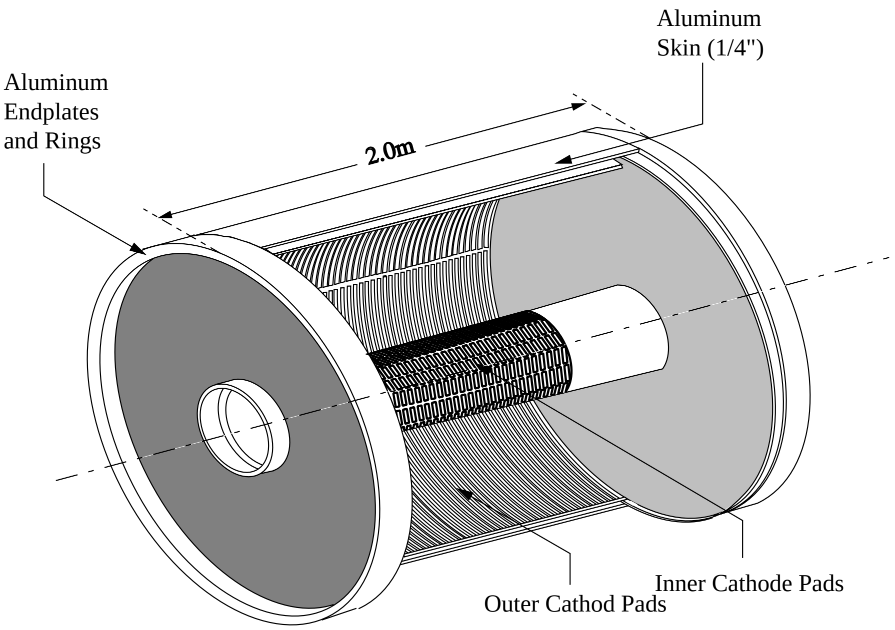

Figure 3.9: Geometry of the Drift Chamber cathodes.

The drift chamber(DR) is comprised of 40 axial and 11 stereo cells which provide azimuthal (ϕ) and polar (θ) tracking information, respectively. There are a total of 12,240 sense wires and 36,270 field wires in the 51 layers[35]. All the sense wires of the DR are made of 20 μm diameter gold-plated tungsten while layers 1-40 of the field wires are 110 μm diameter gold-plated tungsten and layers 41-51 are 110 μm diameter gold-plated beryllium[35]. The arrangement of the "field" and "sense" wires in the DR is shown in Figure 3.7. The endplates that support the wires of the DR are 3.175 cm thick aluminum[35]. These are shown in Figure 3.9 along with other DR geometries. The overall momentum resolution of the DR is $dp/p < 0.56\%$ at $p = 1$ GeV/c[38].

3.2.4 Time of Flight Scintillators

Scintillator paddles arranged around the exterior of the DR and in the endcaps provide particle Time of Flight(TOF) measurements while acting as a fast first level trigger for interesting events. Paddles are 5 cm thick pieces of Bicron BC-408, a plastic scintillator, attached to two photomultiplier tubes for readout[35]. There are 64 rectangular paddles in the barrel and 26 pie shaped paddles in the each endcap. At one time, the timing resolution was 140 ps for the barrel scintillators and 170 ps for the endcaps[35]. This was not the case for CLEOII.V data taking, however. These values degraded to 170 ps and 250 ps, respectively. Significant degradation of the scintillator material was found, presumably due to radiation damage[40], and the TOF system was subsequently removed at the end of the CLEOII.V era.

3.2.5 Crystal Calorimeter

The calorimeter is made of 7,800 thallium-doped cesium iodide (CsI) crystals. 6,144 of these lie around the barrel of the detector and provide coverage of 71% of the solid angle[32]. Figures 3.4 and 3.5 show how the crystals in the barrel are arranged so that particles will strike the crystal face at nearly normal incidence. The endcaps contain 828 crystals each with the crystals aligned along the z-axis. Each crystal is 5 cm square by 30 cm long resulting in an angular resolution of 5-10 mrad[35]. Figures 3.10 and 3.11 show the support structure and arrangement of the crystals in

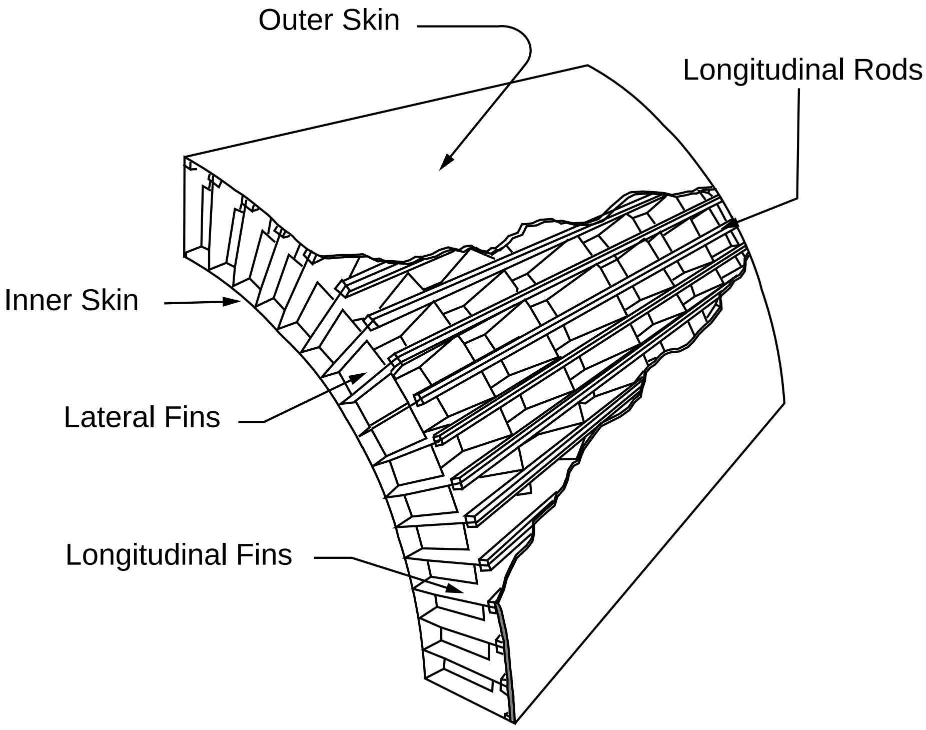

Figure 3.10: The support structure for the crystals in the barrel portion of the calorimeter.

the barrel and the endcap regions of the calorimeter, respectively.

The calorimeter collects information about photons and electromagnetic showers from particle interactions within the crystals. Energy resolutions are measured to be[35]

$$\frac{\sigma_E}{E}(\%) = \frac{0.35}{E^{0.75}} + 1.9 - 0.1E \quad \text{Barrel} \tag{3.1}$$

$$\frac{\sigma_E}{E}(\%) = \frac{0.26}{E} + 2.5 \quad \text{Endcap} \tag{3.2}$$

Therefore, the calorimeter has an energy resolution of about 2-3% for a 1 GeV electron or photon.

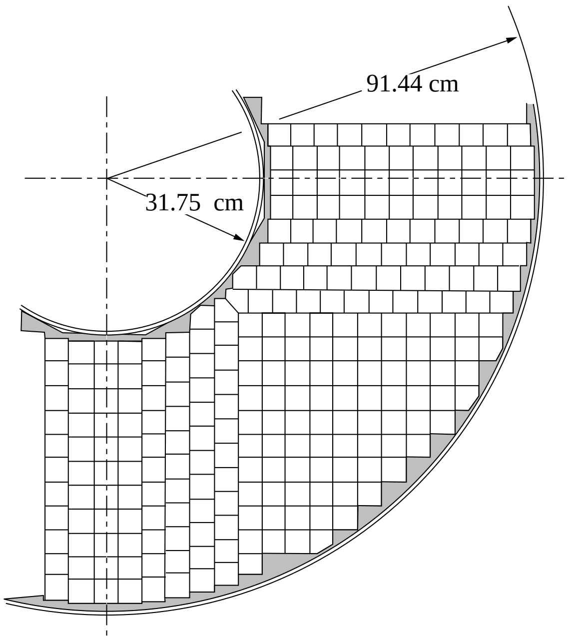

Figure 3.11: The arrangement of the crystals in the endcap regions of the calorimeter.

3.2.6 Muon Chamber

Finally, the muon detector is a collection of alternating particle detectors and several layers of iron sheeting. The iron allows only the most penetrating particles through to the detectors while, at the same time, acting as a flux return for the superconducting magnet. There are three layers of plastic streamer counters at depths of 36, 72, and 108 cm around the barrel[41]. The counters themselves consist of 3 layers, each 8.3 cm wide by 5 m long. Each of these contains eight 50 μm diameter silver-plated copper beryllium axially aligned anode wires to provide $r - \phi$ measurements. Charge division can be used to extract z. The total thickness is 7.2-10 nuclear interaction lengths depending on the trajectory of the particle[41]. The endcaps are instrumented with only one layer of these counters.

3.2.7 Trigger, Data Acquisition and Luminosity Record

Electron-positron collisions occur with such frequency in the IR that if every interaction or "event" were saved to tape, Wilson Lab would soon run out of storage space to house all the tapes. It is therefore necessary to have some system to determine whether an event is interesting enough to keep. At CLEO, this is a multistage process involving both hardware and software systems.

Crudely, events of the type $e^+e^- \to \gamma^* \to u\overline{u}, d\overline{d}, s\overline{s}, c\overline{c}, B\overline{B}, \tau^+\tau^-$ are the interesting reactions we wish to save at CLEO. Other events such as Bhabhas ($e^+e^- \to \gamma^* \to e^+e^-$), $\mu^+\mu^-$ pairs and cosmic rays are less interesting but may still be saved for use as detector diagnostic tools. Since $\tau^+\tau^-$ pairs are included in the above list and predominantly decay to only two stable charged particles[3], the CLEO trigger must be efficient at finding both interesting low and high multiplicity events.

There are four levels to the trigger system with each level requiring more information and, therefore, more time to make a decision. The first three, L0, L1, and L2, are hardware triggers. L0 simply counts the number of hits in the CC, VD, and TOF and makes a cut. In addition, there is a primitive ϕ angle coincidence system between the VD and TOF for "high momentum" tracks. These criteria make L0 nearly 100% efficient at selecting hadronic events. If L0 is triggered, data taking is disabled while L1 and L2 make more informed decisions about the relevance of the event. The L1 trigger is based on a Track Segment Processor(TSP)[43] and a binary link trigger(BLT)[44] as well as CC and TOF information. Both the TSP and BLT use VD and DR hits to form tracks in an event. L1 and L2 replace the L0 "hits" with BLT and TSP tracks in the VD and DR and also use energy measurements from "supersections" of the CC. L1 decisions are made within 1 μs and L2 decisions within 50 μs. The later L2 uses more track information and a more accurate energy measurement. In addition, L2 is designed to reject tracks that do not originate from the beam spot position (i.e., cosmic rays). For a luminosity of $4.5 \times 10^{32}\, cm^{-2}\, s^{-1}$, the L0 trigger rate is about 30 kHz and the L2 rate is about 35 Hz[35].

L1 and L2 form 16 trigger "lines" from the available information. The main trigger lines that accept hadronic events are the multitrack trigger and the energy trigger. At least three tracks need to be found and at least 40% of the beam energy needs to have been deposited in the calorimeter. Simulations with hadronic events show that greater than 99.5% of $e^+e^- \to q\overline{q}$ events pass these triggers. When rudimentary analysis cuts are applied, such as requiring at least five good tracks as in this analysis, the trigger is essentially fully efficient for accepted events.

The L3 software trigger is designed to look for non-beam-beam related interactions that produce multiple tracks, such as beam-wall and beam-gas interactions. L3 further rejects about 35% of the events that pass L2 without reducing the efficiency for hadronic events. Events that make it through L3 are written to tape. This accounts for the 9.0 fb^{-1} of CLEOII.V accumulated luminosity.

Table 3.2: The CLEOII.V accumulated luminosity record[46].

dataset name	run dates	ON res (pb^{-1})	OFF res (pb^{-1})	Total (pb^{-1})
4sH	11/16/95 - 3/11/96	357.9	160.9	518.8
4sJ	4/3/96 - 7/8/96	450.9	225.2	676.1
4sK	8/19/96 - 10/28/96	436.8	156.3	593.1
4sL	11/17/96 - 3/10/97	634.7	431.9	1066.6
4sM	4/5/97 - 6/17/97	373.4	157.5	530.9
4sN	6/19/97 - 8/17/97	418.1	292.2	710.3
4sP	10/15/97 - 2/9/98	745.3	356.7	1102.0
4sQ	2/27/98 - 4/21/98	381.0	178.8	559.8
4sR	4/21/98 - 6/5/98	324.4	174.4	498.8
4sS	6/27/98 - 10/5/98	862.4	345.2	1207.6
4sT	11/10/98 - 2/15/99	1196.3	384.6	1580.9
TOTAL	11/16/95 - 2/15/99	6181.2	2863.7	9044.9

Before going to tape, the data passes first through an online data quality monitor which also updates and maintains a constants database. It is then passed through a complete track reconstruction routine known as DUET[45]. Both the raw data and the reconstructed objects are saved to tape separately.

The range of CLEOII.V DAQ readout capability ran from 30 Hz to 60 Hz over the course of CLEOII.V data taking as trigger requirements were modified and software was improved. Some of the largest improvements came from identifying common SVX noise so that they may be ignored in the readout[35].

Until the turn on of PEP-II at SLAC and KEK-B at KEK, CLEO maintained the record for highest instantaneous and integrated luminosities. The highest daily accumulated luminosity achieved at CLEO, 32.3 pb^{-1}, exceeded the design goal by

33%[46]. Figure 3.12 shows the daily accumulated luminosity delivered to CLEO and Table 3.2 shows the accumulated luminosity record for the entire CLEOII.V data taking era.

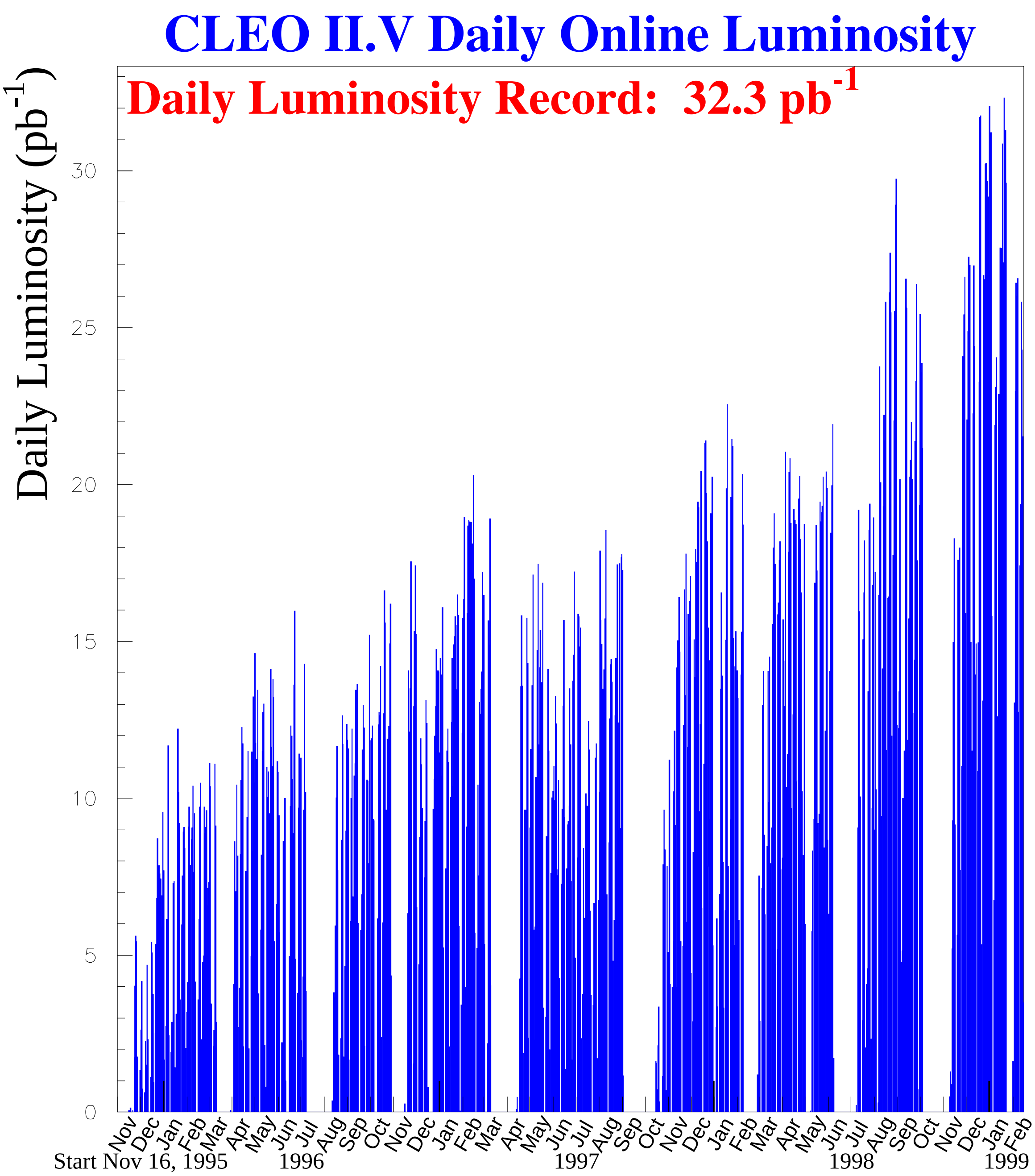

Figure 3.12: The daily accumulated luminosity record for the CLEOII.V experiment.

Chapter 4

Method

Before I get into the details of the analysis, I would like to give an overview of event selection and reconstruction. This is intended as a road map to follow through the analysis section with the details of methodology and efficiencies to follow.

4.1 Event reconstruction overview

Before I begin to describe the event selection and reconstruction techniques, I will introduce my decay chain. Of course, all charge conjugate modes are implied throughout this thesis.

$$D^{*+} \longrightarrow D^0\,\pi_s^+$$
$$D^0 \longrightarrow K^{*-}\,e^+\,\nu$$
$$K^{*-} \longrightarrow K_S^0\,\pi^-$$
$$K_S^0 \longrightarrow \pi^+\,\pi^-$$

Beginning with a D^* allows for tagging of the initial flavor of the D^0 with the charge of the low momentum or "soft" pion, π_s, from the D^* decay. This decay chain results in five stable charged particles, four π's and an electron, and a ν. The actual event selection and reconstruction proceeds along the same lines as those described here and will be expanded upon in later sections. All cuts and selection criteria and their corresponding efficiencies are enumerated in Tables 4.2 and 4.4 on pages 82 and 84, respectively.

First, it is necessary to select events which have the potential to be signal events. Not all events recorded in the CLEO detector come from $e^+e^- \to q\overline{q}$, therefore, CLEO assigns a class to each event with the variable KLASGL. Examples of these classes are radiative Bhabha events ($e^+e^- \to \gamma^* \to e^+e^-\gamma$), cosmic ray events, collinear leptons and yes, hadronic events. For this analysis, those events that are most likely hadronic events are selected; KLASGL = 10. KLASGL = 10 signifies that there are at least three charged tracks with at least one having a reasonable impact parameter with the beam spot. The total energy of these events must be at least 15% of the center of mass energy and the x and y vertex positions of the event must be within ± 2 cm and the z vertex position within ± 5 cm of the beam spot[47].

Also, for the reconstruction of my decay chain, I need at least five good tracks in the event; NTRKCD ≥ 5. For a description of the decay chain, see Table 4.3. NTRKCD is the number of tracks in the event identified to originate from the primary or a secondary vertex[48].

Another variable calculated for each event describes the jettiness, or conversely the sphericity, of the event; R2GL. R2GL is the ratio of the second to the zeroth

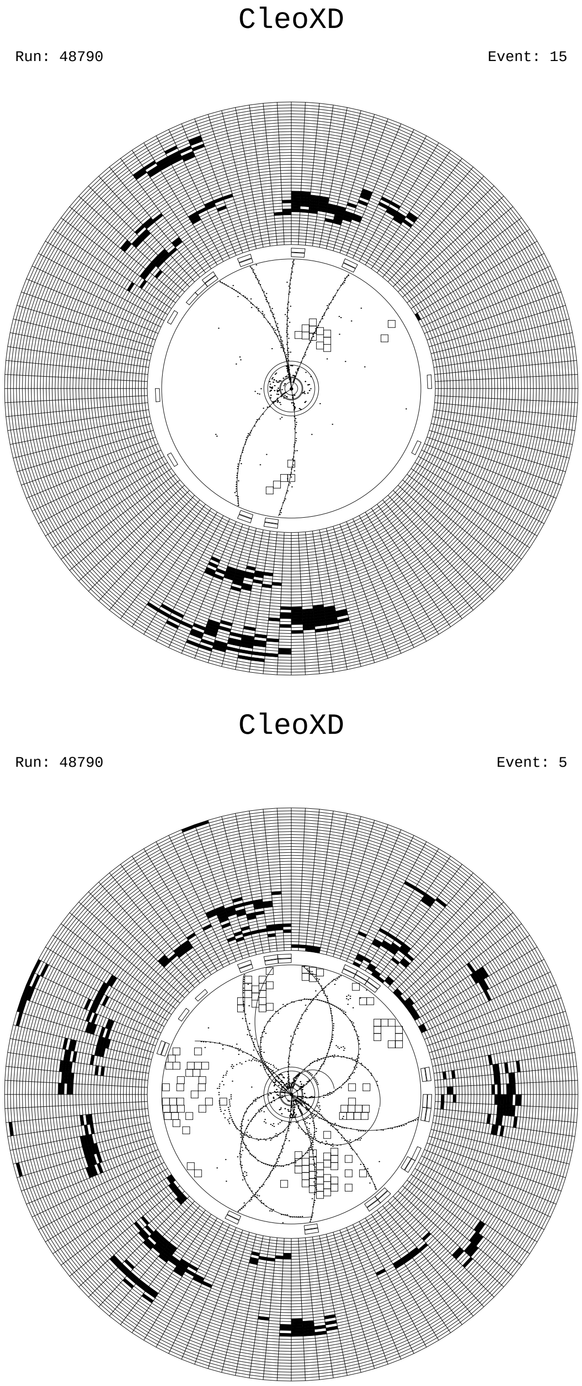

Figure 4.1: Examples of jet-like(top) and spherical events in the CLEO detector. Events with jet-like characteristics are selected for use in the analysis. Tracks can clearly be seen connecting the hits in the DR. Squares in the DR region are hits in the endcap calorimeters. The circular grid is a blown-out view of the CC with filled in sections representing cyrstal hits.

order Fox-Wolfram moments of the event[47]. Values of R2GL run from 0.0 to 1.0 with low values corresponding to more spherical events. Events with jet-like character are selected. A comparison of data and monte carlo distributions for R2GL is shown in Figure 4.19 on page 4.19. Figure 4.1 has examples of events in the CLEO detector considered jet-like and spherical.

After selecting candidate events, I look for those events that may contain an electron using a set of electron selection criteria that is described in detail in Section 4.2. In events where an electron is found, I look for K_S^0 candidates using an existing CLEO routine for finding secondary vertices, KNVF[49]. After selecting the K_S^0 with a mass cut, I search for K^*'s by finding π's that, when combined with the K_S^0, pass a K^* mass cut. Plots of the mass distributions for both the K_S^0 and the K^* in data and monte carlo are shown in Figure 4.20 on page 86. Since a vertex between the electron and the π_{K^*} candidate is used to determine the decay point of the D^0, both tracks are required to have at least two hits in both the silicon layers that describe the z direction and the layers that describe the $r - \phi$ direction. With those four tracks (e,π_{K^*},$2\pi_{K_S^0}$) accounted, for I look for π_s candidate tracks to complete the set of five observable particles. The π_s candidate must pass the track quality cuts listed below but is not required to have hits in the SVX since it is not used in determining a vertex. The charge on the π_s is taken as an indication of the initial flavor of the D^0 as in the decays $D^{*+} \to D^0\pi_s^+$ or $D^{*-} \to \overline{D^0}\pi_s^-$. The events in which the charge on the electron in the $D^0 \to K^{*-}e^+\nu$ decay matches the charge on the π_s are called "right sign"(RS). "Wrong sign"(WS) candidates are those with unmatched charges on the electron and the π_s.

All tracks used in the reconstruction are required to pass a set of track quality cuts which include the following:

- **TNG $\geq$ 0**: A measure of the track quality based on pattern recognition from the routine TRKMNG[50]. Tracks of TNG $= 0$ are of the highest quality, while a TNG $\neq 0$ signifies that the track may have fallen into a known pathology class. For example, a pair of ghost tracks may have been recognized. One is given a negative value of TNG and excluded.

- **KINCD = 0**: Identifies tracks that are loosely consistent with the primary vertex[51]. Tracks used to reconstruct the K^0_S are allowed to have KINCD ≥ 0 to allow for tracks originating from a secondary vertex.

- **no dredge**: A "dredge" track is one that was found only during the last-ditch effort to connect hits in the drift chamber into tracks[52].

- **no z-escape**: Z-escapes are tracks generated in a secondary pattern recognition routine to recover tracks lost through the endplates of the detector[51].

With a complete set of tracks in hand, I set about reconstructing the D^0. It is necessary to find the π_s candidate before proceeding to this step because the direction of the π_s is used in a determination of the direction of the D^0. This is described in detail in the $\vec{P}_{D^0}$ reconstruction method, Section 4.3.

After $\vec{P}_{D^0}$ reconstruction is complete, the π_s is combined with the D^0 to calculate the energy release, Q. Also, the lifetime of the D^0, τ, can now be calculated. The sample is then split into RS and WS candidates and the variables Q and τ are used in a 2-dimensional binned maximum likelihood fit.

This procedure is repeated for both MC and data. The MC sample is used to determine the appropriate functions and parameters used in the 2D fit. The subsequent systematic error analysis considers the validity of using a MC sample exclusively to determine these fitting parameters.

4.2 Electron selection

Since $\Gamma(D^0 \to e \text{ anything})$ is only about 8%[3], the first order of business for finding event candidates is to search for those hadronic events that contain an electron.

To find electrons, I use a combination two kinematic variables from the CLEO library. The first is SGELDI, which is the number of σ away from the expected specific ionization (dE/dx) of an electron in the drift chamber[53] or

$$\text{SGELDI} = \frac{I_{meas}(p, N_{hits}) - I_{elec}(p, N_{hits})}{\sigma_I(p, N_{hits})} \tag{4.1}$$

where I is the specific ionization which is a function of the particle momentum, p, and the number of hits in the DR, N_{hits}, and σ_I is the width of the distribution of known specific ionization values for electrons in the DR[39]. The second is E/P, the ratio of the energy and the momentum (≈ 1 for electrons) of the electron candidate.

The problem with any attempt at particle identification is that other species will have the same combination of variables at differing levels. This potential for contamination can be seen in the momentum dependences of the two electron identification variables in Figures 4.2 and 4.3.

For SGELDI, pion, kaon, and proton SGELDI distribution tails all cross the SGELDI = 0 at some momentum. Pions contribute the most contamination in this variable since most of the particles created in the detector are π's and they cross SGELDI = 0 at momenta closer to those of the signal electrons. Kaons and protons fake electrons as well, but both occur less often and cross at a higher momentum.

E/P becomes less effective as the momentum drops because the calorimeter's ability to make accurate measurements of the particle's energy declines (see Equations 3.1 and 3.2). This can be seen in Figure 4.3 as a widening in E/P as the electron momentum decreases and the incursion of more non-electrons into the region E/P $\approx$ 1. Also, as their momentum drops, fewer particles can make it to the calorimeter for an energy measurement. At a particle momentum of $\approx$280 MeV, the 1.5 T magnetic field with CLEO begins to curve the particles enough to cause them to miss the calorimeter and spiral inwards (see Figure 4.4).

To take advantage of the properties of the SGELDI and E/P distributions of the electrons, I combine these two variables into a phase space. I will refer to this as the "eID" phase space. One axis is simply SGELDI where the other is $20(1-E/P)c^{-1}$ to center the E/P distribution around 0 and rescale it to approximately the same scale

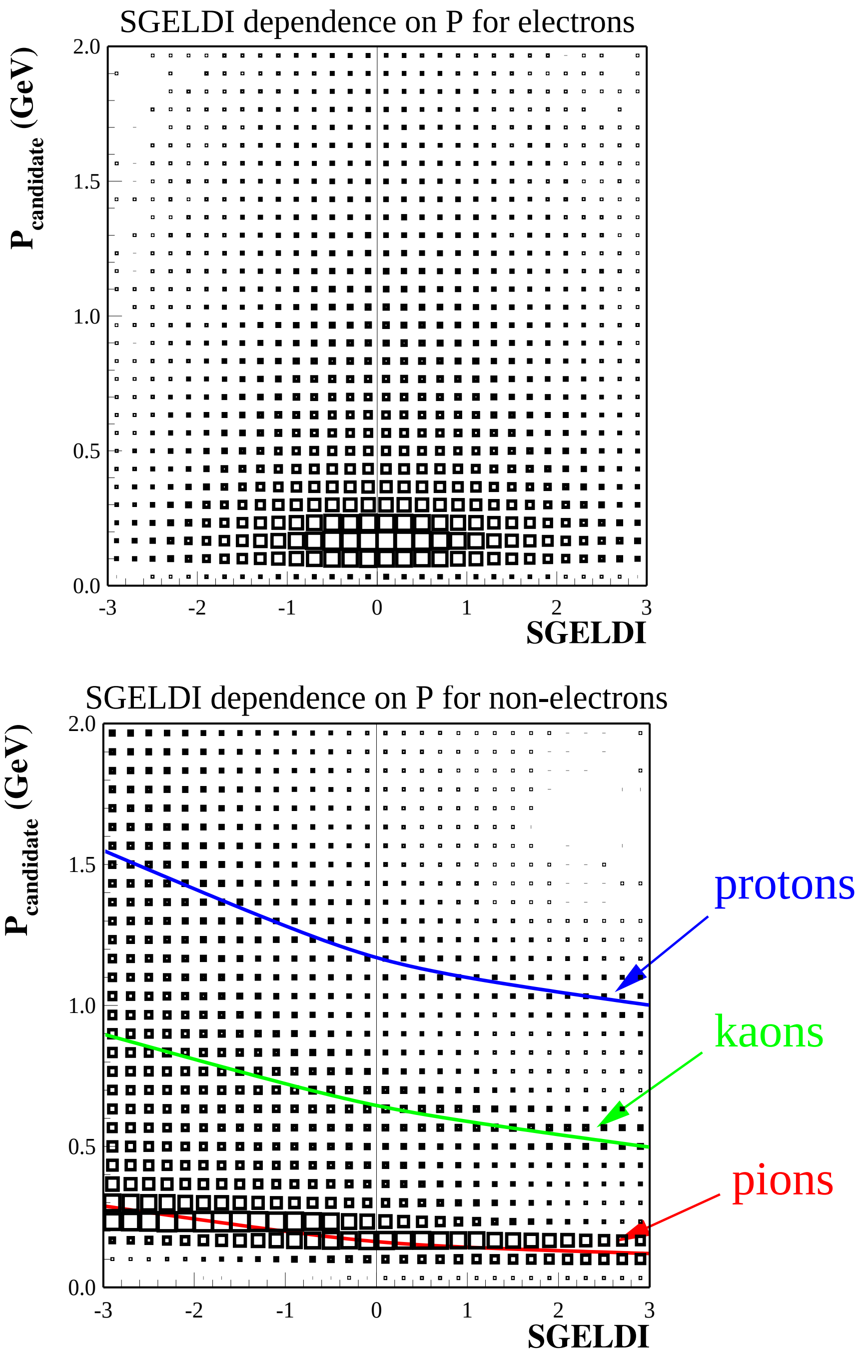

Figure 4.2: Momentum dependence of SGELDI (see Equation 4.1) for electrons(top) and non-electrons. Lines are included in the non-electron plot to show approximately where other species' SGELDI distributions cross the zero-point. These distributions are based on 520,000 generic continuum MC events. In this and all subsequent 2-dimensional plots, the size of the box is an indication of the relative occupancy of the bin.

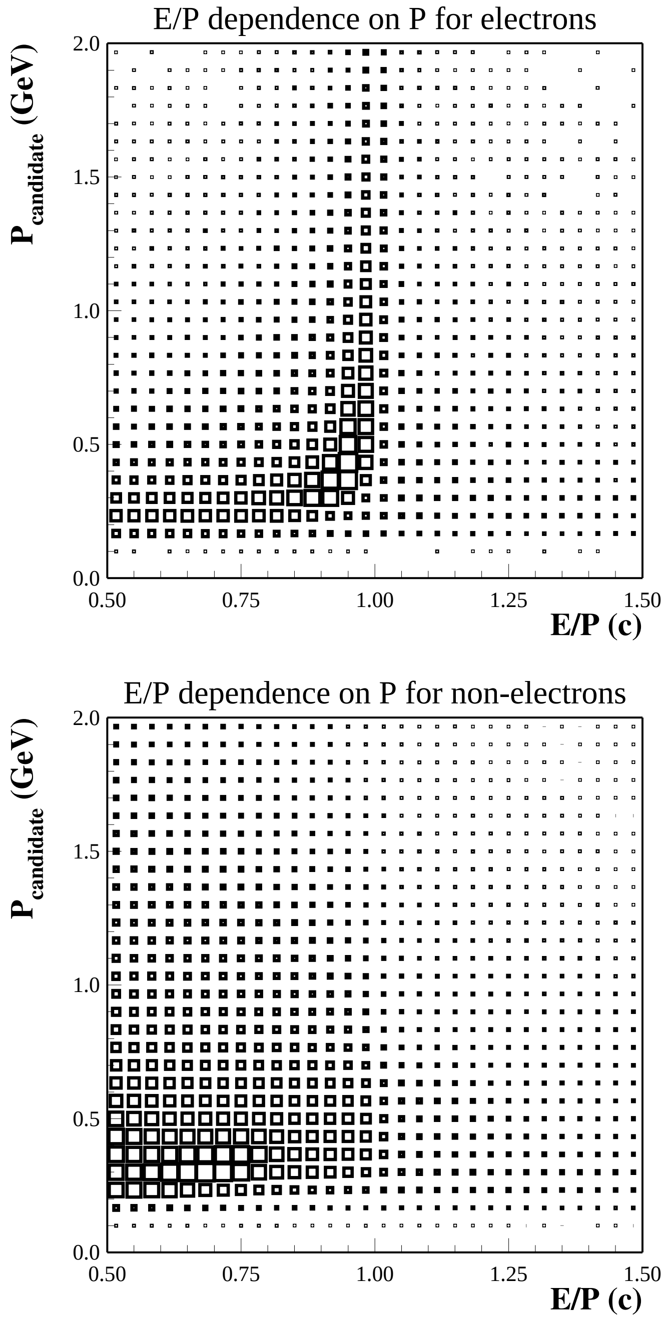

Figure 4.3: Momentum dependence of E/P for electrons(top) and non-electrons. For low p, it can been seen that not only does the electron distribution begin to move away from 1, but that non-electron concentrations increase as well. These distributions are based on 520,000 generic continuum MC events.

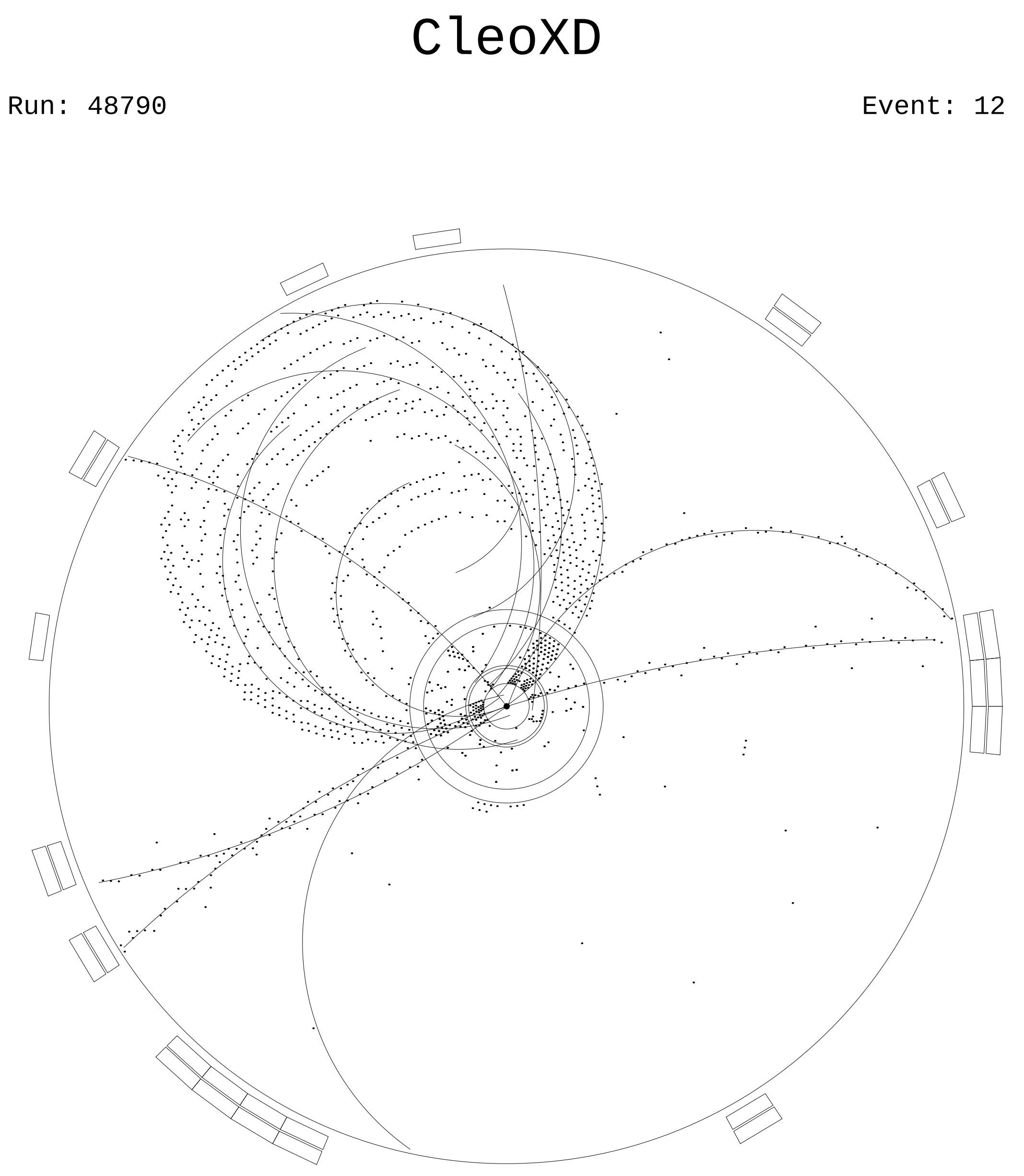

Figure 4.4: Below the momentum of ≈280 MeV, particles in the CLEO detector no longer have the momentum to carry them through the 1.5 T magnetic field to the calorimeter. These particles, called "curlers", spiral in on themselves until eventually decaying or interacting with a gas or wire particle in the drift chamber.

as SGELDI. In this space, cuts at

$$\sqrt{SGELDI^2 + [20(1 - E/P)c^{-1}]^2} < 2.0 \tag{4.2}$$

and

$$20(1 - E/P)c^{-1} > -0.6 \tag{4.3}$$

optimize signal-squared over background in the monte carlo. This is effectively a 2σ cut in dE/dx when E/P = 1 and limits on E/P of $0.90c < E/P < 1.03c$ at SGELDI = 0. This results in an almost hemispherical cut in eID phase space (see Figures 4.5 and 4.6). A comparison of SGELDI and E/P values between electrons in the monte carlo sample and electron candidates in the data sample is shown in Figure 4.8 on page 63.

A comparison of the efficiency of eID with an existing electron selection routine used in many CLEO analyses is contained in Appendix B.

It was revealed that a few simple kinematic cuts can augment eID by targeting electron fakes directly. Very narrow opening angles between tracks ($\theta < 5°$) can be an indication of γ conversion or ρ^0 decay. A routine exists in the CLEO libraries (GCFIND) to determine whether a particular electron candidate is part of an electron pair from a γ conversion with an optimum 96% efficiency[55]. In conjuction with this routine, I also compare all the opening angles of the electron and π_s candidates and the electron and π_{K^*} candidates in an attempt to identify ρ^0 decays and yet more γ conversions. As can be seen in Figure 4.7, the opening angle distributions for

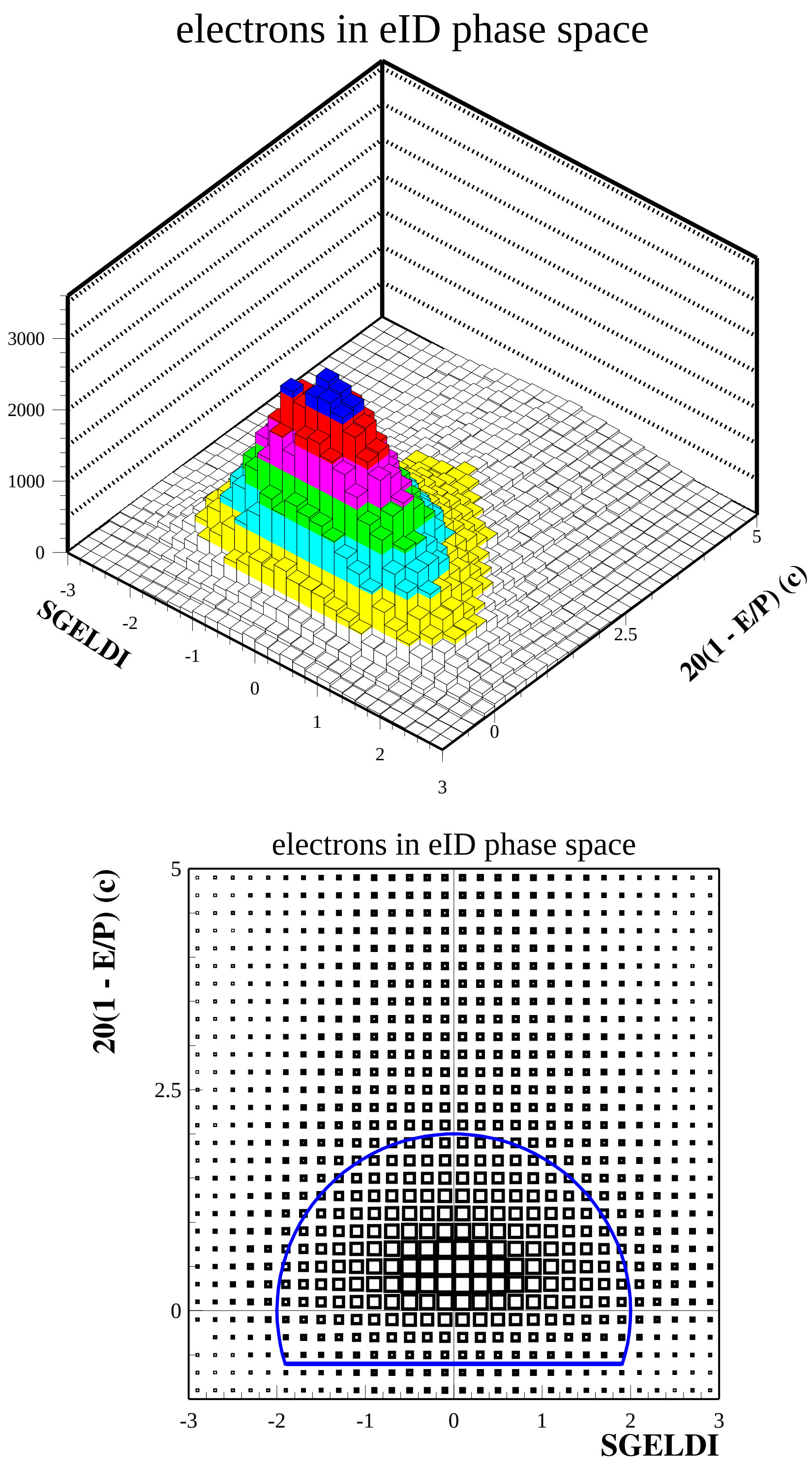

Figure 4.5: Electron distributions in eID phase space. Electrons are selected by taking candidates within the hemispherical cuts shown in the plot on the bottom. These distributions are based on $p > 330$ MeV tracks in 25×10^6 generic MC events.

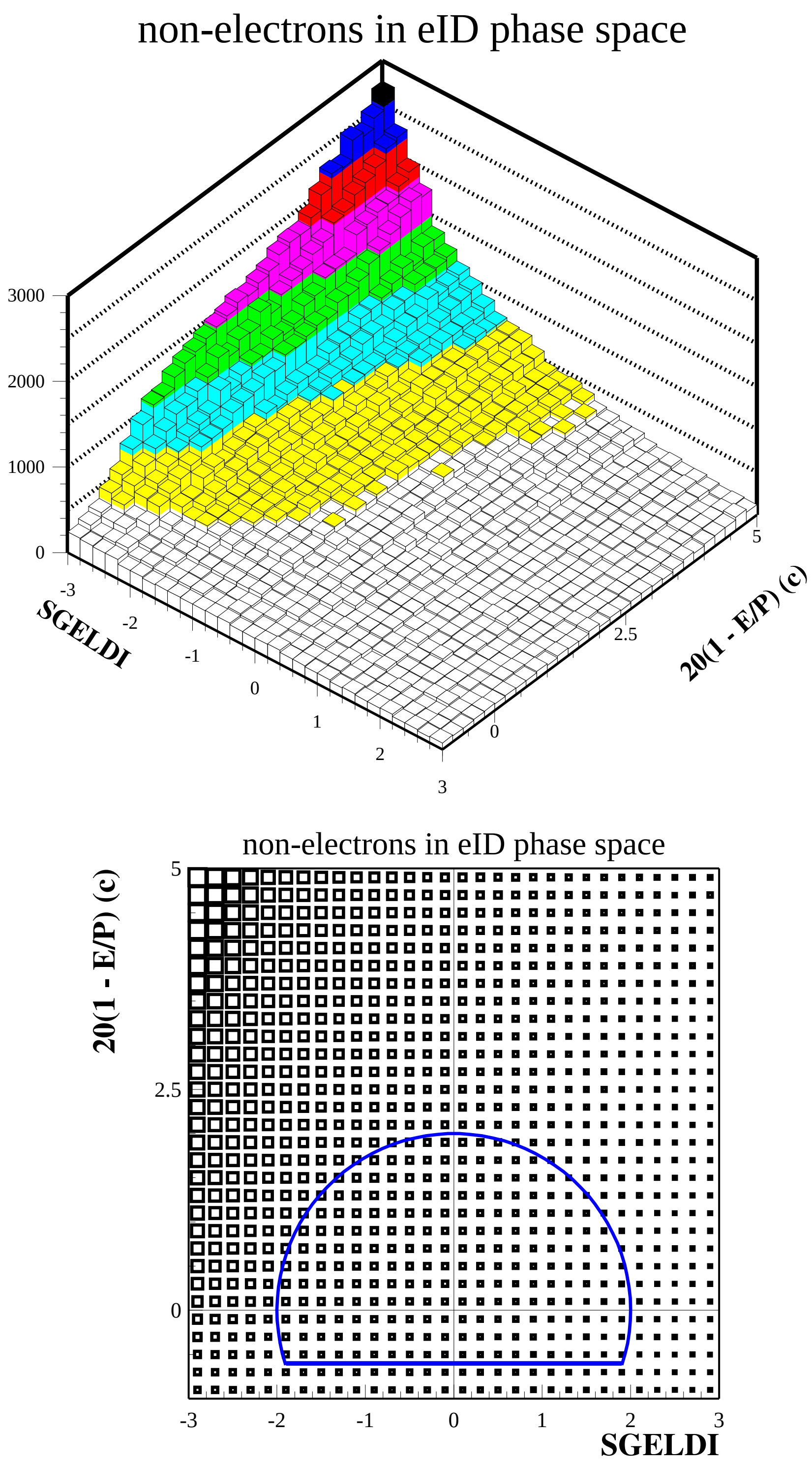

Figure 4.6: Non-electron distributions in eID phase space. Non-electrons are anti-selected by limiting candidates to the area within the hemispherical cuts shown in the plot on the bottom. These distributions are based on $p > 330$ MeV tracks in 25×10^6 generic MC events.

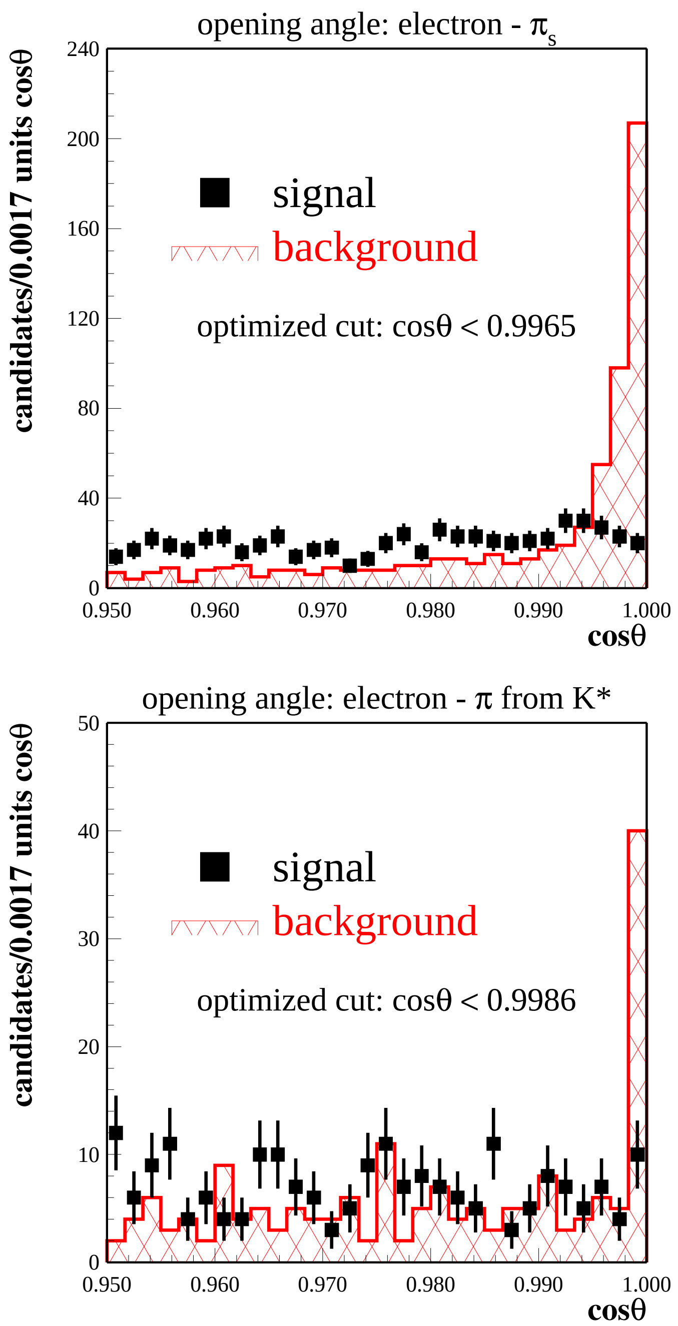

Figure 4.7: Cosθ distributions for the opening angles between the e and the π_s(top) and between the e and the π_{K^*} (the π from the K^* decay). These plots are based on RS signal and WS background monte carlo samples.

signal events tends to be flatter at high $\cos\theta$ values allowing for rejection of these two backgrounds with a minimum of signal loss (<1%). A narrow opening angle between the electron and the π_s or the π_{K^*} might indicate that a π from a ρ^0 decay has passed the eID selection criteria. An electron identification is not performed on the remaining four tracks once an electron track has been chosen. This allows some electrons from γ conversions to fake π_s or π_{K^*} candicacy. It is particulary dangerous when this phenomena occurs between the electron and the π_s since they are oppositely charged; an indication of WS signal. Nonetheless, the optimized cuts shown in Figure 4.7 are applied to both WS and RS events so as not to effect the relative efficiency of the two.

Figure 4.8 and 4.9 shows comparisons of some of the variables pertinent to the electron selection. A RS signal monte carlo sample is compared to RS data in the signal region, $0 < Q < 20$ MeV. Of course, a fraction of this region is backgrounds which can be seen by an enhancement to the data sample in low E/P values. When making the comparison, all the cuts are applied to both samples except the cuts relevant to the variable being plotted. Plots are based on approximately 150,000 signal monte carlo events and the 9.0 fb^{-1} of CLEOII.V data. Monte carlo plots are scaled to fit into region of data plots. A deficit of low momentum electron candidates in Figure 4.9 is due to an initial cut on candidate events taken from the data tapes, $p_e > 200$ MeV and $\sqrt{SGELDI^2 + [20(1-E/P)c^{-1}]^2} < 7.0$.

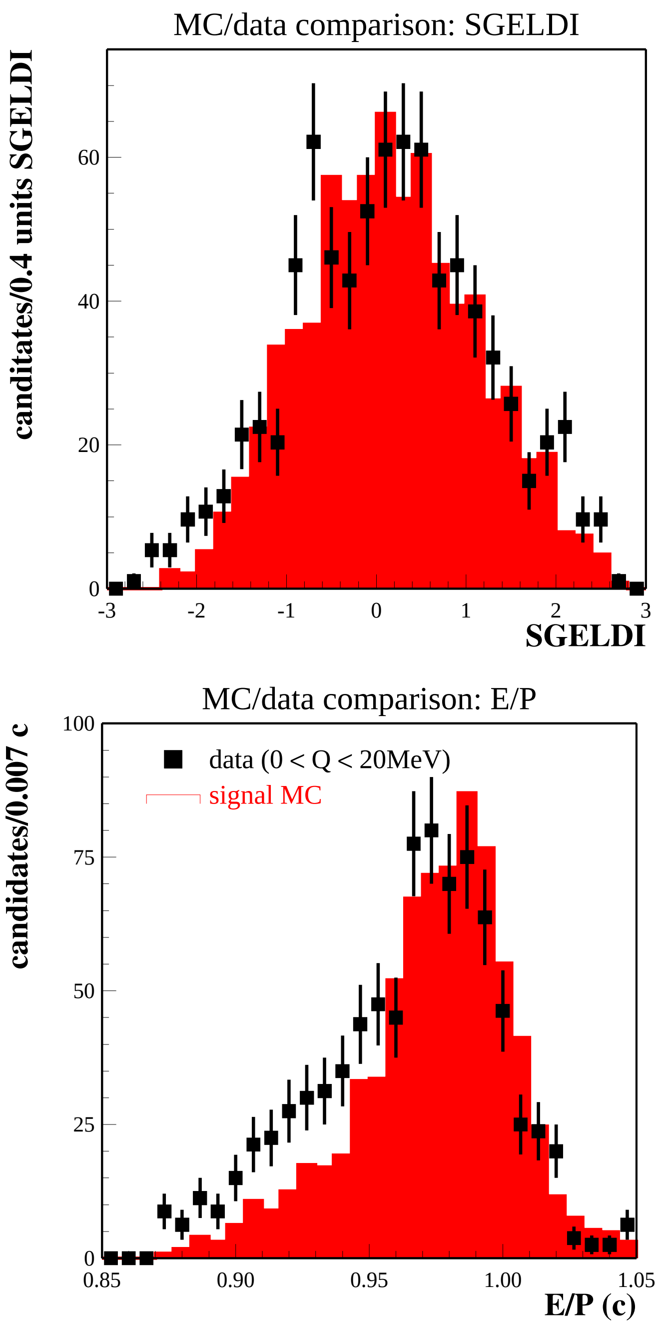

Figure 4.8: Monte carlo and data comparisons of some of the variables pertinent to eID. A RS signal monte carlo sample is compared to RS data in the signal region, $0 < Q < 20$ MeV. Backgrounds in the data sample can be seen in an enhancement at low E/P values. All cuts are applied to both samples except those relevant to the plotted variable.

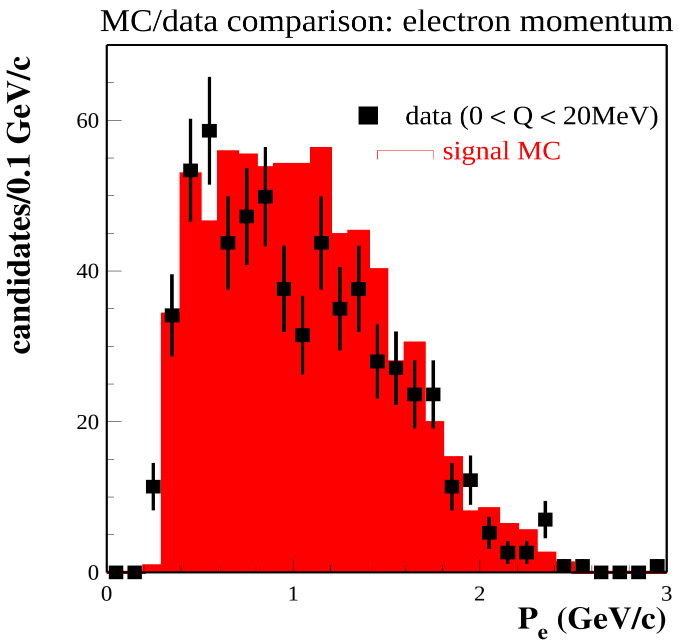

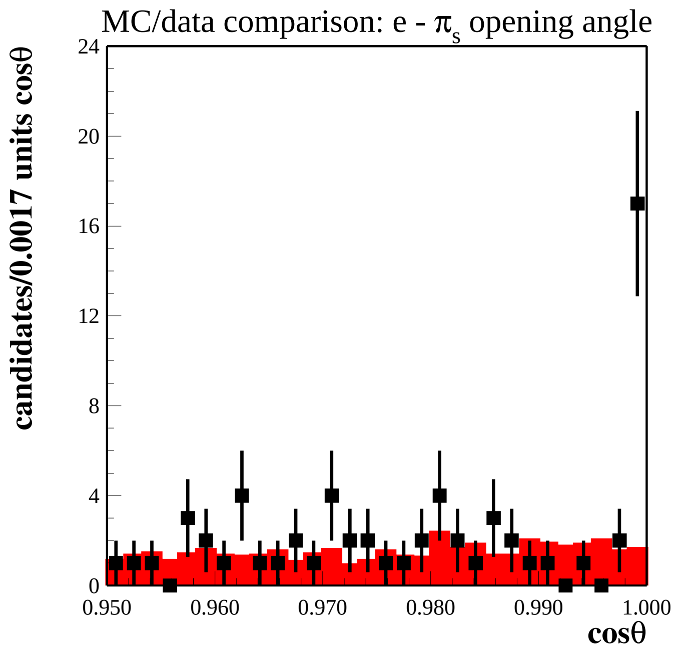

Figure 4.9: Comparisons of monte carlo and data distributions of some of the variables pertinent to eID. A RS signal monte carlo sample is compared to RS data in the signal region, $0 < Q < 20$ MeV. For the opening angle plot(bottom), WS candidates in the data are used. All cuts are applied to both samples except those relevant to the plotted variable.

4.3 $\vec{P}_{D^0}$ reconstruction

The reconstruction of the D^0 can be broken down into two fundamental steps. First, find the direction of the D^0 and then its total momentum.

Traditionally at CLEO, the direction of the D^0 is approximated with the *thrust axis*($\vec{TA}$)[54]. The $\vec{TA}$ is determined by finding the axis ($\vec{X}$) that maximizes the value

$$TH = \frac{\sum_{i=1}^{N}(\vec{p_i} \cdot \vec{X})|\vec{p_i}|}{\sum_{i=1}^{N}|\vec{p_i}|}. \tag{4.4}$$

Where N is the total number of tracks and unmatched showers in the event[56]. This approximates the "jet" or the massive-quark direction in the event. In this case, the *charm* quark.

The typical collision energy of 10.58 GeV during the CLEOII.V era is well above the energy necessary to create a $c\overline{c}$ pair. This extra energy manifests itself as extra particles in the jet as the $c\overline{c}$ pair hadronizes. We refer to this as "fragmentation". Fragmentation is a result of the c or $\overline{c}$ combining with other $q\overline{q}$ pairs in order to maintain a colorless state. At a fixed center of mass energy, the more and/or more energetic fragmentation particles that are created, the more the $\vec{TA}$ is pulled away from the true D^0 direction. A distribution of the opening angles between the thrust axis and the true direction of the D^0 can be seen in the upper left plot of Figure 4.10.

The thrust axis, however, is not the only indication of the direction of the D^0. At least two other vectors exist that can provide us with information. A reconstruction of the available daughters of the D^0, here the K^* and the electron, may also yield some clues to the D^0 direction. Lacking only the neutrino to be a complete reconstruction of the D^0, this "pseudo-D^0"($\tilde{D}^0$) is a good approximation of the $\vec{P}_{D^0}$ since

$$\lim_{p_\nu \to 0} \vec{P}_{\tilde{D}^0} = \vec{P}_{D^0} \tag{4.5}$$

The $\vec{P}_{\tilde{D}^0}$ provides an approximation to the direction of the D^0 with a resolution similar to that of the $\vec{TA}$. Again, see Figure 4.10 for a distribution of the opening angle between the $\tilde{D}^0$ and the true D^0 in monte carlo.

Also, because of the relatively low energy release, $M_{D^*} - M_{D^0} - M_{\pi_s}(Q)$, in the $D^* \to D^0\pi_s$ decay, the opening angle between the π_s and the D^0 is small (Figure 4.10). Therefore, the $\vec{P}_{\pi_s}$ provides yet another indication to the direction of the D^0.

It was my contention that correlations between these three indicators can be taken advantage of to calculate an approximation to the D^0 direction with better resolution than the $\vec{TA}$ used alone. To validate this contention, I begin with the hypothesis that the D^0 direction can be approximated by a linear combination of the unit vectors of the three indicators,

$$\vec{P}_{D^0}^{b.g.} = \mathcal{A}\widehat{TA} + \mathcal{B}\widehat{P}_{\tilde{D}^0} + \mathcal{C}\widehat{P}_{\pi_s} \tag{4.6}$$

and use monte carlo data to find the optimum set $\{\mathcal{A}, \mathcal{B}, \mathcal{C}\}$. Naively, the first attempt at an optimization considered only the mean and r.m.s of the opening angle distribution between the $\vec{P}_{D^0}^{calc}$ and the $\vec{P}_{D^0}^{real}$. This result was heavily weighted toward $\mathcal{C}$; the direction of the π_s. However, this had the effect of pulling backgrounds into the signal region since preferentially narrowing the opening angle between the π_s and the D^0 for

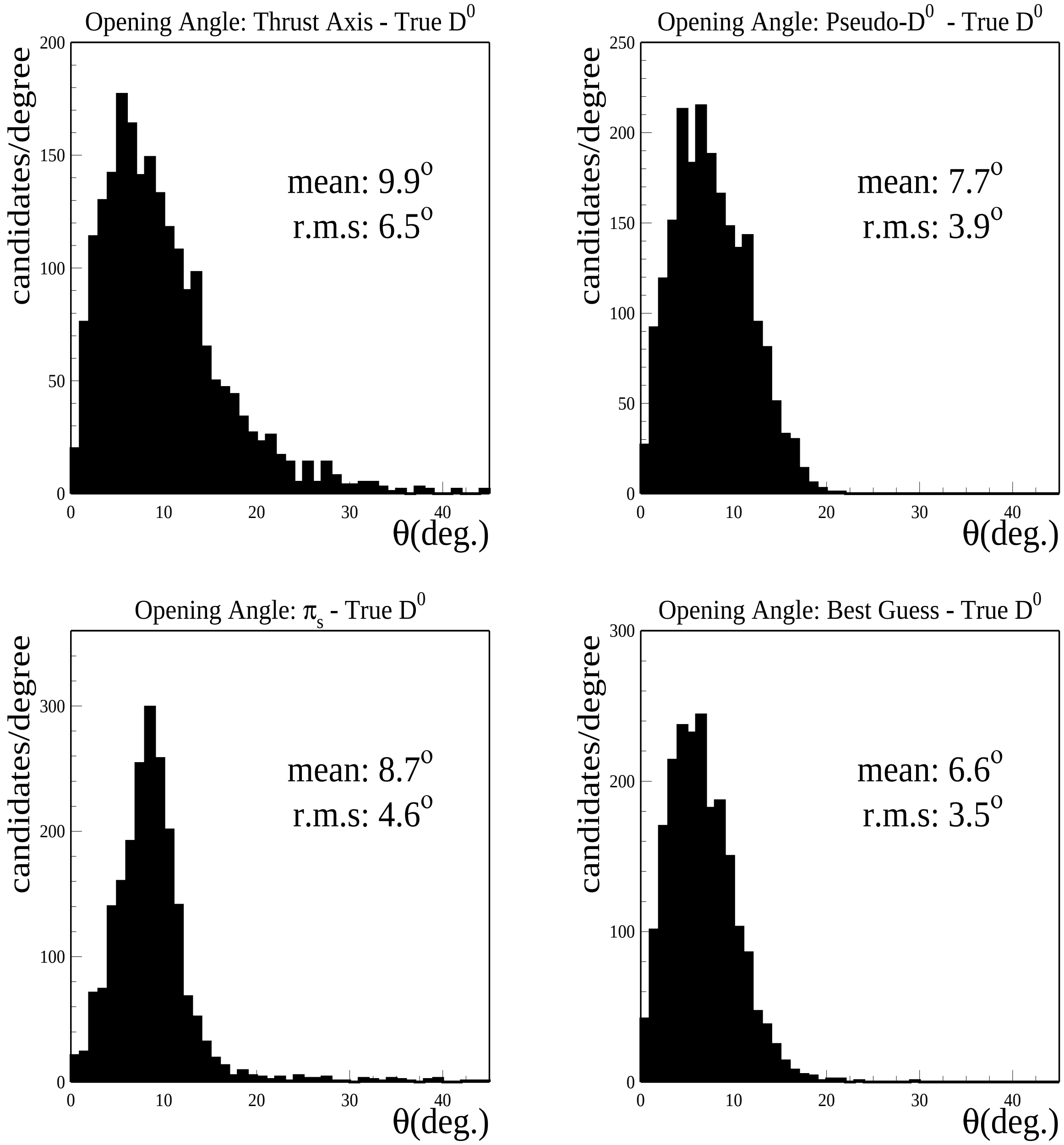

Figure 4.10: These four plots show the respective opening angles between the true direction of the D^0 and the thrust axis, the pseudo-D^0, the π_s, and the "best guess". The best guess is derived using a monte carlo sample of roughly 40,000 signal events to optimize a linear combination of the unit vectors of the other three axes. In so doing, correlations between the three can be taken advantage of to give a best guess direction that results in a distribution that is both narrower and has a smaller average opening angle. For this analysis, the best guess is comprised of roughly 23% thrust axis, 70% pseudo-D^0 and 7% π_s directions.

all events has the tendency to lower the Q value for all reconstructions. This resulted in a background shape similar to the signal shape in Q, making separation of the two difficult. Another monte carlo study was done with an eye on not only minimizing $|\vec{P}_{D^0}^{calc} - \vec{P}_{D^0}^{real}|$, but on maximizing the signal-squared over background ratio in the signal region, $0 < Q < 20$ MeV. Using a monte carlo sample that is approximately three times the data sample, it was found that the optimum set $\{\mathcal{A}, \mathcal{B}, \mathcal{C}\}$ for this analysis is $\{1.0,\ 3.0,\ 0.3\}$. I will refer to this method of optimizing the guess at the D^0 direction as the "best guess."

Is this method really better than just using the $\vec{TA}$? I set about to determine this by comparing the Q distributions that result from using either the $\vec{TA}$ alone or using the best guess. When a Gaussian with separate sigmas on either side of the mean, or a "bifurcated" Gaussian[57], was used to fit 75% of both distributions in the signal region, the best guess method resulted in a mean Q value closer to the known value and was 20% narrower in the fit region (Figure 4.11 and Table 4.1). Using the best guess method as opposed to the thrust axis alone also allows for $\approx 80\%$ more events to be successfully reconstructed using this D^0 reconstruction technique. How failures of this method are typically dealt with is further discussed in point 2) of the discussion on constraining the 4-vector to the mass of the D^0 below.

What about pulling backgrounds under the signal? Again, a comparison was made between the two methods. In the region of $0 < Q < 20$ MeV, the signal to background ratio for the best guess is 5.5:1 compared to 4.9:1 for using the $\vec{TA}$ only.

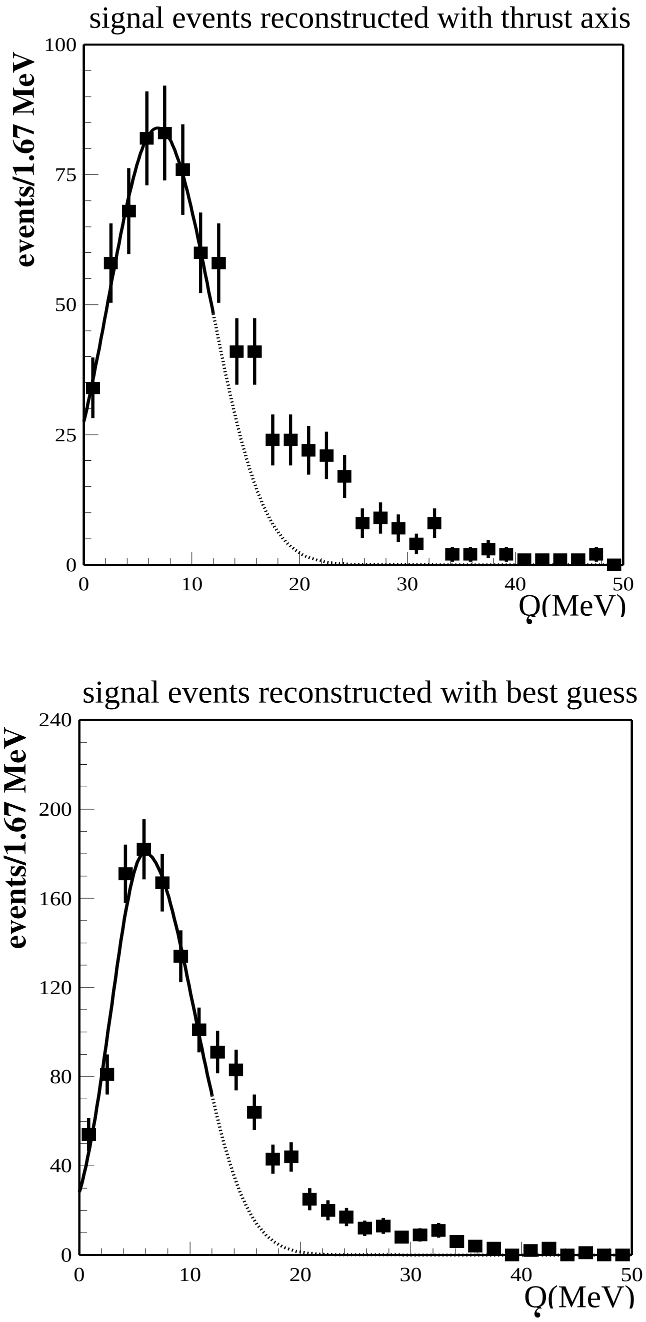

Figure 4.11: Bifurcated Gaussian[57] fits to Q distributions for signal events reconstructed using the thrust axis as the direction of the D^0(top) and using the best guess as the D^0 direction. Equivalent fractional areas are fit for in both instances (75%). The best guess fit is visibly narrower. The results are summarized in Table 4.1.

Table 4.1: Results of fitting the Q distributions that resulted from a calculation with the thrust axis taken as the direction of the D^0 and with the best guess method described in the text. A bifurcated Gaussian[57] was used to fit 75% of the signal events in each plot. The best guess method gave a fit that is 20% narrower in the fit region and a $<Q>$ closer to the true Q value of 5.84 MeV[58].

$axis$	$<Q>\ (MeV)$	$\sigma_{lo}(MeV)$	$\sigma_{hi}(MeV)$
thrust	6.8	4.6	4.9
best guess	5.9	3.1	4.5

In contrast to an initial attempt at a best guess calculation that resulted in being heavily weighted toward the direction of the π_s there appears to be no significant bunching of background in the signal region.

Once we have the direction of the D^0, it is necessary to calculate the total momentum. This is achieved by constraining the 4-vector to the mass of the D^0.

$$E^2 - \vec{P}^2 = M_{D^0}^2 \tag{4.7}$$

This results in a set of solutions for $\vec{P}_{D^0}$ that can be described by an ellipsoid centered on $\vec{P}_{\tilde{D}^0}$ (see Figure 4.13). To decide upon a single final solution, we turn to the calculated direction of the D^0. In general, there are three possible outcomes. 1) The direction of the D^0 could just touch the edge of the ellipsoid, allowing only one possible solution for $|\vec{P}_{D^0}|$. This of course is highly unlikely. Code was in place to notify me if this actually occurred. It did not. 2) The direction of the D^0 could fall somewhere outside the ellipsoid marking a failure of this particular reconstruction method for this set of tracks. In other analyses, when this occurs an alternate method

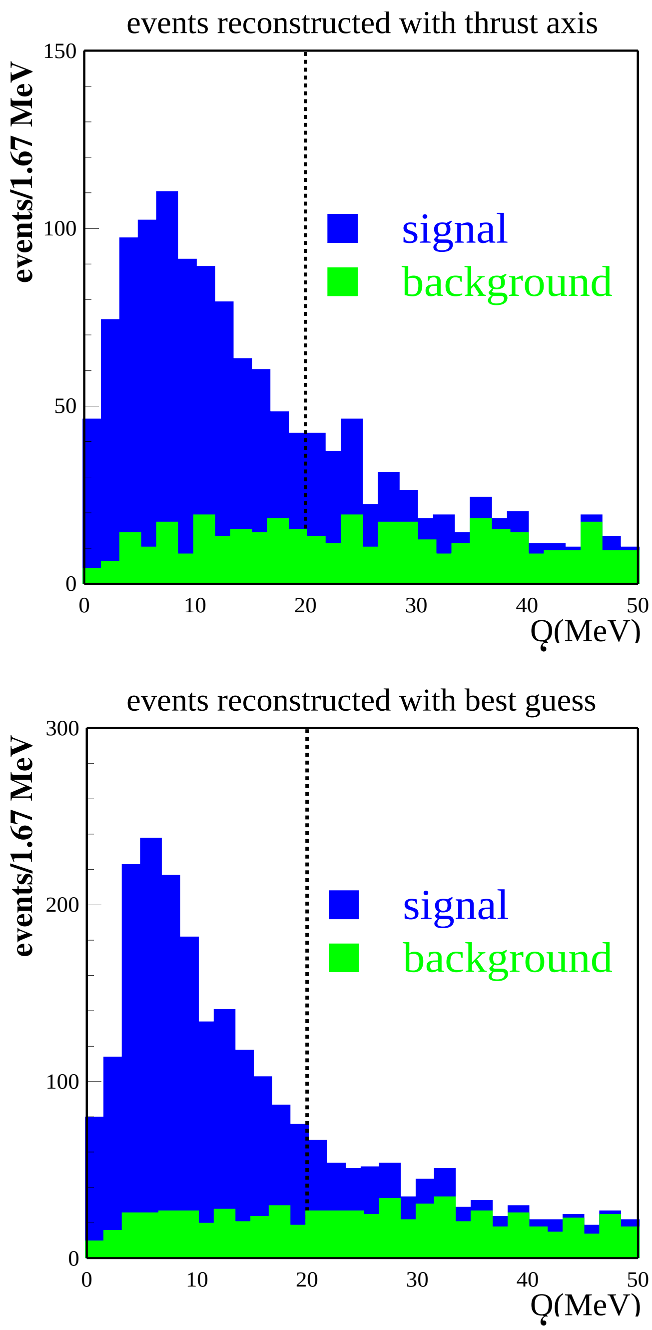

Figure 4.12: Comparison of how the backgrounds behave for both the reconstruction of events using the thrust axis(top) and using the best guess. In contrast to an initial attempt at a best guess which was heavily weighted toward the π_s there appears to be no significant bunching of background in the signal region.

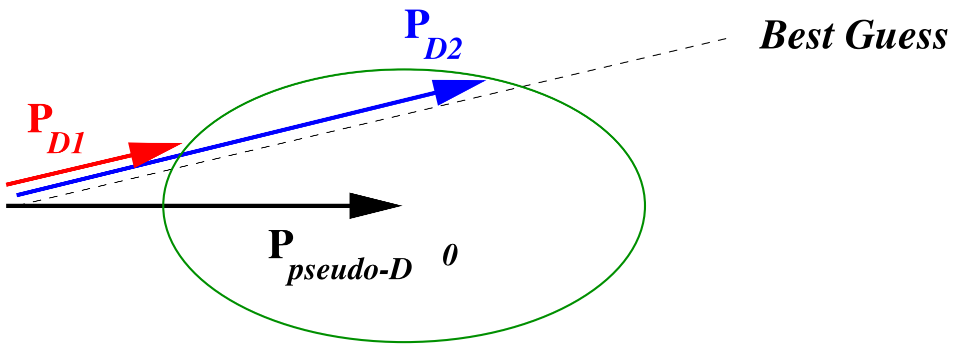

Figure 4.13: Constraining the 4-vector to M_{D^0} results in a set of solutions that can be described by an ellipsoid. The $\vec{P}_{D^0}$ can lie anywhere on this curve. Generally, the calculated direction of $\vec{P}_{D^0}$ intersects the set at two points allowing for two possible solutions. A method to select the most desirable of the two is needed.

of determining $\vec{P}_{D^0}$ is employed[54]. For instance, the missing momentum in the event may be taken to represent the $\vec{P}_\nu$ directly. For this analysis, the best guess method of determining the direction of the D^0 results in only 2% of the events falling into this category. I accept this small loss in signal instead of introducing more and varied backgrounds by attempting an alternate reconstruction technique. 3) The direction of the D^0 could pass through the ellipsoid allowing for two solutions of $|\vec{P}_{D^0}|$. (See appendix A for derivation.) This is by far the most common occurrence. Resolving this quadratic ambiguity comes down to finding a method to select the most desirable of the two solutions.

For this analysis, I use a combination of kinematics variables to calculate which solution has the higher probability of being correct. Figure 4.14 shows the two underlying kinematic distributions that are used to find the most probable of the two solutions. The first is the decay angle of the electron in the rest frame of the W. The

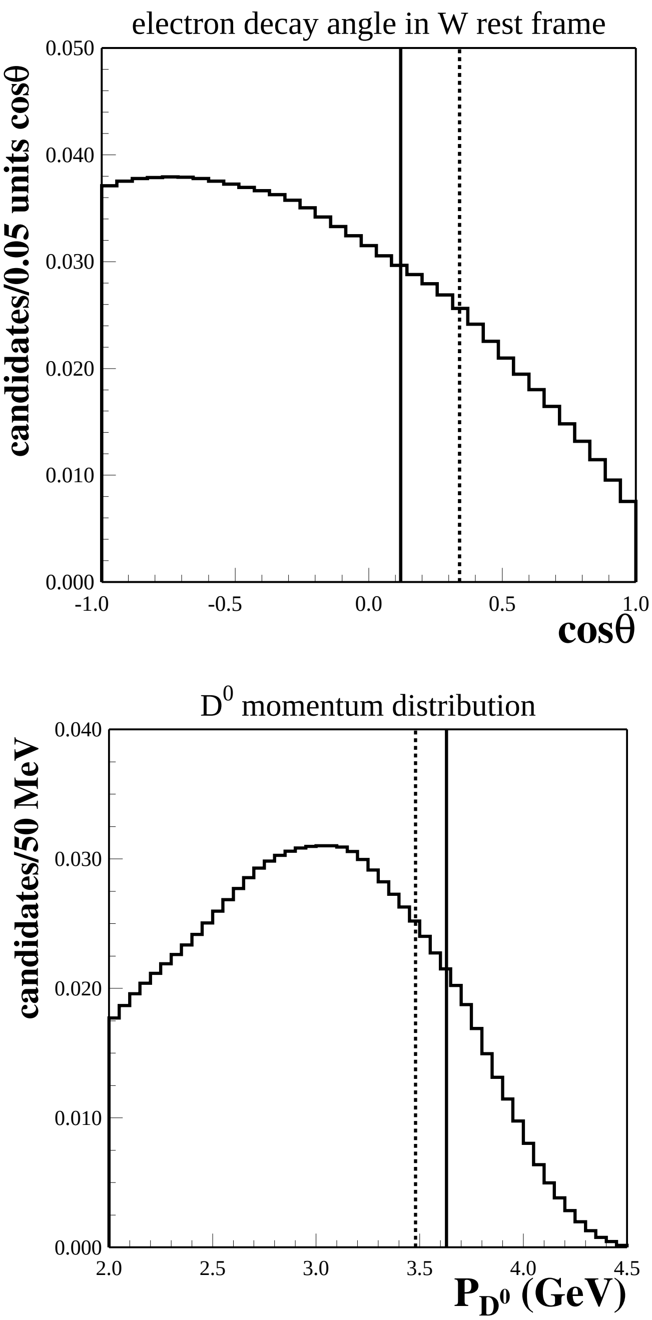

Figure 4.14: Each solution that results from the quadratic ambiguity in $E^2 - \vec{P}^2 = M^2_{D^0}$ has different values for electron decay angle in the W rest frame ($\cos\theta$) and magnitude of the D^0 momentum (shown in dashed and solid lines). In each plot, the solution's probability is taken to be proportional to the bin's occupancy in which the solution falls. The solution with the highest multiplicative probability is taken to be the best solution.

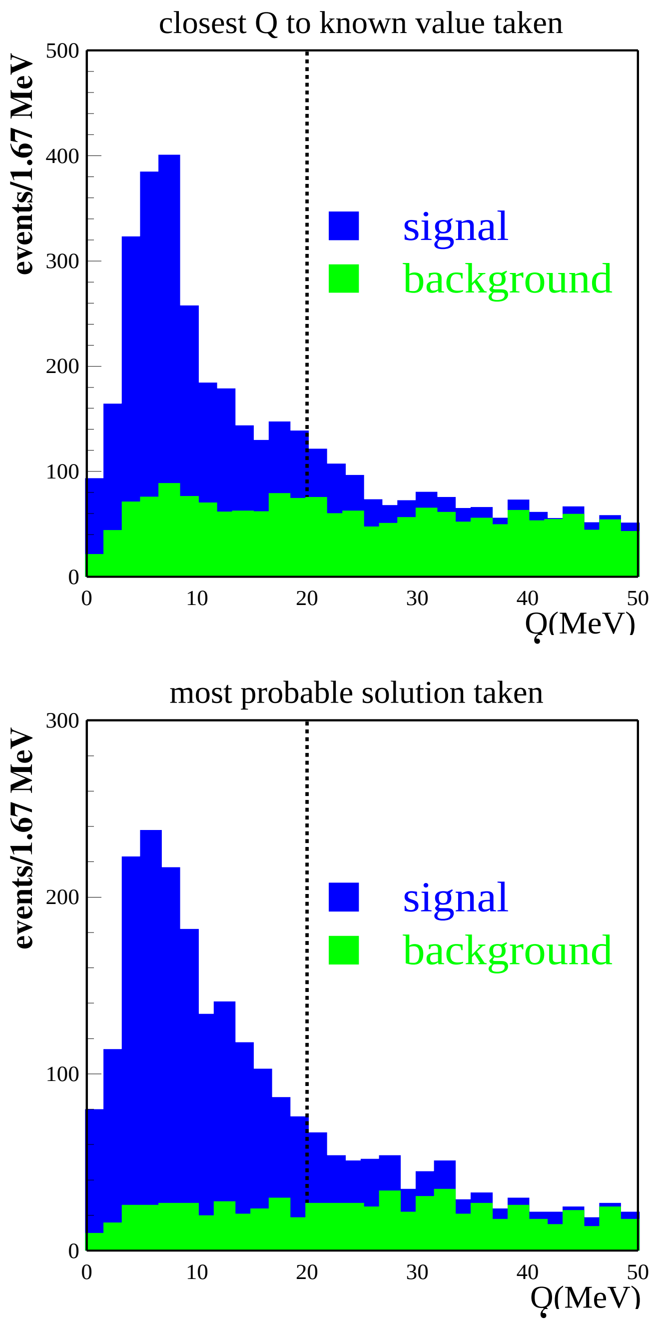

Figure 4.15: Comparison of Q distributions when the solution resulting in the closest to the known value of Q (5.84 MeV[58]) is taken(top) and when the most probable solution is taken. The signal:background ratio increases from 3.3:1 to 5.5:1 when the most probable solution is taken.

decay angle is defined as the angle between the electron and the projected direction of flight of its parent, the weak force mediator, W. In this distribution, the affect of the $V - A$ coupling can be seen to favor an electron that is traveling backward with the respect to the direction of the W. The second distribution used is the momentum spectrum of the D^0. Each plot is used as a probability density function with each solution falling into its respective bin. By multiplying the resulting probabilities, the most-likely solution is taken to be that with the highest value.

Commonly, the solution that results in the D^0, that when combined with the π_s candidate, gives the Q value closest to the known value of 5.84 MeV[58] is taken as the best solution. In a comparison of this method with the one described above, I found taking the closest Q tended to decrease the signal to background ratio in the signal region. For a monte carlo sample three times the size of the data sample, the ratio dropped from 5.5:1 for taking the most probable solution to 3.3:1 for taking the closest Q. This is easy to understand since taking the closest Q preferentially selects those $|\vec{P}_{D^0}|$ that give low Q.

Having calculated both its direction and magnitude, I now have $\vec{P}_{D^0}$. This method of reconstructing the $\vec{P}_{D^0}$ is double-checked by repeating the analysis with the hadronic decay mode $D^0 \to K\pi\pi^0$. By ignoring the π^0 and reconstructing the event as if it were a ν, we will check for consistency in the distributions of signal and background in both monte carlo and an appropriately tagged data sample. A similar method was followed with success in the analysis of $\mathcal{B}(D^+ \to K^{*0} l^+ \nu_l)$[54].

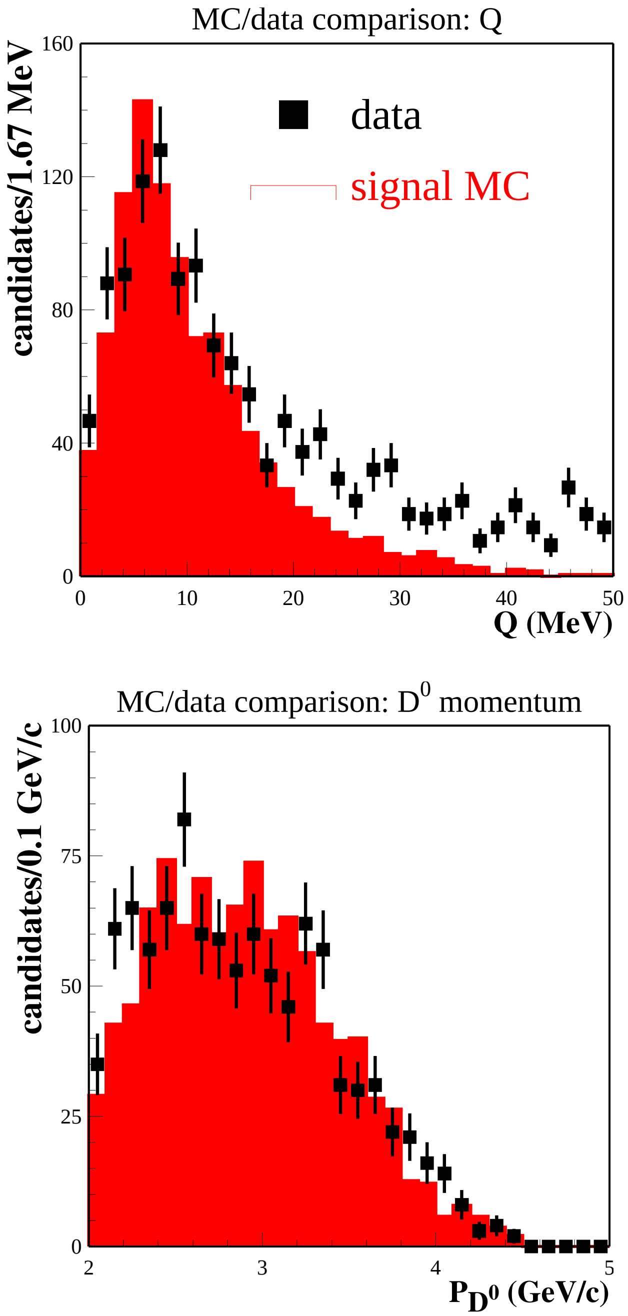

Figure 4.16: Monte carlo and data comparison of some of the variables pertinent to $\vec{P}_{D^0}$ reconstruction. A RS signal monte carlo sample is compared to RS data for the region $Q < 50$ MeV. Note backgrounds in data sample at higher Q values(top).

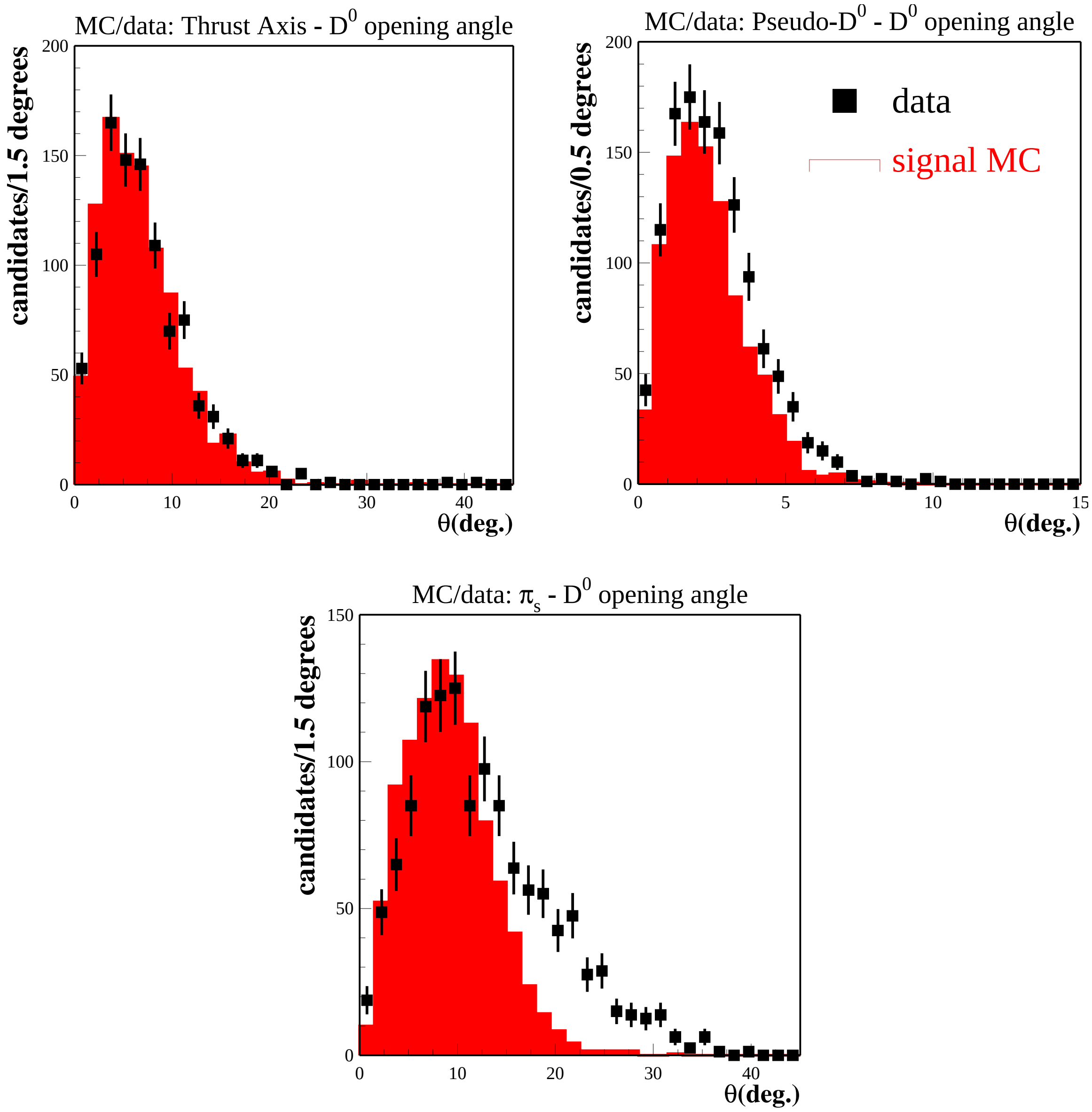

Figure 4.17: Comparisons of monte carlo and data distributions for the three indicators used in an optimized Best Guess of the D^0 direction. RS signal monte carlo sample is compared to RS data for the region $Q < 50$ MeV. Note the narrower opening angle distribution between the $\tilde{D}^0$ and the D^0 due to the weighting of the optimized Best Guess result, $\{\mathrm{TA}, \tilde{D}^0, \pi_s\} = \{1.0, 3.0, 0.3\}$.

This test is described in detail in Section 6.3. Until then though, a comparison of some pertinent distributions from the reconstruction technique for both monte carlo and data samples will have to suffice as a means of showing agreement between the two. The comparison of Q in Figure 4.16 shows good agreement between RS signal monte carlo and RS data candidates. Here, backgrounds in the data sample are seen to dominate as Q increases. Also, Figure 4.16 shows good agreement between MC and data for the momentum of the reconstructed D^0 candidate. Figure 4.17 is a MC/data comparison of the three indicators used to calculate the direction of the D^0. Each shows the opening angle distribution of the indicator with respect to the calculated D^0 direction for all candidates of $Q < 50$ MeV. Of note is the significantly narrower opening angle distribution between the $\tilde{D}^0$ and the D^0 due to the optimized Best Guess result being most heavily weighted towards the direction of the $\tilde{D}^0$. Also notable is the high background contribution from random π_s candidates(Figure 4.17).

4.4 Lifetime

One of the two variables to be used in a 2-dimensional binned likelihood fit is the lifetime of the D^0 candidate. Lifetime information can be used as a means of identifying "wrong-sign" signal events because the lifetime of mixed states is expected to be have a $t^2 \cdot e^{-t}$ dependence (Figure 2.4). We know the decay vertex of the D^0 (x_v, y_v, z_v) from the vertex of the electron and the charged π from the decay of the

K^*. We can use the K^*'s charged daughter because the K^* is short-lived. The D^*, which is also short-lived, decays within the beam ribbon. The resolution of the beam ribbon is 1.1 cm in the z-direction and 350 μm in the x-direction, but only 7 μm in the y-direction[21, 60, 61]. The narrowness of the luminous region in the y-direction is given by CESR lattice theory. Track resolution dominates attempts to measure this width directly, but beam parameters may be measured which do allow for a calculation of the beam width. This analysis has been done and the measured beam parameters result in value of the width of the luminous region in the y-direction that is in good agreement with CESR lattice theory[21, 60, 61]. Taking advantage of this narrow beam width in the y-direction, using only p_y and y_v allows for a D^0 flight distance resolution of about 98 μm in the monte carlo data sample with a minimum amount of vertexing constraints (Figure 4.18). The typical three-dimensional flight distance for a D^0 free of mixing is approximately 180 μm. This is equivalent to a lifetime resolution of $0.94\tau_{D^0}$.

4.5 Yield expectation

Table 4.2 contains a summary of all the cuts discussed in Section 4.1 and throughout the rest of Chapter 4. The only cut unmentioned is a minimum momentum cut on the $\tilde{D}^0$, $p_{\tilde{D}^0} > 2.05$ GeV. This cut is used to minimize the amount of combinatoric backgrounds resulting from errant combinations of the many low momentum tracks

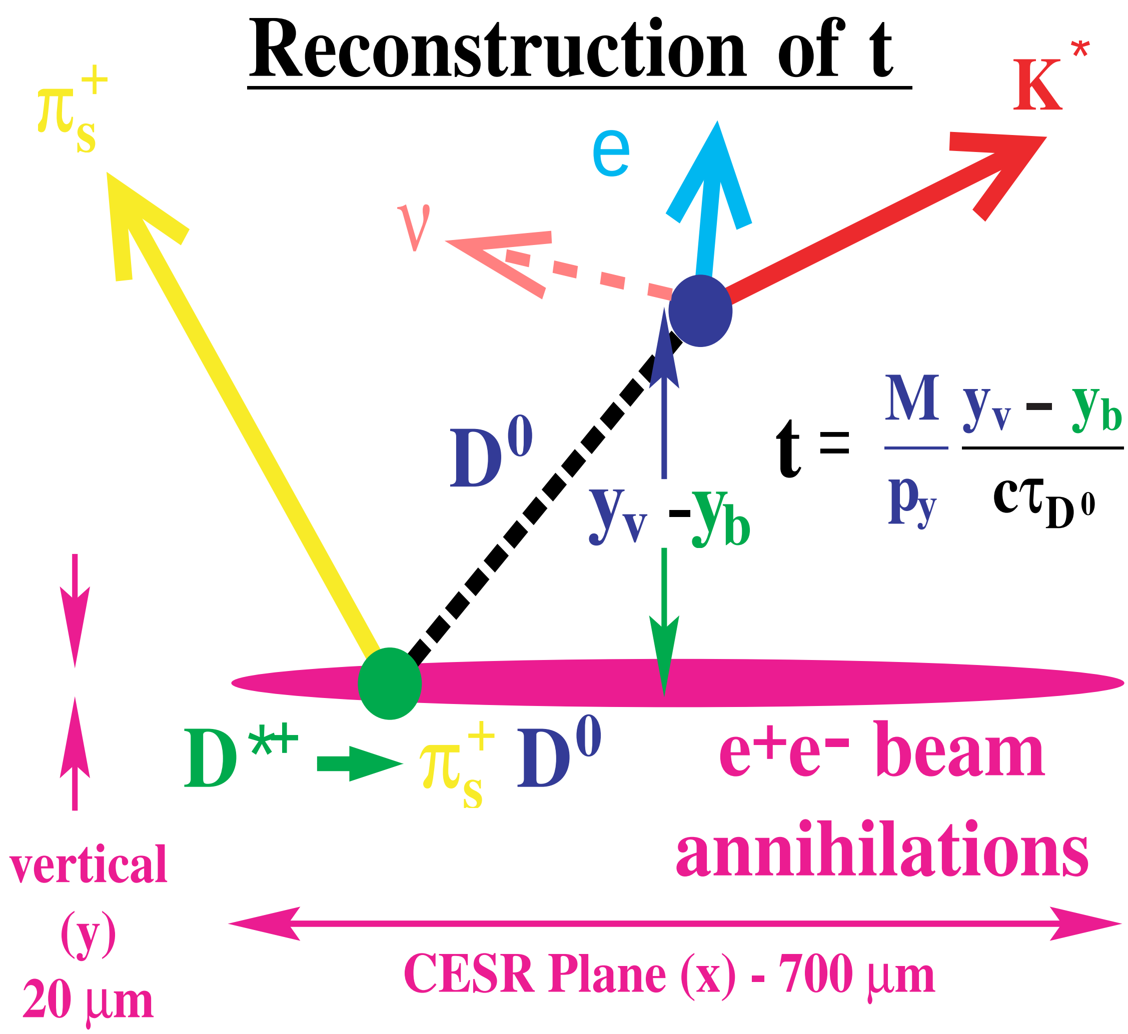

Figure 4.18: A calculation of the D^0 lifetime takes advantage of the narrow width of the beam ribbon in the y direction. By using only the y component of the D^0 decay vertex and the y position of the beam spot, a lifetime may be calculated with a limited number of vertex constraints. The calculation of the lifetime t is based on M, the mass of the D^0, p_y, the momentum of the D^0 in the y direction, y_v and y_b, the measured decay vertex of the D^0 and the known beam position along the y-axis, respectively, and $c\tau_{D^0}$, the decay length of the D^0.

available in most events. A comparison of the $p_{\tilde{D}^0}$ distributions in the monte carlo and the data sample is shown in Figure 4.19.

There are two factors associated with a calculation of the expected yield in any analysis. First, how many signal events are expected to be contained within the data set. This is a combination of the expected cross section to an inclusive state of some parent particle and the subsequent branching fractions through the signal state to the final observable states. At CLEO, this cross section has been measured at $\sigma(e^+e^- \to D^{*+}X) \approx 660$ pb[62] and the subsequent branching fractions are listed in Table 4.3. Therefore,

$$\sigma\mathcal{L}\mathcal{B} = (660\,\text{pb})(9000\,\text{pb}^{-1})(0.00235) \approx 14,000 \text{ signal events} \tag{4.8}$$

where $\mathcal{L}$ is the total integrated luminosity of CLEOII.V and $\mathcal{B}$ is the overall branching fraction from Table 4.3.

Initially, the intent of this analysis was to include the decay $D^0 \to K^*\mu\nu$ as well. However, to achieve good separation of signal from background, it was necessary to require that the μ candidate had passed through at least five layers of the muon detector. This is effectively a hard cut on the momentum of the μ candidate, $p_\mu > 1.6$ GeV. This left only a tiny fraction of the original μ available for reconstruction since the $V - A$ coupling favors softer leptons. In addition, it was thought that the decay of the K^* to $K\pi^0$ could also be included in the analysis, but the combination of poor resolution for low p_{π^0} and a large missing p_ν allowed for many random combinatoric

Table 4.2: Summary of kinematic and event selection cuts used in this analysis. Items of note are requirements on vertexed tracks to have at least two silicon hits in both the $r-\phi$ and z directions, minimum p_e below the existing Cornell Electron Identification package limit requires changes to electron selection cuts, and further electron fakes are excluded with γ conversion, $\cos\theta_e^{\pi_s}$, and $\cos\theta_e^{\pi_{K^*}}$ cuts. Cuts are defined in Sections 4.1 and 4.2.

type	*variable*	*limit*
global	KLASGL	$= 10$
	NTRKCD	≥ 5
	R2GL	> 0.23
track selection	TNG	≥ 0
	KINCD	$= 0$
	dredge	no
	z-escape	no
vertexed tracks	SV $r-\phi$ hits	≥ 2
	SV z hits	≥ 2
electron selection	semi-circle enclosing	
	$-2.0 <$ SGELDI < 2.0	
	$0.90c <$ E/P $< 1.03c$	
	γ conversion	no
	$\cos\theta_e^{\pi_s}$	< 0.9965
	$\cos\theta_e^{\pi_{K^*}}$	< 0.9986
	p_e	> 330 MeV
K_S^0 selection	mass window	16 MeV
K^* selection	mass window	60 MeV
kinematic	p_{π_s}	180-400 MeV
	$p_{\tilde{D}^0}$	> 2.05 GeV

Table 4.3: Knowing $\sigma(e^+e^- \rightarrow D^{*+}X) \approx 660$ pb[62] and the branching fractions below, I expect the 9000 pb^{-1} of CLEOII.V data to yield $\approx$14,000 signal events. The π_s, the electron and the three π's from the K^* and subsequent K^0_S decays are the five tracks used in event reconstruction.

Mode								**Fraction**[3]
D^{*+}	$\longrightarrow$	$D^0\,\pi_s^+$						0.683
		D^0	$\longrightarrow$	$K^{*-}\,e^+\,\nu$				0.0201
				K^{*-}	$\longrightarrow$	$K^0_S\,\pi^-$		0.250
						K^0_S	$\longrightarrow$ $\pi^+\,\pi^-$	0.686
							Total	0.00235

backgrounds.

The second factor is the overall event reconstruction efficiency. This is dependent on, among other things, the geometry of the detector, the intrinsic acceptance in its elements, and the cuts used in the analysis to select signal and exclude backgrounds.

Table 4.4 lists the cuts used in the analysis and their corresponding efficiencies. The efficiencies are based on the cuts being taken successively as listed so that an overall reconstruction efficiency can be calculated by simply multiplying each cut's corresponding efficiency. Some of the lowest efficiencies are the K^0_S acceptance (59%), the π_s acceptance (58%) and the overall electron acceptance and selection (38%).

Multiplying the 14,000 signal events from Eqn. 4.8 by the overall reconstruction efficiency of 4.2% yields approximately 590 signal events when reconstruction is complete. This is in good agreement with the number of RS signal events found in a fit to the data, 638 ± 51(see Figure 5.9).

A further comparison of the monte carlo and data samples is shown in Fig-

Table 4.4: To get the efficiencies, the cuts are taken successively as they are listed in the table so the total efficiency represents the complete reconstruction efficiency. Therefore, starting with the expected 14,000 signal events (from Table 4.3), I should expect to reconstruct about 590 signal events. This is in good agreement with the fit results shown in Figure 5.9, 638 ± 51.

Cut	**Efficiency**
Event classification and minimum track #	0.98
Event geometry (R2GL)	0.88
$P_e > 330$ MeV and track quality	0.64
electron selection	0.60
K_S^0 reconstruction	0.59
π_{K^*} track quality	0.76
K^* mass cut	0.70
$p_{\tilde{D}^0} > 2.05$ GeV	0.71
p_{π_s} cuts and track quality	0.58
D^0 reconstruction technique	0.98
Total	0.042

ures 4.19, 4.20 and 4.21. Variables upon which cuts are applied to exclude backgrounds are shown in Figures 4.19 and 4.20. All cuts are applied to both sets of data except those of the plotted variable. Backgrounds can be seen to enhance the data distributions at low values of p_{π_s} and $p_{\tilde{D}^0}$; cuts are applied to both of these variables (see Table 4.2) in such a way as to maximize the ratio of signal-squared over background in the monte carlo. Plots are based on approximately 150,000 signal monte carlo events and the 9.0 fb^{-1} of CLEOII.V data. Monte carlo plots are normalized to the area of the data plots for comparison.

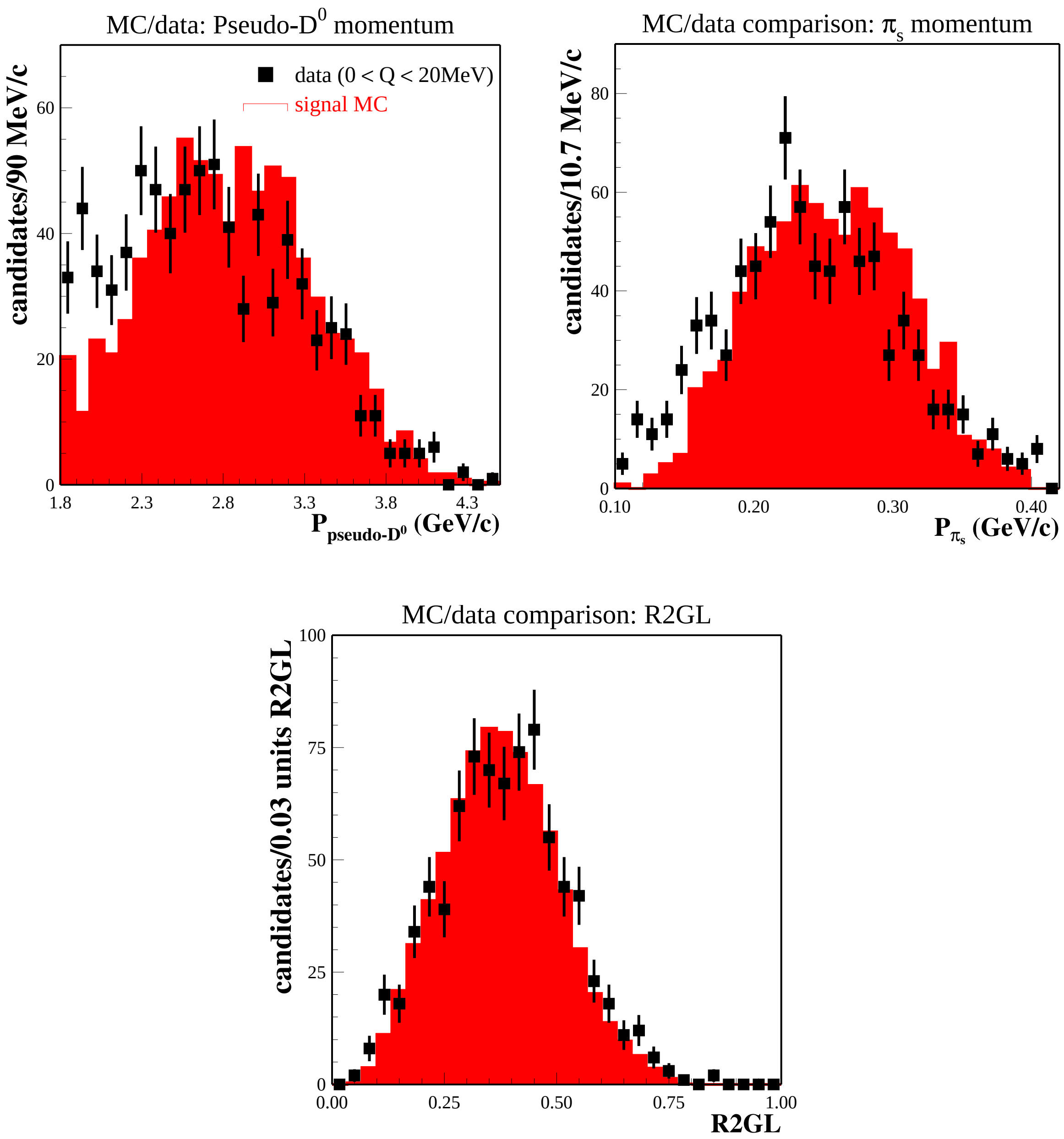

Figure 4.19: Comparisons of RS signal monte carlo and data distributions for some of the variables subject to cuts in the analysis. All cuts, except those of the plotted variable, are applied to both sets of data. Data plots are based on RS candidates in the signal region, $Q < 20$ MeV. Backgrounds are evident in the data distributions in low momentum ranges of the $\tilde{D}^0$ and the π_s.

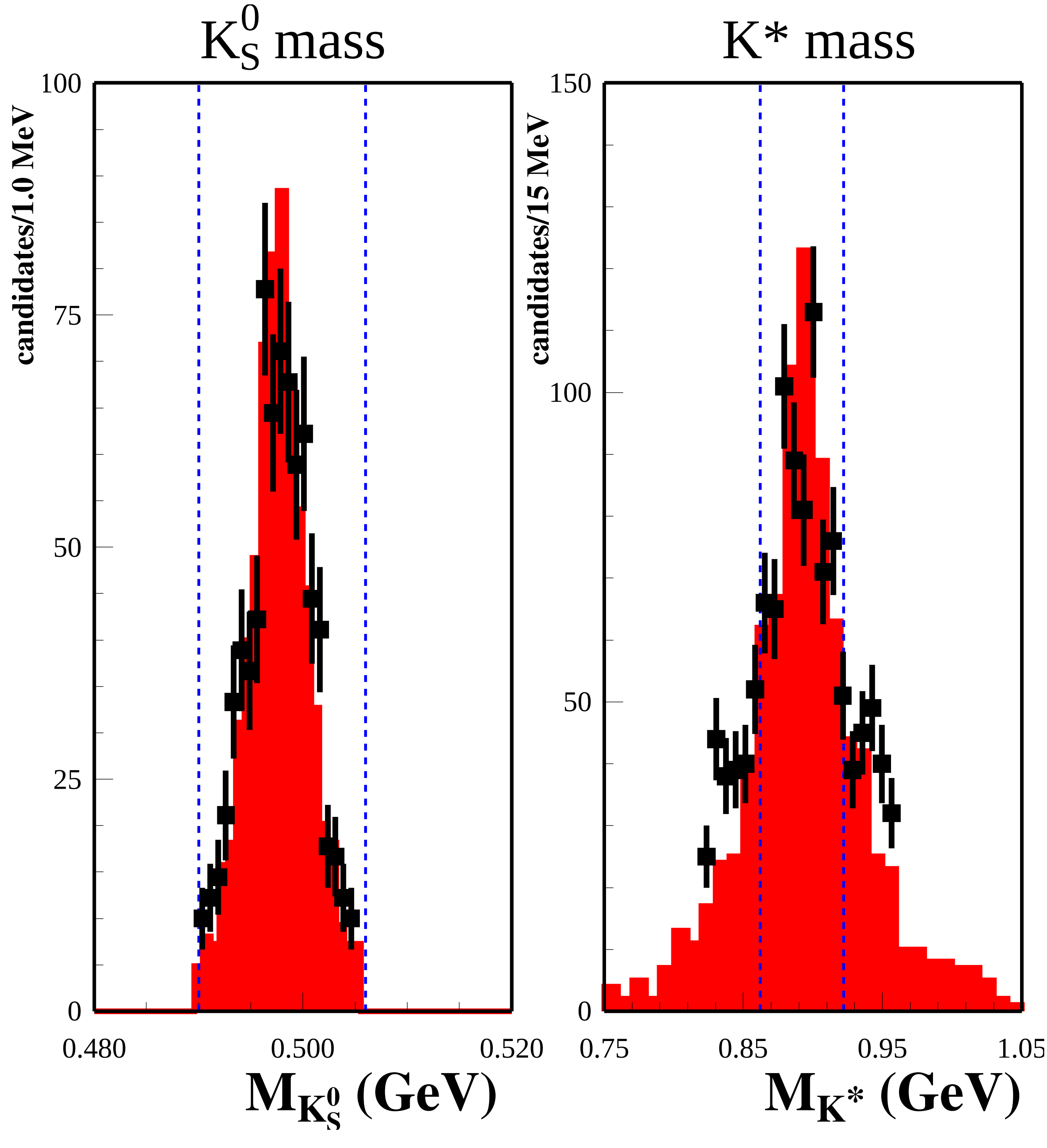

Figure 4.20: Comparisons of RS signal monte carlo(solid histogram) and data(points) distributions for the K_S^0 and the K^* masses to illustrate that the distributions in MC and data are qualitatively the same. Dashed lines indicate where the mass cuts are placed; ± 8 MeV and ± 30 MeV(1.2σ) around the nominal K_S^0 and K^* mass, respectively. In the case of the K_S^0, the cuts used to initially extract candidate events from data tapes are the same as the final analysis cuts.

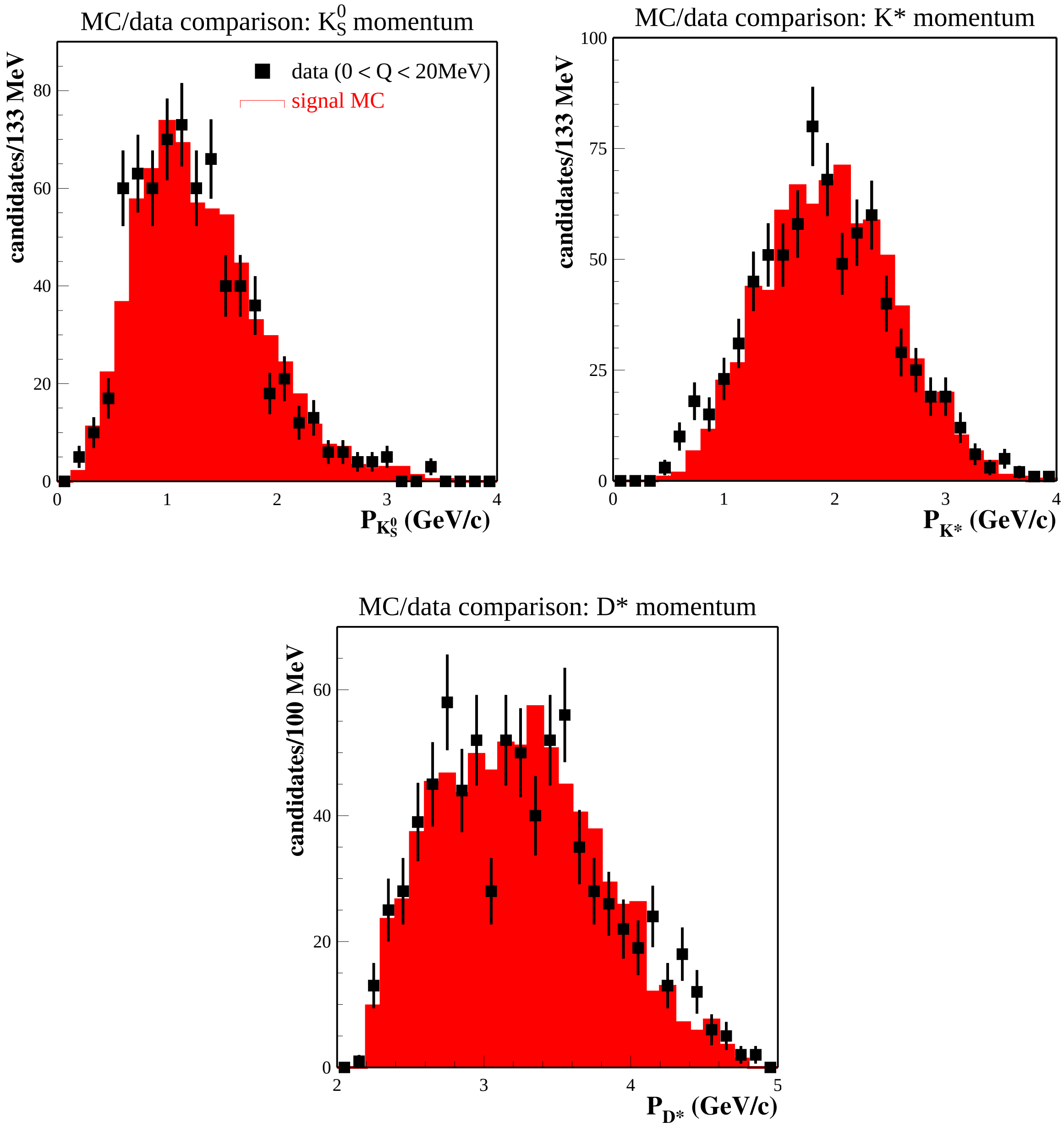

Figure 4.21: Comparisons of RS signal monte carlo and data distributions for some notable kinematic variables. These variables are not cut on in the analysis. Data plots are based on RS candidates in the signal region, $Q < 20$ MeV. Backgrounds are evident in the data distributions in low momentum ranges of the $\tilde{D}^0$ and the π_s and at low R2GL values.

Chapter 5

Fitting

A two-dimensional binned maximum likelihood fitting technique is used. The two dimensions are the energy released in the decay of the D^* (Q) and the lifetime of the D^0 candidate in units of D^0 lifetimes (t understood to be $\frac{t}{\tau_{D^0}}$). Fundamentally, only two functions are used to describe all components: 1) a two-parameter threshold function is used to describe components in the Q dimension

$$\mathcal{F}(Q; p, s) \propto Q^p e^{sQ} \tag{5.1}$$

and 2) an exponential convolved with a resolution Gaussian $g(\sigma)$ in the lifetime direction

$$\mathcal{H}(t; \tau, \sigma) \propto \underbrace{[t^2]}_{WS} e^{-\frac{t}{\tau}} * g(\sigma) \tag{5.2}$$

5.1 Fitting for signal

The RS signal has a sharp Q and lifetime exponential of mean $1\tau_{D^0}$ with resolution of also about $1\tau_{D^0}$. To account for badly measured decay distances, mainly caused by failures in the neutrino reconstruction method in about 5% of signal events, the lifetime part also includes a second piece with a resolution of $5\tau_{D^0}$. All parameters are derived from a MC data set roughly equivalent to three times the CLEOII.V data set. The 2-dimensional plots of events reconstructed as RS and WS in the MC data set are shown, along with projections onto the respective axes, in Figures 5.3 and 5.4 on pages 94 and 95, respectively. Results from fits to this MC data set are shown in Figures 5.5 and 5.6 and Table 5.2 on pages 96, 97 and 91, respectively. A qualitative description of the functions used to fit signal and background is contained in Table 5.1 on page 91. The normalizations of both pieces are allowed to float when fitting the data. For the WS signal the lifetime distribution is modulated by t^2. The wide Gaussian lifetime piece is fixed to zero for the fit to WS. It was floated as a systemic check and the contribution to the systematic error was found to be negligible.

5.2 Fitting for background

The backgrounds come mainly from two sources. The first is combinatoric backgrounds from $e^+e^- \to u\overline{u}, d\overline{d}, s\overline{s}, B\overline{B}$ events. Comprised mainly of stable or short-lived particles generated within the luminous region, these tend to reconstruct as having very low lifetimes. The second is $e^+e^- \to c\overline{c}X$ events with misreconstruction of a D^0 through random tracks in the events. These reconstructions tend to have some fraction of a D^0 lifetime.

Three 2-dimensional functions are used to describe the backgrounds for both the RS and WS cases with all parameters, again, derived from a monte carlo analysis. The backgrounds are considered to be made of three separate pieces. A piece with no lifetime, a piece that has some fraction of a D^0 lifetime, and a underlying wide flat piece to account for random combinatorics and failures of the reconstruction technique.

In general, in the Q dimension, the backgrounds have a slower turn on (p) and lower slope (s) than the signal parameters. This can be seen in the monte carlo sample in Figures 5.5 and 5.6. In addition, the zero-lifetime backgrounds are well modeled with $s = 0$ resulting in a simplification of the threshold function to a power law. This results in a flatter overall function in the signal region, $0 < Q < 20$ MeV. Examples of the functions used to describe both the Q and lifetime dimensions can be seen in Figures 5.1 and 5.2, respectively.

5.3 What the fits look like

The 2-dimensional plots of events reconstructed as RS and WS in the 9.0 fb^{-1} of CLEOII.V data are shown, along with projections onto the respective axes, in Figures 5.7 and 5.8 on pages 98 and 99, respectively. Results from a fit to the data set for RS signal are shown in Figure 5.9 on page 101 and projections onto the respective axes are shown in Figure 5.10 on page 102. Results from a fit to the data set for WS

Table 5.1: Qualitative summary of functions used for RS and WS signal and background. Examples of these functions are shown in Figures 5.1 and 5.2.

	dimensions for 2D fit		
fit to	*Q*	*Lifetime*	*source*
RS sig	sharp threshold	$e^{-\Gamma t}$ convolved with a narrow resolution Gaussian, $<\tau_{RS}>\approx\tau_{D^0}$	
		wide Gaussian, $<\tau>=<\tau_{RS}>$	signal
RS bkg	wide threshold	$e^{-\Gamma_{RS}^{bkg}t}$ convolved with a wide resolution Gaussian, $<\tau>\approx 0.5\tau_{D^0}$	
		wide Gaussian, $<\tau>\approx 0.5\tau_{D^0}$	$c\overline{c}$
	power law	resolution Gaussian short-lived candidates, $<\tau>=0$	$u\overline{u}, s\overline{s}, d\overline{d}, B\overline{B}$
WS sig	sharp threshold	$t^2e^{-\Gamma t}$ convolved with a narrow resolution Gaussian, $<\tau>\approx 3\tau_{RS}$	signal
WS bkg	wide threshold	$e^{-\Gamma_{WS}^{bkg}t}$ convolved with a wide resolution Gaussian, $<\tau>\approx 0.5\tau_{D^0}$	
		wide Gaussian, $<\tau>\approx 0.5\tau_{D^0}$	$c\overline{c}$
	power law	resolution Gaussian for short-lived candidates, $<\tau>=0$	$u\overline{u}, s\overline{s}, d\overline{d}, B\overline{B}$

Table 5.2: Parameters derived from 20.0 fb^{-1} of MC data for functions used to fit RS and WS signal and background in the data. These parameters correspond to those described in Equations 5.1 and 5.2.

for fit to	$\mathcal{F}(Q;p,s)$		$\mathcal{H}(t;\tau,\sigma)$	
	p	$s(MeV^{-1})$	$\tau(\tau_{D^0})$	$\sigma(\tau_{D^0})$
RS sig	0.8733 ± 0.0105	-0.1616 ± 0.0018	1.0155 ± 0.0553	0.9389 ± 0.0460
	0.8733 ± 0.0105	-0.1616 ± 0.0018	1.0155 ± 0.0553	5
RS bkg	0.2258 ± 0.0117	-0.0185 ± 0.0013	0.6621 ± 0.0920	1.1713 ± 0.0808
	0.2258 ± 0.0117	-0.0185 ± 0.0013	0.6621 ± 0.0920	5
	0.2018 ± 0.0206	0	0	1.1903 ± 0.1262
WS sig	0.8733 ± 0.0105	-0.1616 ± 0.0018	1.0155 ± 0.0553	0.9389 ± 0.0460
WS bkg	0.3639 ± 0.0146	-0.0268 ± 0.0016	0.4943 ± 0.1018	1.2585 ± 0.1057
	0.3639 ± 0.0146	-0.0268 ± 0.0016	0.4943 ± 0.1018	5
	0.2852 ± 0.0228	0	0	1.0841 ± 0.0791

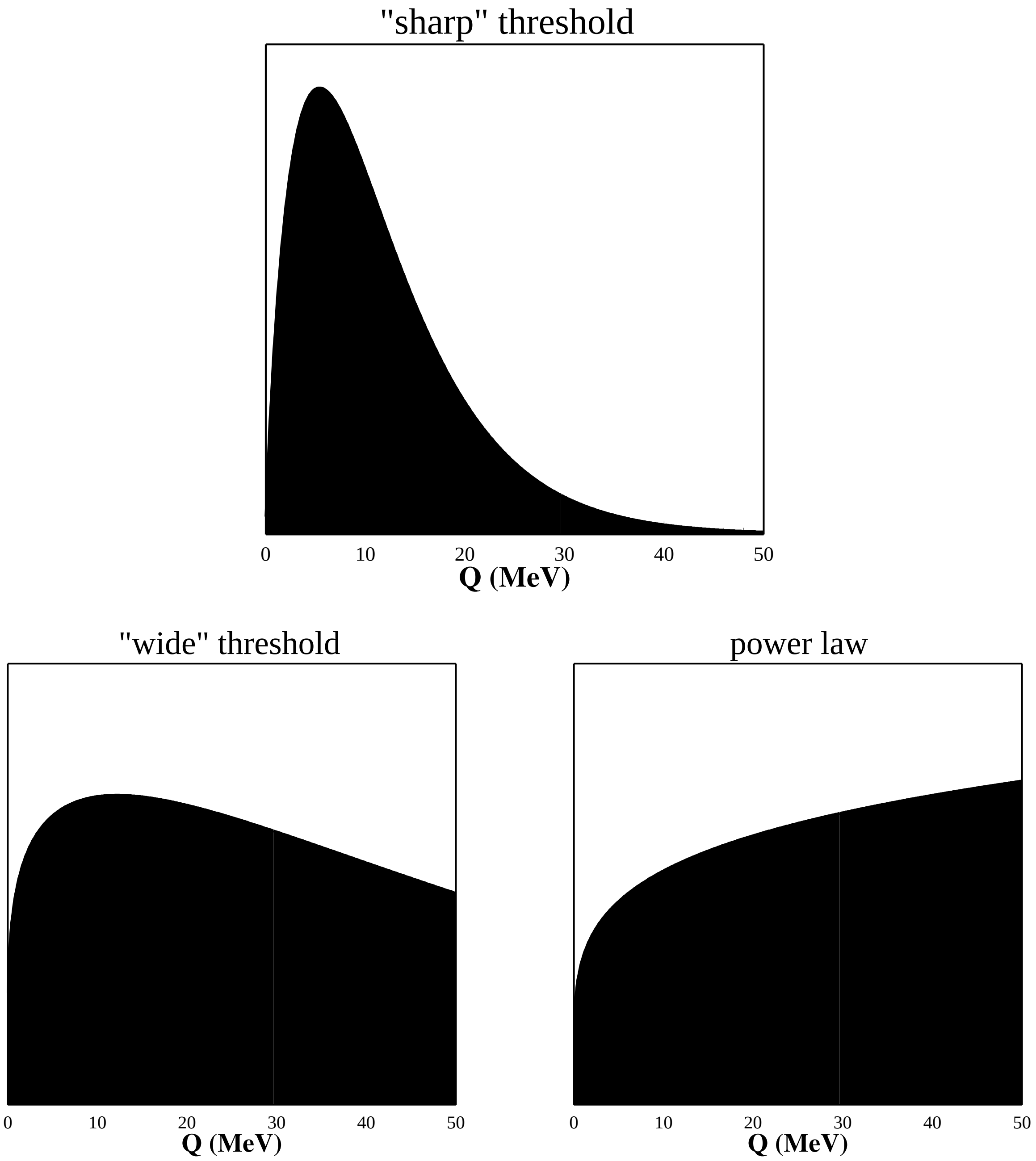

Figure 5.1: Examples of the three functions used for fitting the Q dimension in the 2-dimensional fit of Q and lifetime. The top plot is a "sharp" threshold used to fit for RS and WS signal, while "wide" threshold and power law functions are used to fit for backgrounds. The power law function is equivalent to a threshold function with $s = 0$, as in Equation 5.1 and Table 5.2

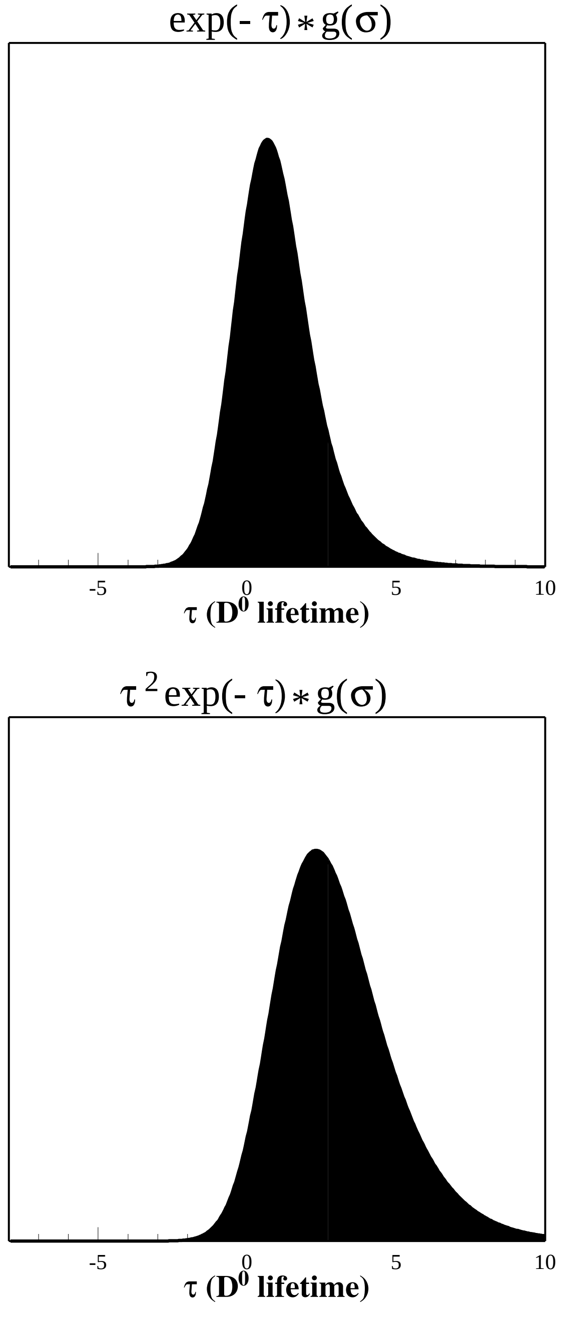

Figure 5.2: Examples of the two functions used for fitting the τ dimension in the 2-dimensional fit of Q and lifetime. Both are exponential functions of τ convolved with a resolution Gaussian. However, the functions used to fit for the lifetimes of mixed decays (WS signal) have an added factor that is second order in τ as in Equation 5.2 and Table 5.2

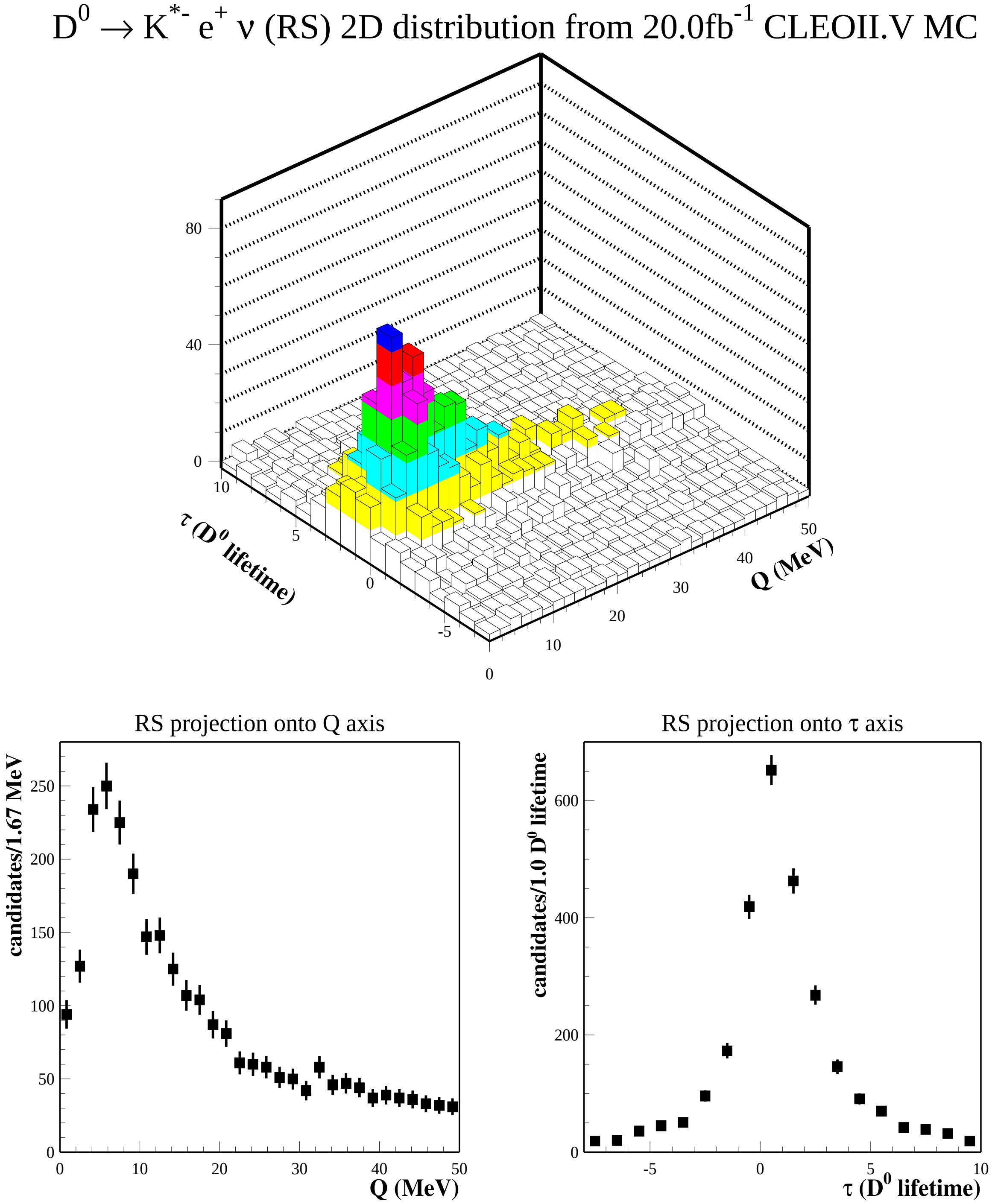

Figure 5.3: Two-dimensional display(top) and projections of Q and τ of RS monte carlo. A clear RS signal peak can be seen in Q.

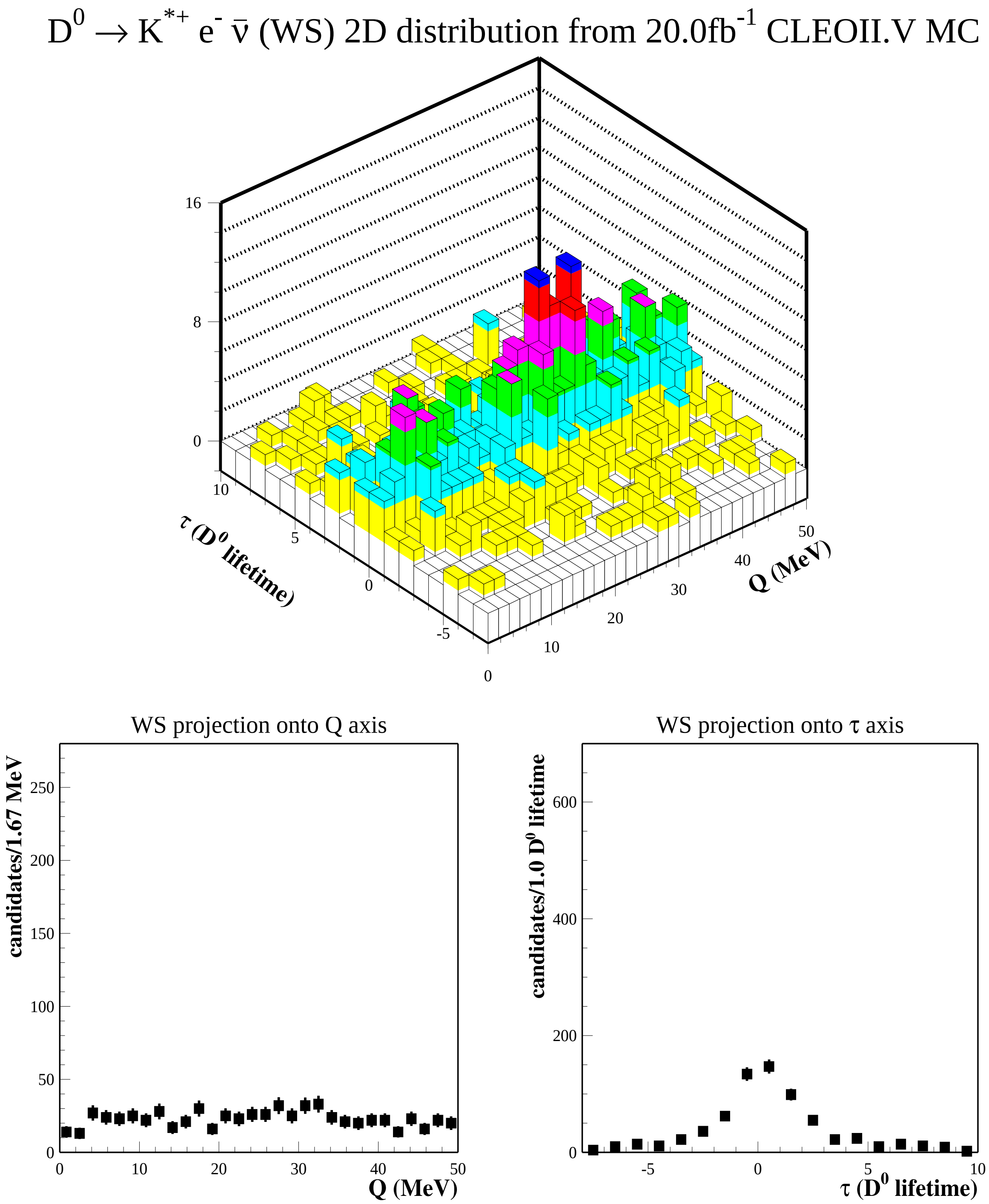

Figure 5.4: Two-dimensional display(top) and projections of Q and τ of WS monte carlo data. WS projections are suppressed to place on same scale as RS projections in Figure 5.3.

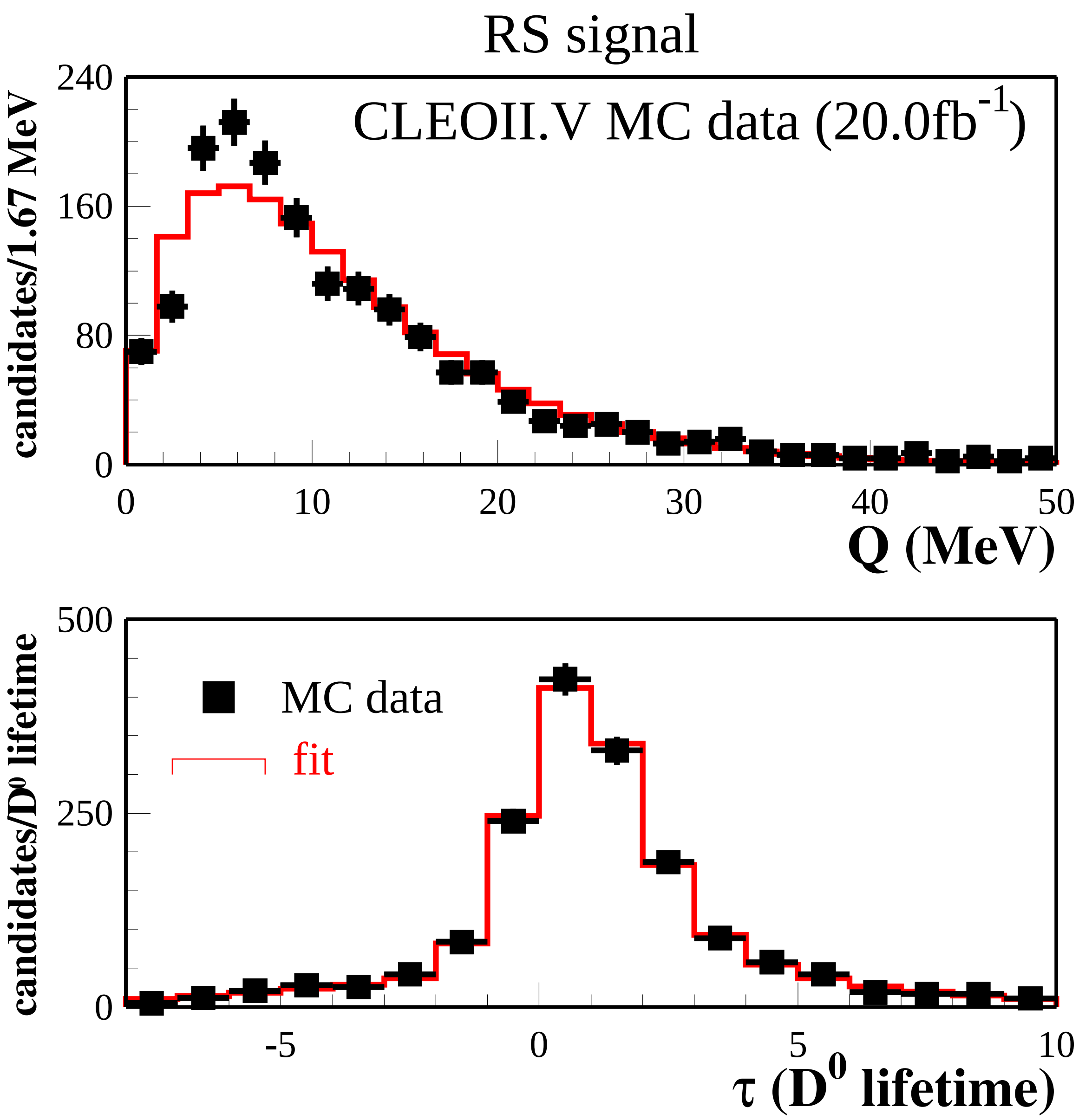

Figure 5.5: Projections from fits to RS signal to illustrate the functions described in Tables 5.1 and 5.2. The confidence level of this likelihood fit is 0.183%.

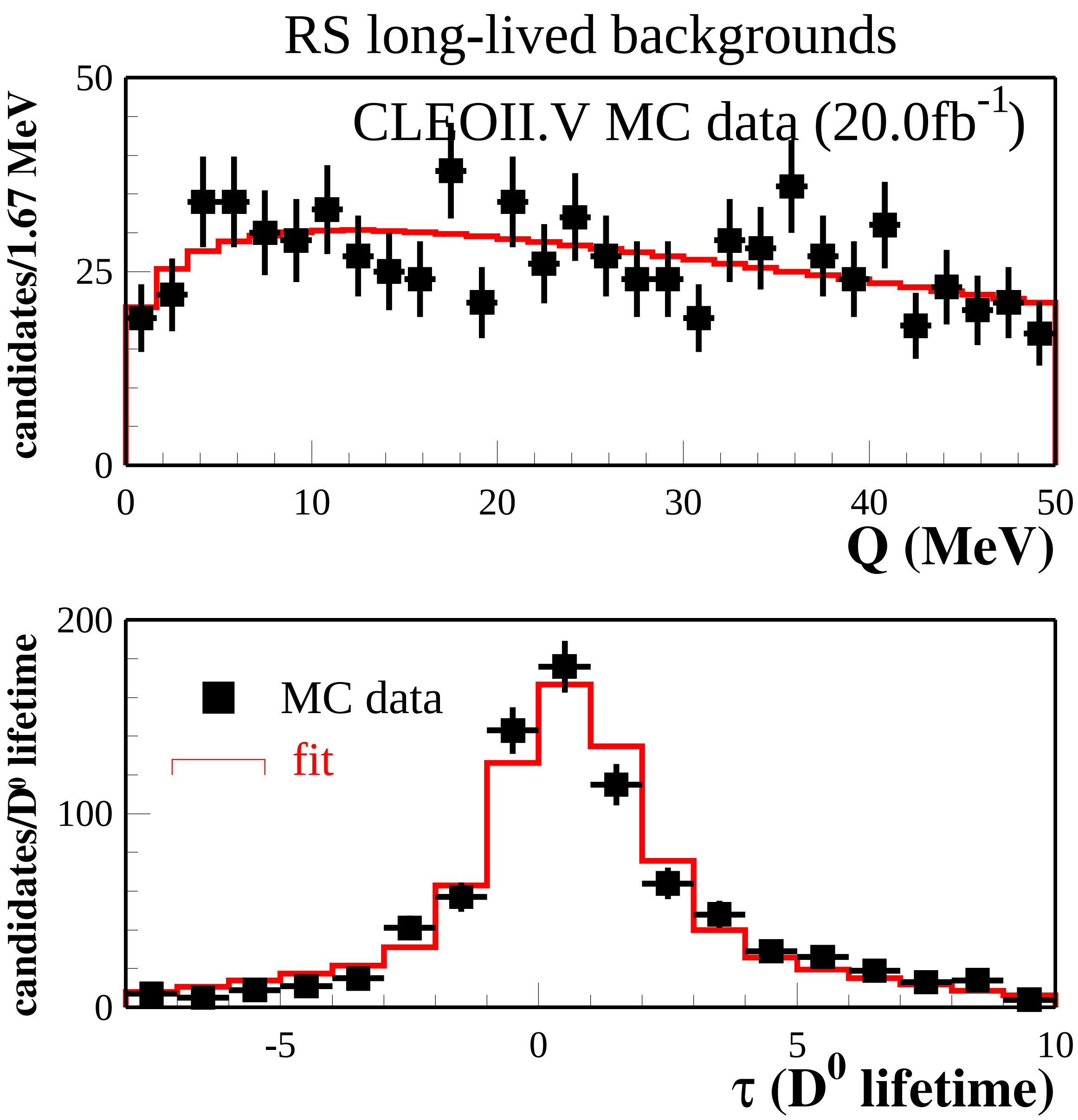

Figure 5.6: Projections from fits to RS long-lived backgrounds to illustrate the functions described in Tables 5.1 and 5.2. The confidence level of this likelihood fit is 86.8%.

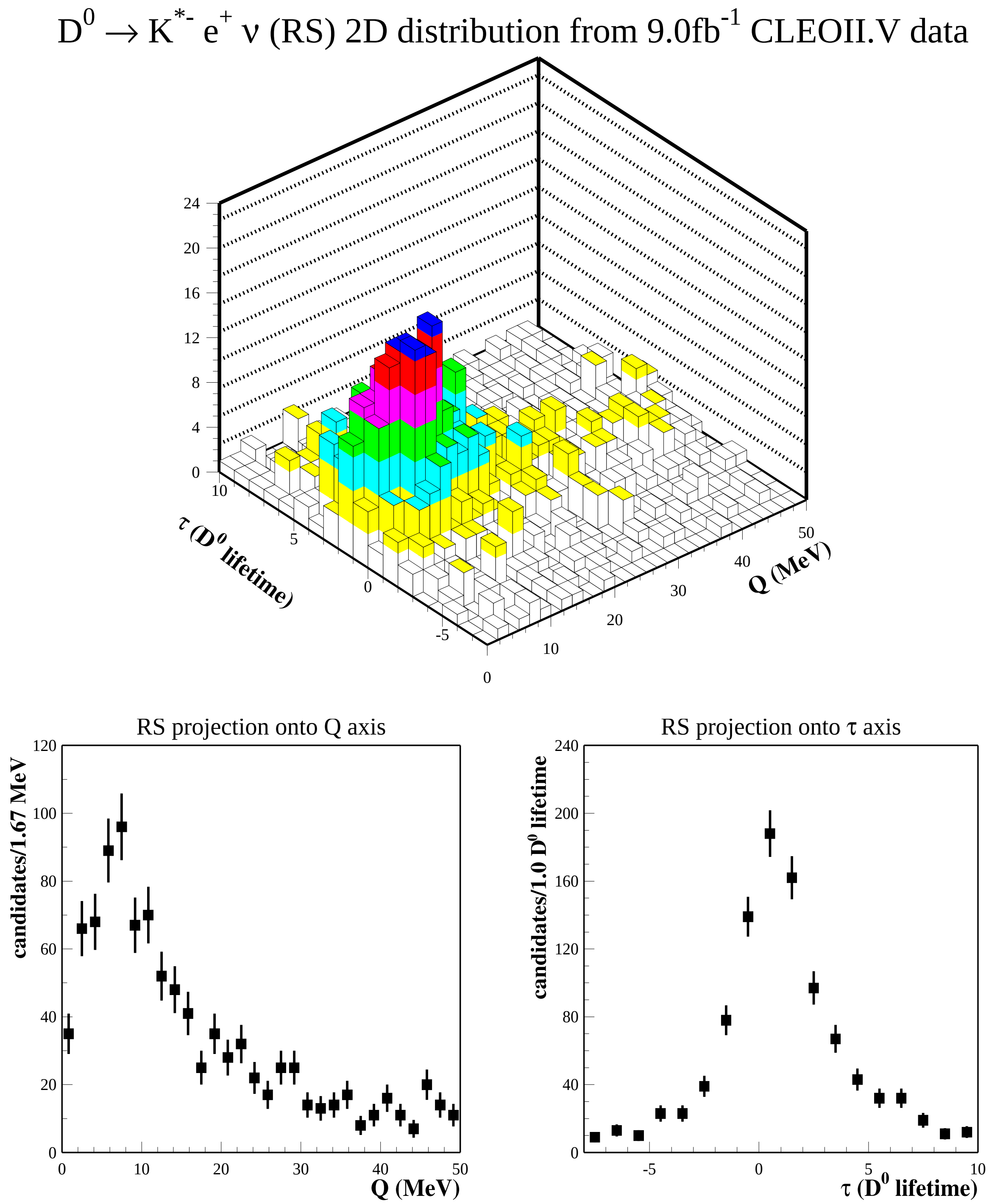

Figure 5.7: Two-dimensional display(top) and projections of Q and τ of RS data. A clear RS signal peak can be seen in Q.

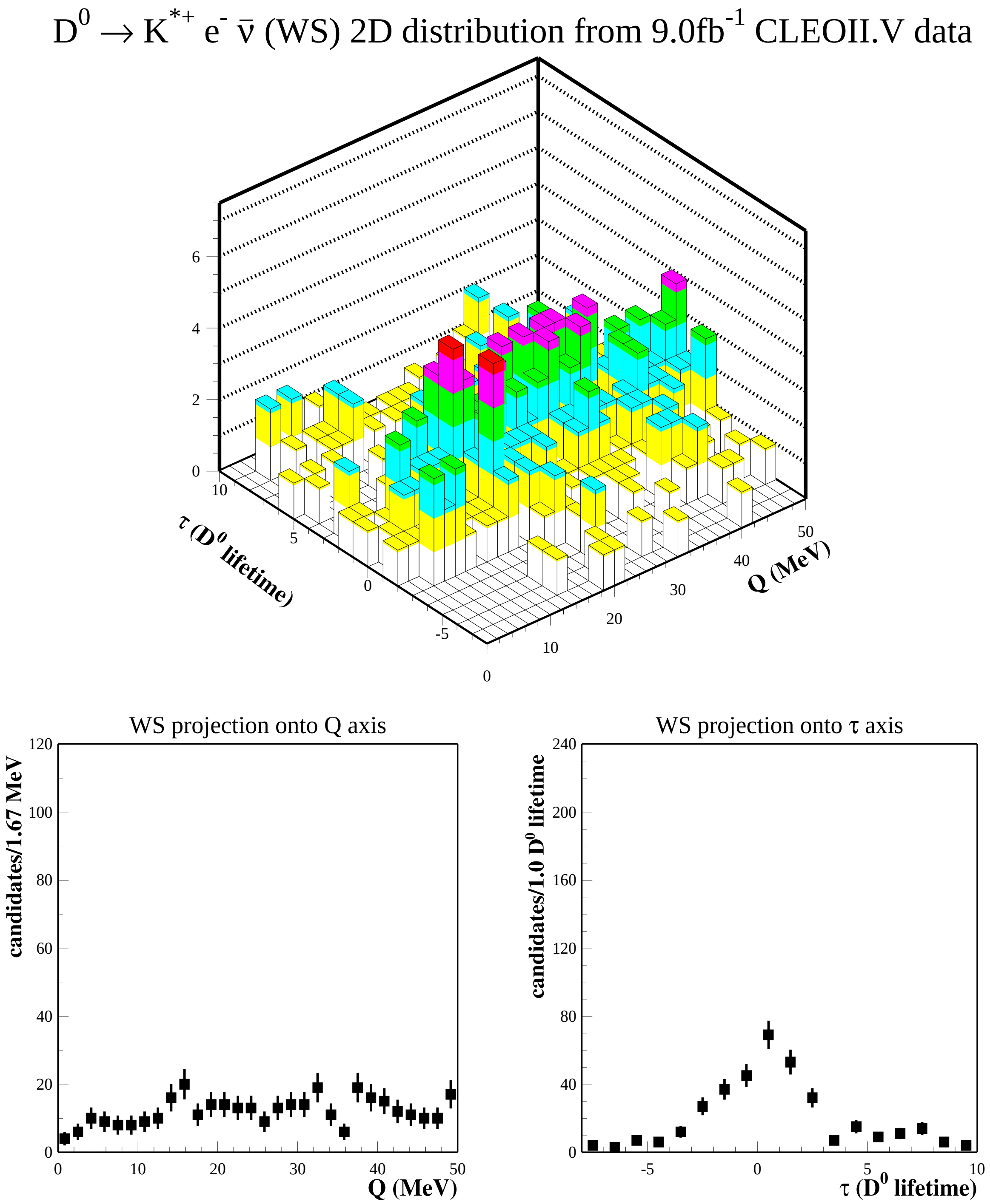

Figure 5.8: Two-dimensional display(top) and projections of Q and τ of WS data. An absence of WS signal is evident in the 2D plot at low Q and $< \tau > \approx 3\tau_{D^0}$. WS projections are suppressed to place on same scale as RS projections in Figure 5.7.

signal are shown in Figure 5.11 on page 103 and projections onto the respective axes are shown in Figure 5.12 on page 104.

A fit to the RS data sample yields 638 ± 51 candidates. A fit to the WS data sample yields -30.42 ± 8.17 candidates. This result is unphysical, so the WS signal piece is constrained to be ≥ 0 and refit. The confidence level drops, 29.2% $\rightarrow$ 15.8%, but the fit is still good. The likelihood distributions are checked for the two fits, shown in Figure 5.13, and it is observed that the errors calculated by MINUIT are correct. In Figure 5.13, a one unit change in $-ln(L/L_{max})$ corresponds to a one sigma error[57]. It was a concern that the unconstrained fit result is 3σ negative but the systematic checks described in the next chapter indicate that the function shapes used are appropriate for a description of the background.

I calculate the upper limit on R_{mix} using the more conservative result obtained from the constrained fit. This is equivalent to 1.99 WS signal events or $R_{mix} = 0.00 + 0.31$.

MINUIT Likelihood Fit to Plot 634&1

RS: $D^{*+} \to D^0 \pi^+, D^0 \to K^{*-} e^+ \nu$

File: *r2datap1.rzn 5-FEB-2002 11:14

Plot Area Total/Fit 997.00 / 997.00 Fit Status 3

Func Area Total/Fit 996.98 / 996.98 E.D.M. 4.548E-06

Likelihood = 562.6

χ^2= 544.1 for 540 - 5 d.o.f., C.L.= 38.3%

Errors		Parabolic	Minos	
signal				
Function 1:				
normalization	20.858	± 2.130	- 2.126	+ 2.149
* p	0.87332	± 0.0000E+00	- 0.0000E+00	+ 0.0000E+00
* s	-0.16159	± 0.0000E+00	- 0.0000E+00	+ 0.0000E+00
* τ	1.0155	± 0.0000E+00	- 0.0000E+00	+ 0.0000E+00
* σ	0.93894	± 0.0000E+00	- 0.0000E+00	+ 0.0000E+00
Function 2:				
normalization	1.3551	± 0.1703	- 0.1684	+ 0.1727
* p	0.87332	± 0.0000E+00	- 0.0000E+00	+ 0.0000E+00
* s	-0.16159	± 0.0000E+00	- 0.0000E+00	+ 0.0000E+00
* τ	1.0155	± 0.0000E+00	- 0.0000E+00	+ 0.0000E+00
* σ	5.0000	± 0.0000E+00	- 0.0000E+00	+ 0.0000E+00
background				
Function 5:				
normalization	0.33531	± 0.2678	- 0.2684	+ 0.2721
* p	0.20178	± 0.0000E+00	- 0.0000E+00	+ 0.0000E+00
* σ	1.1903	± 0.0000E+00	- 0.0000E+00	+ 0.0000E+00
Function 3:				
normalization	1.9466	± 1.715	- 1.708	+ 1.755
* p	0.22575	± 0.0000E+00	- 0.0000E+00	+ 0.0000E+00
* s	-1.84573E-02	± 0.0000E+00	- 0.0000E+00	+ 0.0000E+00
* τ	0.66206	± 0.0000E+00	- 0.0000E+00	+ 0.0000E+00
* σ	1.1713	± 0.0000E+00	- 0.0000E+00	+ 0.0000E+00
Function 4:				
normalization	0.54195	± 7.6954E-02	- 7.4633E-02	+ 7.9441E-02
* p	0.22575	± 0.0000E+00	- 0.0000E+00	+ 0.0000E+00
* s	-1.84573E-02	± 0.0000E+00	- 0.0000E+00	+ 0.0000E+00
* τ	0.66206	± 0.0000E+00	- 0.0000E+00	+ 0.0000E+00
* σ	5.0000	± 0.0000E+00	- 0.0000E+00	+ 0.0000E+00

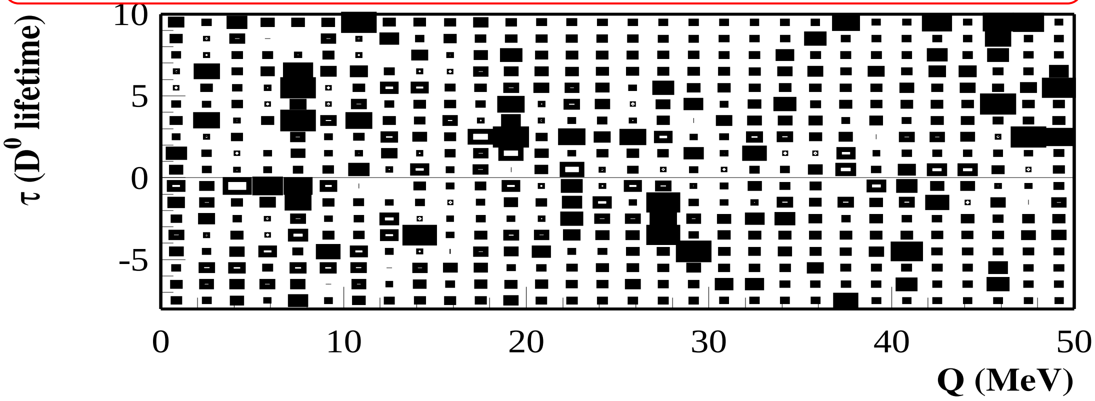

Figure 5.9: Results from the fit to the RS data sample with the functions described in Tables 5.1 and 5.2. Function number corresponds to row in Table 5.2. Black (white) boxes in the 2-dimensional plot represent when the value from the fit function is less (more) than the data value for that bin. Box size is a measure of relative χ^2. The signal function normalizations are equivalent to 638 ± 51 events.

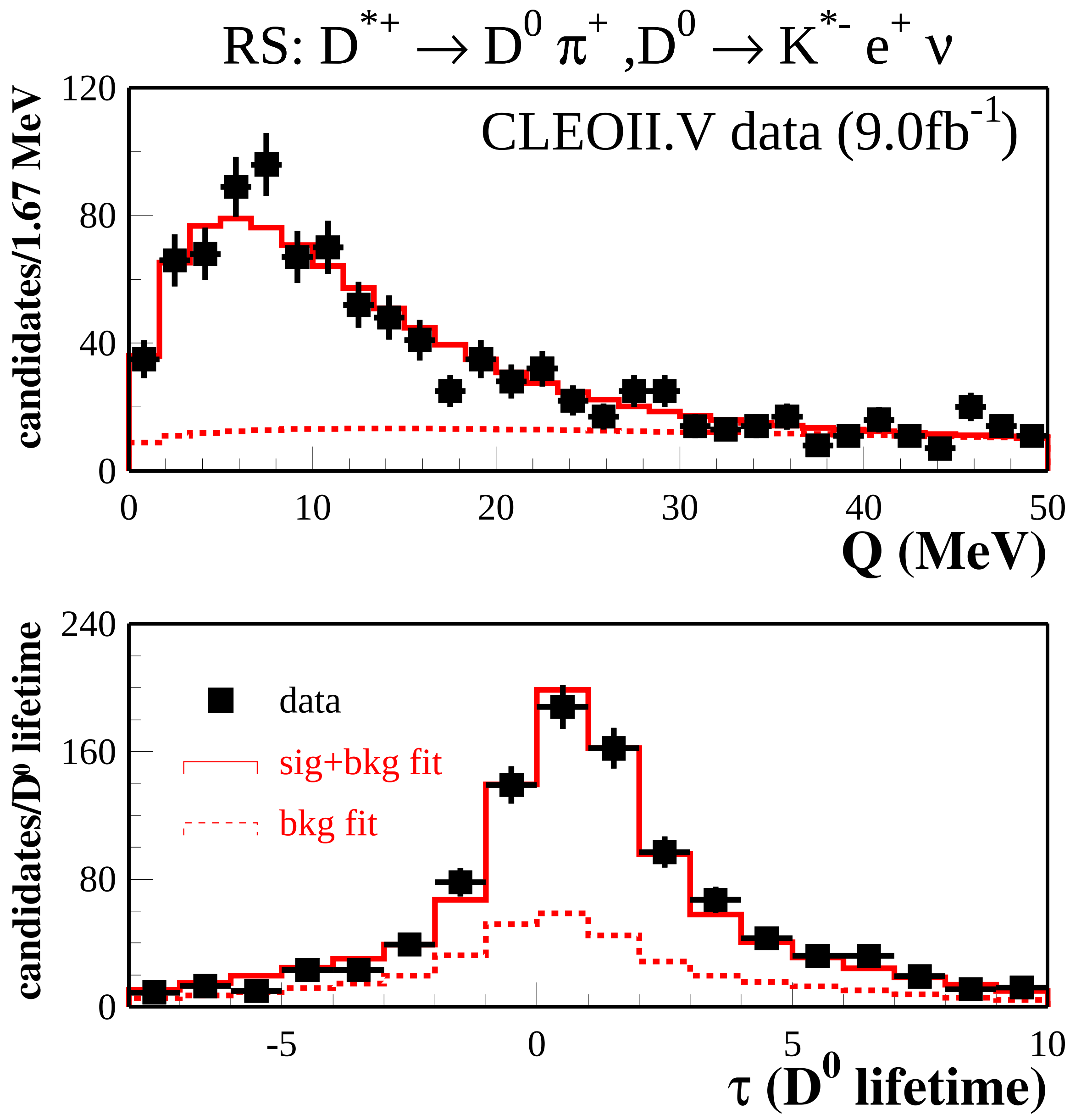

Figure 5.10: Projections of the fit to the RS data sample with the functions described in Tables 5.1 and 5.2. The confidence level of this likelihood fit is 38.3%.

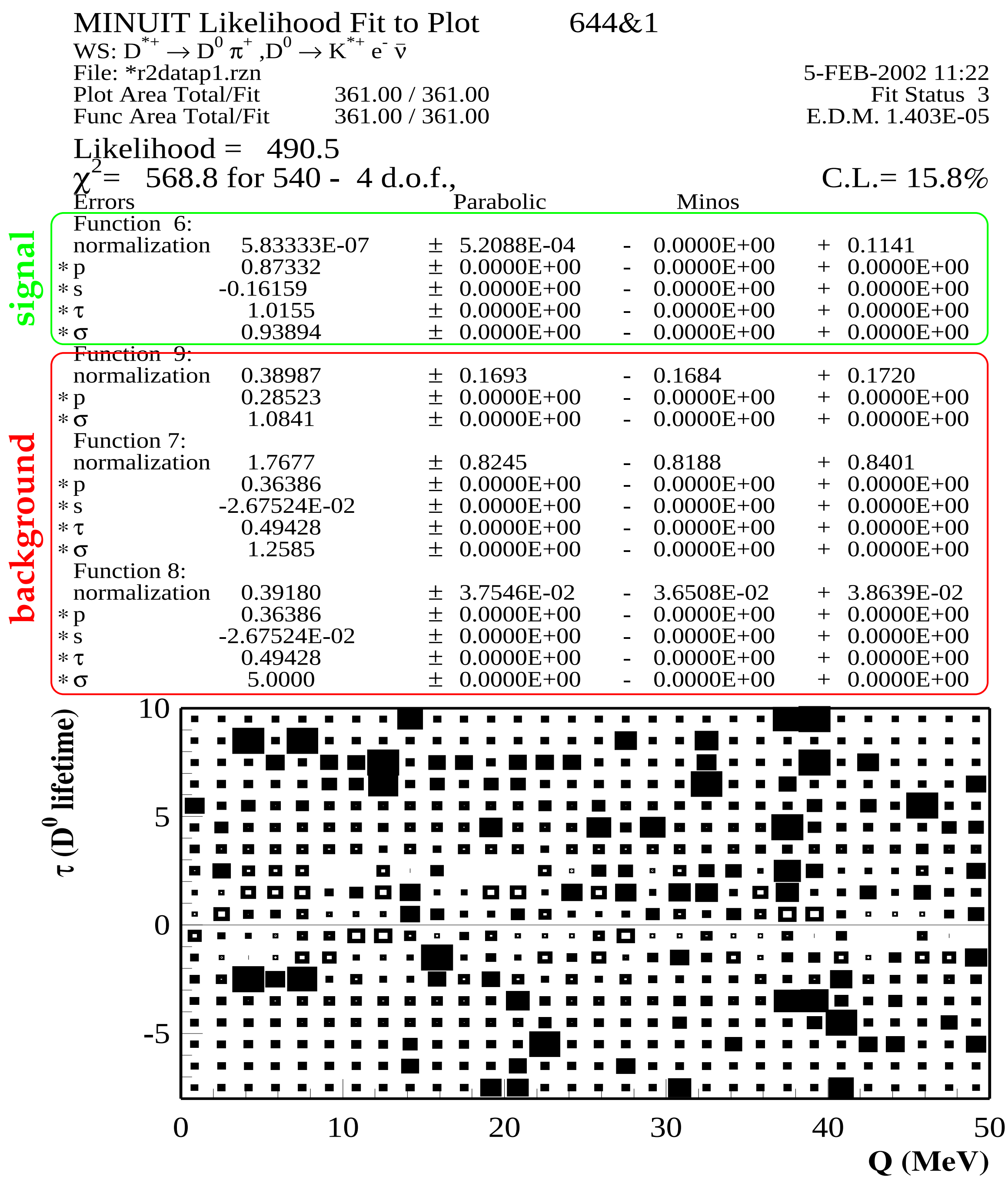

Figure 5.11: Results from the constrained fit to the WS data sample with the functions described in Tables 5.1 and 5.2. Function number corresponds to row in Table 5.2. Black (white) boxes in the 2-dimensional plot represent when the value from the fit function is less (more) than the data value for that bin. Box size is a measure of relative χ^2. The signal function normalization is equivalent to 0.00 ± 1.99 events.

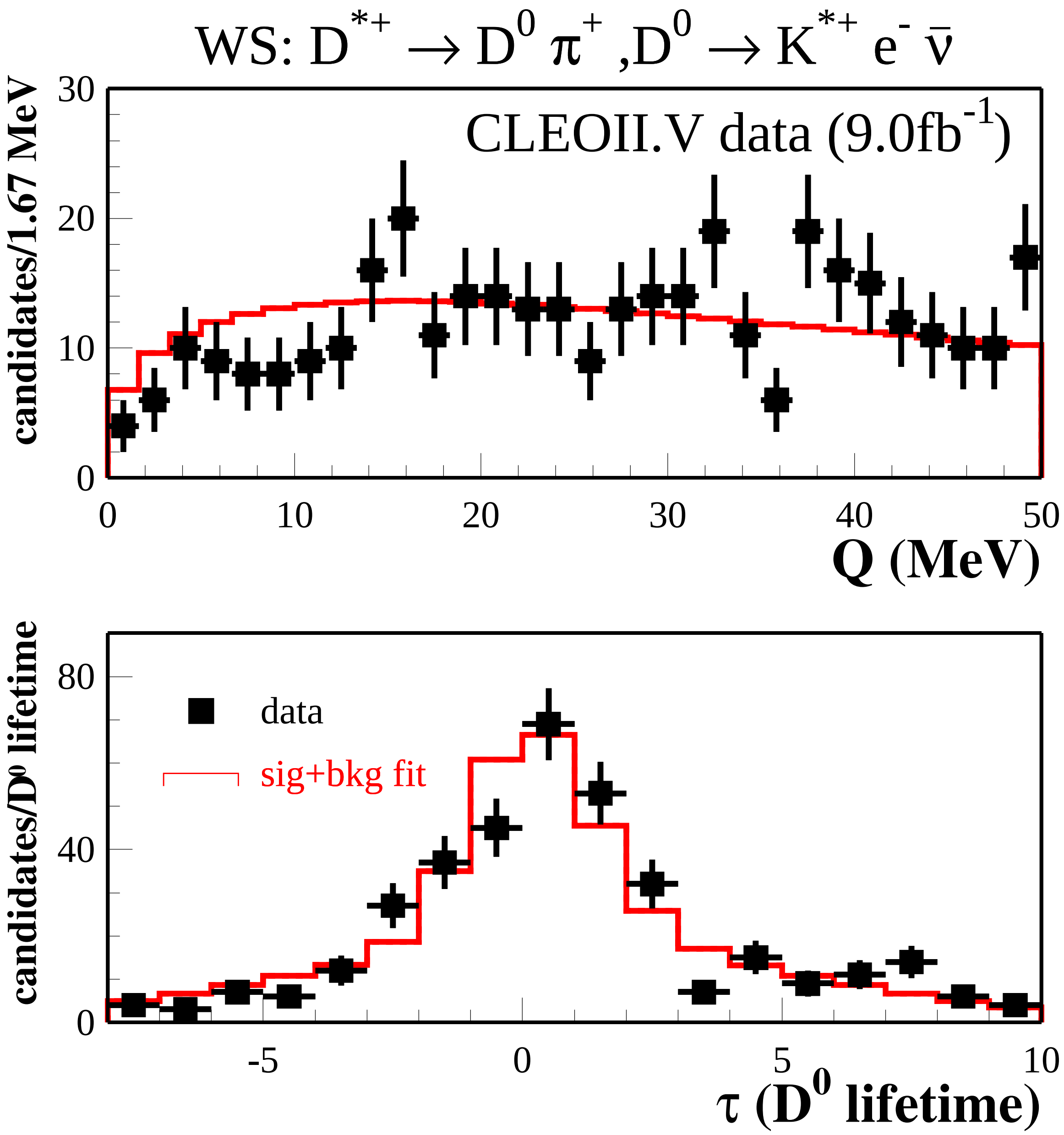

Figure 5.12: Projections of the fit to the WS data sample with the functions described in Tables 5.1 and 5.2. The confidence level of this likelihood fit is 15.8%.

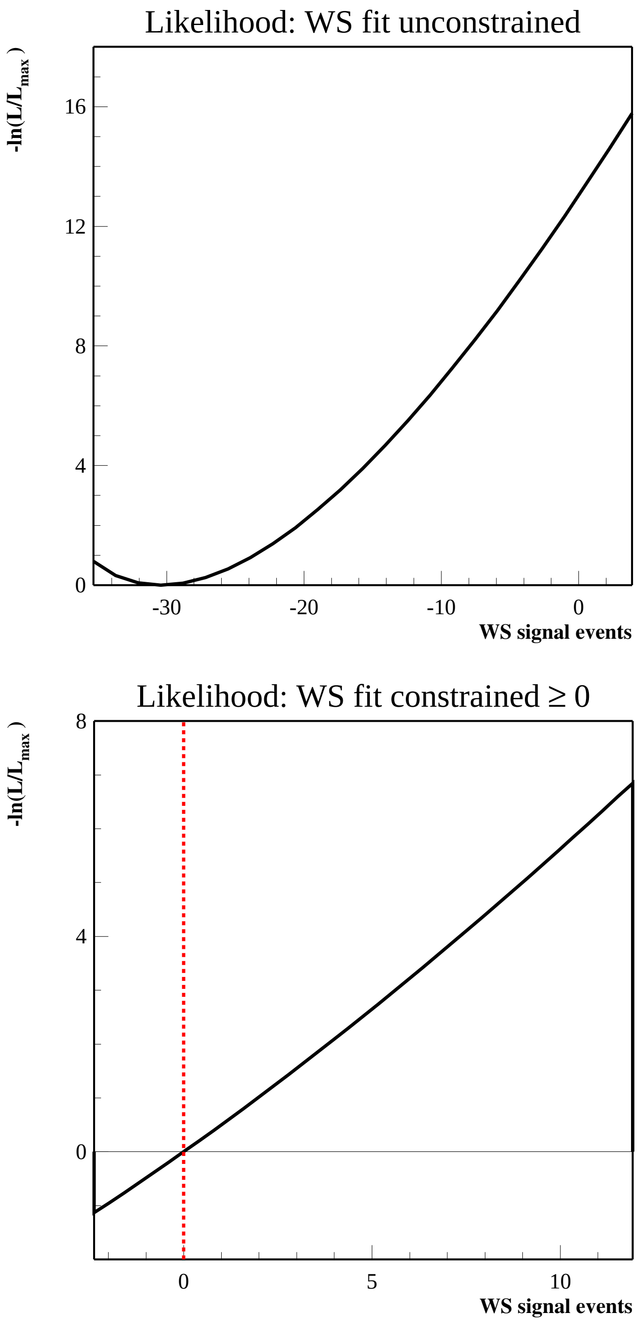

Figure 5.13: Likelihood distributions for the constrained(top) and unconstrained fits to WS data. A one unit change in $-ln(L/L_{max})$ corresponds to a one sigma error[57].

Chapter 6

Systematics

The systematic errors for this analysis come from two main sources; the efficiency with which we reconstruct both RS and WS events and how well we describe the functions we use to quantify the RS and WS signal and background.

Since the fit for WS signal events is bounded on one side, it is not reliable to use changes to the central value of WS candidates to determine the systematic errors. However, it is possible to calculate the systematic error using the statistical and total error from the following formula:

$$\sigma_{syst}^2 = \sigma_{total}^2 - \sigma_{stat}^2 \tag{6.1}$$

It should be noted that this is why only positive $\Delta\sigma_{R_{mix}}$ values are taken to contribute to the systematic errors as seen in Table 6.2.

The efficiencies are checked with a sample of roughly 20,000 RS events and 30,000 WS events. The efficiencies of the two are found to be consistent within monte carlo statistics. The resulting systematic error is listed in Table 6.3.

6.1 Monte carlo statistics

Each of the 2-dimensional functions used to describe the signal and background have at most four parameters that are determined with the monte carlo sample. If we had an infinite amount of monte carlo statistics, the errors ascribed to these parameters would be 0. Needless to say, we do not have the disk space for an infinite amount of statistics, so the variations in the parameters allowed by our finite sample add some systematic error. To determine this effect of finite statistics, each free parameter in the nine functions used to describe the data is varied up and down by 1σ.

In addition, bin sizes were varied to measure the systematics associated with a binned likelihood fit. The systematics from these variations contributed a negligible amount to the total systematic error.

6.2 Parameters describing signal candidates

Using a monte carlo sample to derive the parameters of the functions used to describe the signal and background Q and τ distributions assumes that the monte carlo correctly imitates data. To check this supposition, a fully reconstructible hadronic mode with similar kinematic characteristics to $D^0 \rightarrow K^* e\nu$ events is employed. The decay $D^0 \rightarrow K\pi\pi^0$ is chosen for these similarities and the existence of a large monte carlo signal sample. By first reconstructing the D^0 candidates using a selection

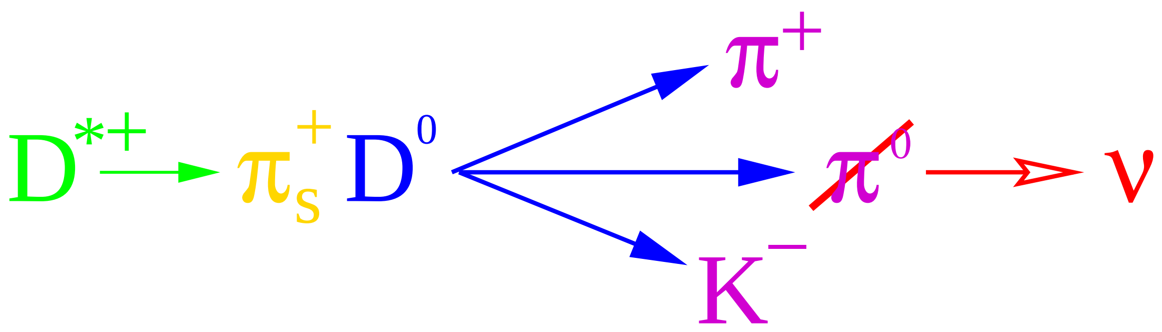

Figure 6.1: To check the D^0 reconstruction method and the systematic errors associated with the functions used in the 2-dimensional binned maximum likelihood fit I utilize the decay channel $D^0 \to K\pi\pi^0$. The D^0 is first reconstructed and selected following the method set forth in the mixing analysis using that decay chain[59]. The π^0 is then tossed-out and the D^0 is reconstructed as if the π^0 were a neutrino in the same manner as described in Section 4.3. The resulting Q and lifetime plots are fit to the same functions described in Sections 5.1 and 5.2. This is repeated for both monte carlo and data samples. Systematic variations are determined by a comparison of the fit parameters derived from each.

method similar to that done in the search for $D^0 - \overline{D}^0$ mixing in that channel[59], cuts can be made on the Q and M_{D^0} distributions to select signal candidates. The π^0 is then excluded and the D^0 is reconstructed as $D^0 \to K\pi\nu$ using the identical technique to reconstruct $D^0 \to K^*e\nu$. This technique is repeated for both a sample of monte carlo and data events to qualitatively and quantitatively check the neutrino reconstruction method and determine the systematic errors on the parameters used to describe signal and background shapes.

A sample of 650,000 $D^0 \to K\pi\pi^0$ monte carlo events is used. These events were generated to be flat across the Dalitz plot. However, in the data there is structure to the Dalitz distribution. To accommodate for this, a simple set of cuts are imposed to select those regions of the Dalitz plot predominantly occupied by signal in the data sample, Figure 6.2.

A background subtraction is performed using $2\sigma_Q$ wide sidebands centered at $4\sigma_Q$ above and below the signal region in the Q distribution, Figure 6.3.

Sidebands are added in equal parts and normalized to the background area under the signal peak. A direct comparison of the resulting distributions from both the monte carlo and data samples can be seen in Figure 6.4.

After the background subtraction, the distributions for Q and τ are fit using identical functions to those describing the Q and τ distributions in the $D^0 \to K^* e\nu$ analysis. The variations of these parameters, subsequently used for the systematic error determination, are calculated in the following way:

$$\sigma_P = \left| \frac{P_{data} - P_{MC}}{P_{MC}} \right| \tag{6.2}$$

where P represents each of the four parameters $(power, slope, \tau, \sigma)$ used in the functions describing signal and background. These variations are then individually applied to the parameters in the fits for RS and WS signal and background to determine the error. A summary of these variances can be found in Table 6.1.

6.3 Parameters describing backgrounds

A similar procedure to that mentioned above is repeated to check the parameters used in a fit to the background. In this case, a sample of 24×10^6 events of generic

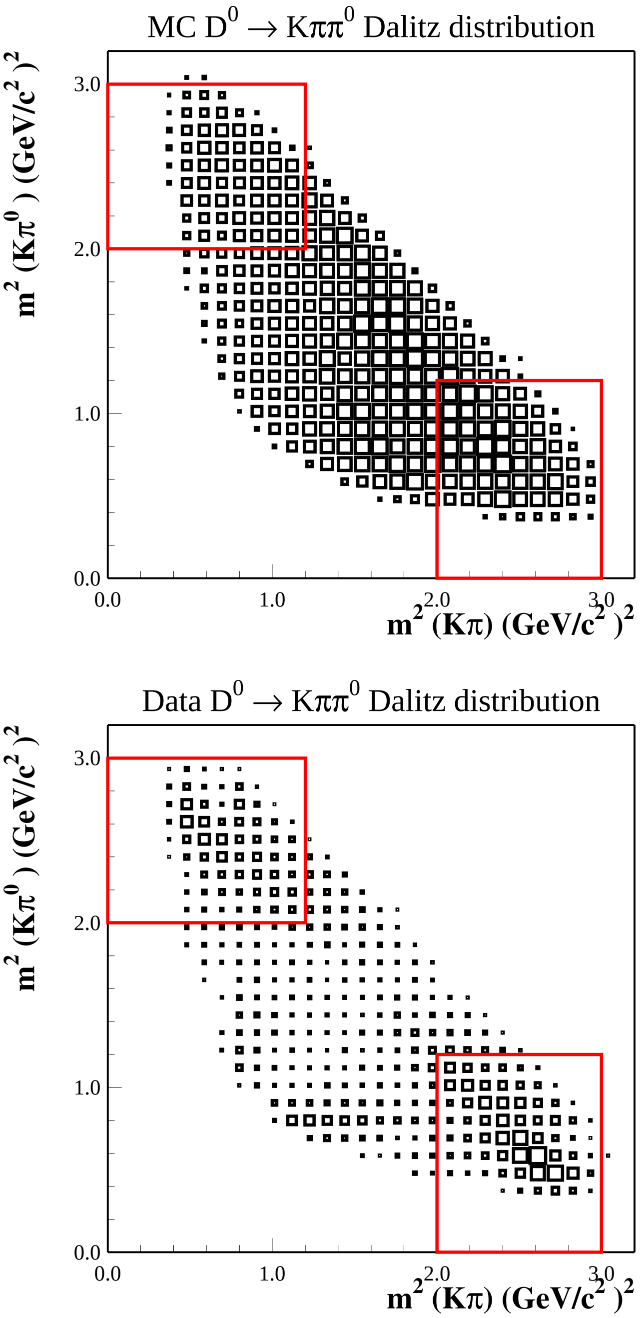

Figure 6.2: Dalitz distributions for monte carlo(top) and data signal candidates after Q and M_{D^0} cuts are made. Boxes indicate cuts to select kinematically similar events.

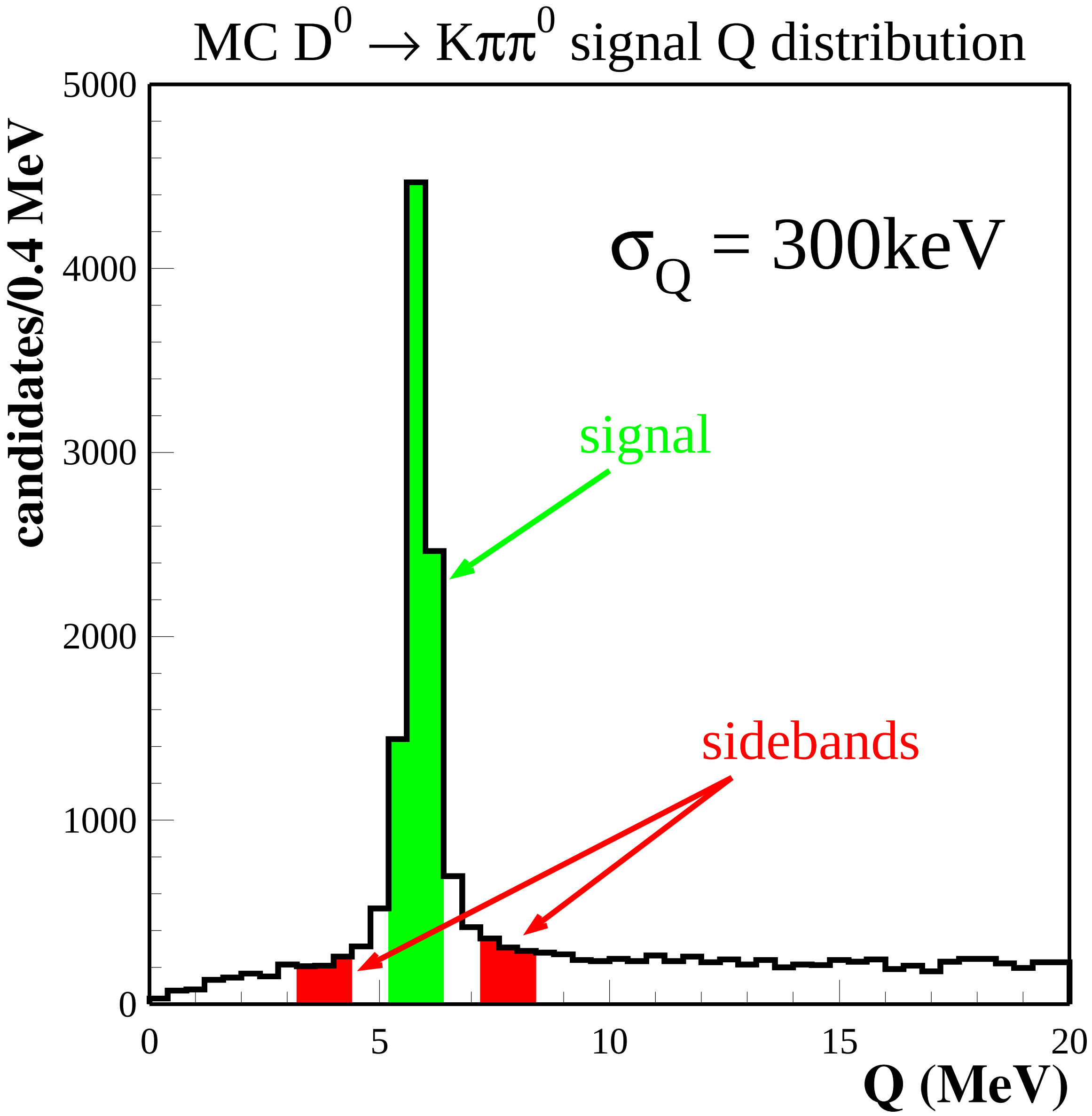

Figure 6.3: Top plot is the Q distribution of $D^0 \to K\pi\pi^0$ reconstructed in the data ($2\sigma_M$ cut in M_{D^0}). Sidebands used for background subtraction are $2\sigma_Q$ bands centered at $4\sigma_Q$ from Q peak.

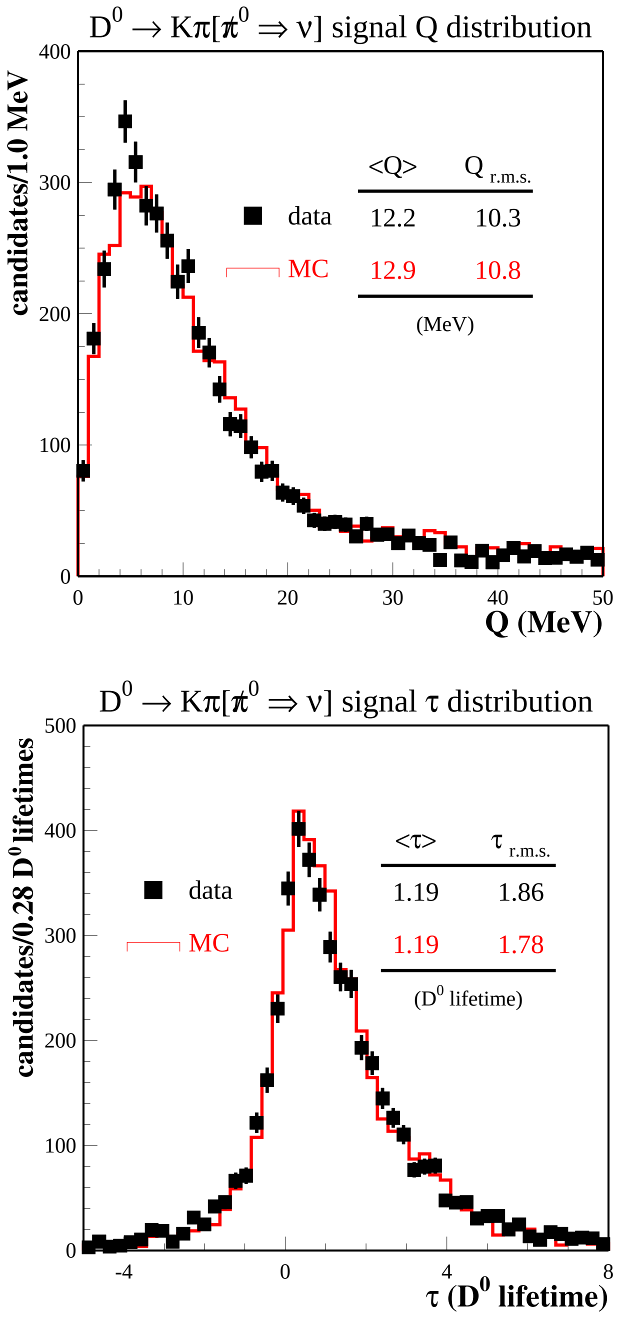

Figure 6.4: Q(top) and τ distribution comparisons between data and monte carlo signal samples after selecting for $D^0 \to K\pi\pi^0$ signal, excluding the π^0 and reconstructing as $D^0 \to K\pi\nu$. This shows excellent agreement between monte carlo and data for the $\vec{\nu}$ reconstruction method.

Table 6.1: Summary of variances in function parameters determined using $D^0 \rightarrow K\pi\pi^0$ decay mode. The variances are determined by the relative change in the function parameter when monte carlo and data samples are fit to the same functions used in the analysis. These variances are then used to modify the function parameters set with 20.0 fb^{-1} of monte carlo data in a fit to signal and background samples for $D^0 \rightarrow K^* e\nu$. This is used as a means of determining the systematic errors associated with using a monte carlo sample to determine shapes expected in data. A summary of these errors is shown in Table 6.2.

	signal				*background*		
	power	slope	τ	σ	τ	$\sigma_{\tau\neq0}$	$\sigma_{\tau=0}$
variance (%)	2	2	2	3	33	3	3

monte carlo is used.

The Dalitz distribution of events in the generic monte carlo has similar structure to that found in the data. Therefore, the box cuts described above are unnecessary to get the correct distribution of kinematically similar events.

Again, candidate events are selected by first reconstructing the decay $D^0 \rightarrow K\pi\pi^0$ then reconstructing the event as if the π^0 was a neutrino. In this instance, however, candidates are taken from M_{D^0} sidebands between 4σ and 16σ above and below the nominal D^0 mass. A direct comparison of the Q and τ distributions can be seen in Figure 6.5 and a summary of the variances in Table 6.1.

The Q and τ distributions of RS and WS backgrounds are identical to within statistical error for the monte carlo sample. Therefore, no distinction is made in either the monte carlo or the data and the results are taken as variances for both RS and WS background parameter errors in the analysis.

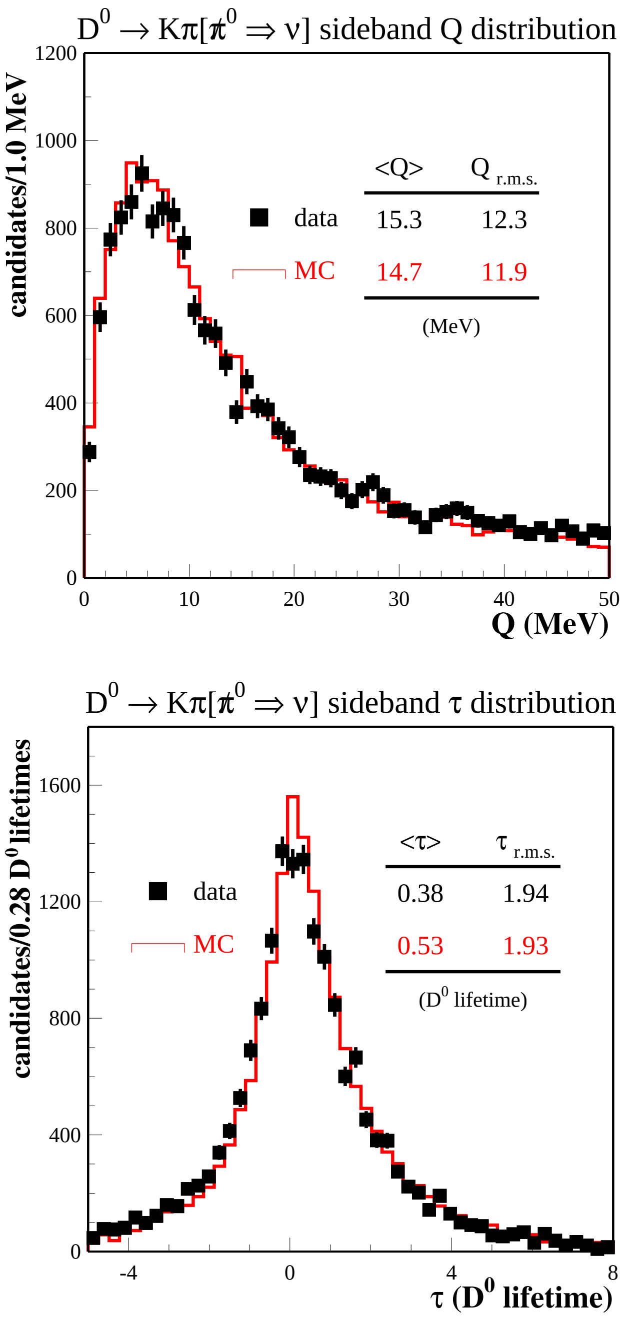

Figure 6.5: Q(top) and τ distribution comparisons between data and monte carlo sideband samples after selecting for $D^0 \to K\pi\pi^0$ signal, excluding the π^0 and reconstructing as $D^0 \to K\pi\nu$.

It can be seen that the variance in the parameters is less than 4% in all cases except the lifetime of background. As a reminder, the background lifetime is described by three functions; a portion with some fraction of τ_{D^0} convolved with a resolution Gaussian $g(\sigma_{\tau\neq 0})$, a portion of zero lifetime $g(\sigma_{\tau=0})$, and a wide Gaussian. The variance of the background is 33%. It may be interesting to attempt to understand why this is so large with respect to the other variances, but for this analysis, it is not the major contributor to the systematic error (that honor going to the MC statistics error for WS background). Also, although the variance of the resolution on the zero lifetime piece is a significantly smaller 3%, the error attributed to that parameter is considerable. If the WS background lifetime variance is left out of the systematic error calculation, the overall error is reduced by only 7%.

6.4 Background Q distributions

Although the parameters used to describe the Q distributions appear to vary little between monte carlo and data as described above, the background Q distributions for the mode $D^0 \to K\pi\pi^0$ are markedly different than those for $D^0 \to K^*e\nu$. This can be seen by comparing the Q distributions in Figure 6.5 with the background Q distribution in Figure 5.6 or the Q distribution in Figure 5.12. Therefore, an independent method for determining the limits on variations in the background Q distributions is considered. A simple flat function is substituted for the threshold

Table 6.2: Details of systemtatic errors determined using $D^0 \rightarrow K\pi\pi^0$ decay mode. The table is divided into three sections; one for each set of parameters describing functions used to fit for (a) signal, (b) RS backgrounds, and (c) WS backgrounds. The central value and the new values $\pm$(central value $\times$ variance) are included along with the resulting changes to number of RS signal events and the error on the number of WS signal events. Finally, the change to R_{mix} and the resulting systematic error are shown. For reference, the number of RS and WS events determined in the analysis are $RS \pm \sigma_{RS} = 638 \pm 51$ and $WS + \sigma_{WS} = 0.00 + 1.99$.

parameter (central value)	*new value*	ΔRS *(events)*	$\Delta\sigma_{WS}$ *(events)*	$\Delta\sigma_{R_{mix}}$ *(%)*	$\sigma_{\mathbf{syst}}$ **(%)**
power	0.8559	+20.5	+0.06	−0.0005	n/a
(0.8733)	0.8908	−20.0	−0.06	+0.0006	**0.0196**
slope	−0.1584	−14.1	−0.03	+0.0015	**0.0303**
(−0.1616)	−0.1648	+14.2	+0.04	−0.0013	n/a
lifetime	0.9952	−0.48	−0.03	−0.0045	n/a
(1.0155)	1.0358	+0.53	+0.03	−0.0050	**0.0559**
σ	0.9108	−0.74	−0.01	−0.0009	n/a
(0.9389)	0.9671	+0.72	+0.01	+0.0009	**0.0243**
subtotal for signal shape parameters					**0.0708**
lifetime	0.4436	+3.07	0.00	−0.0015	n/a
(0.6621)	0.8805	−0.59	0.00	+0.0003	**0.0133**
$\sigma_{\tau\neq 0}$	1.1362	+1.80	0.00	−0.0009	n/a
(1.1713)	1.2064	−1.56	0.00	+0.0008	**0.0218**
$\sigma_{\tau=0}$	1.1546	−1.19	0.00	+0.0006	**0.0190**
(1.1903)	1.2260	+1.24	0.00	−0.0006	n/a
subtotal for RS background shape parameters					**0.0318**
lifetime	0.3312	0.00	+0.19	+0.0300	**0.1399**
(0.4943)	0.6574	0.00	−0.10	−0.0157	n/a
$\sigma_{\tau\neq 0}$	1.2207	0.00	+0.01	+0.0012	**0.0276**
(1.2585)	1.2962	0.00	−0.00	−0.0006	n/a
$\sigma_{\tau=0}$	1.0516	0.00	−0.05	−0.0080	n/a
(1.0841)	1.1166	0.00	+0.05	+0.0086	**0.0736**
subtotal for WS background shape parameters					**0.1605**
				GRAND TOTAL	**0.1782**

Table 6.3: Summary of systematic error analyses.

variation	*as applied to*	$\Delta R_{mix}(\%)$
MC statistics	WS bkg	± 0.19
	signal	± 0.10
	RS bkg	± 0.07
	subtotal	$\pm\mathbf{0.23}$
shape variations	WS bkg lifetime	± 0.16
	signal lifetime	± 0.06
	signal Q	± 0.04
	RS bkg lifetime	± 0.03
	subtotal	$\pm\mathbf{0.18}$
Q shape to flat	RS bkg	± 0.07
	WS bkg	± 0.06
	subtotal	$\pm\mathbf{0.09}$
efficiency	WS/RS	$\pm\mathbf{0.00}$
	TOTAL	$\pm\mathbf{0.31}$

functions used to described the RS and WS backgrounds. This is perhaps the most extreme change that can be made in these shapes but is also a good systematic check because it tends to overestimate the number of WS signal and underestimate the number of RS background. The fits are shown in Figures 6.6, 6.7, 6.8, and 6.9. The resulting systematics from these approximations are contained in Table 6.3.

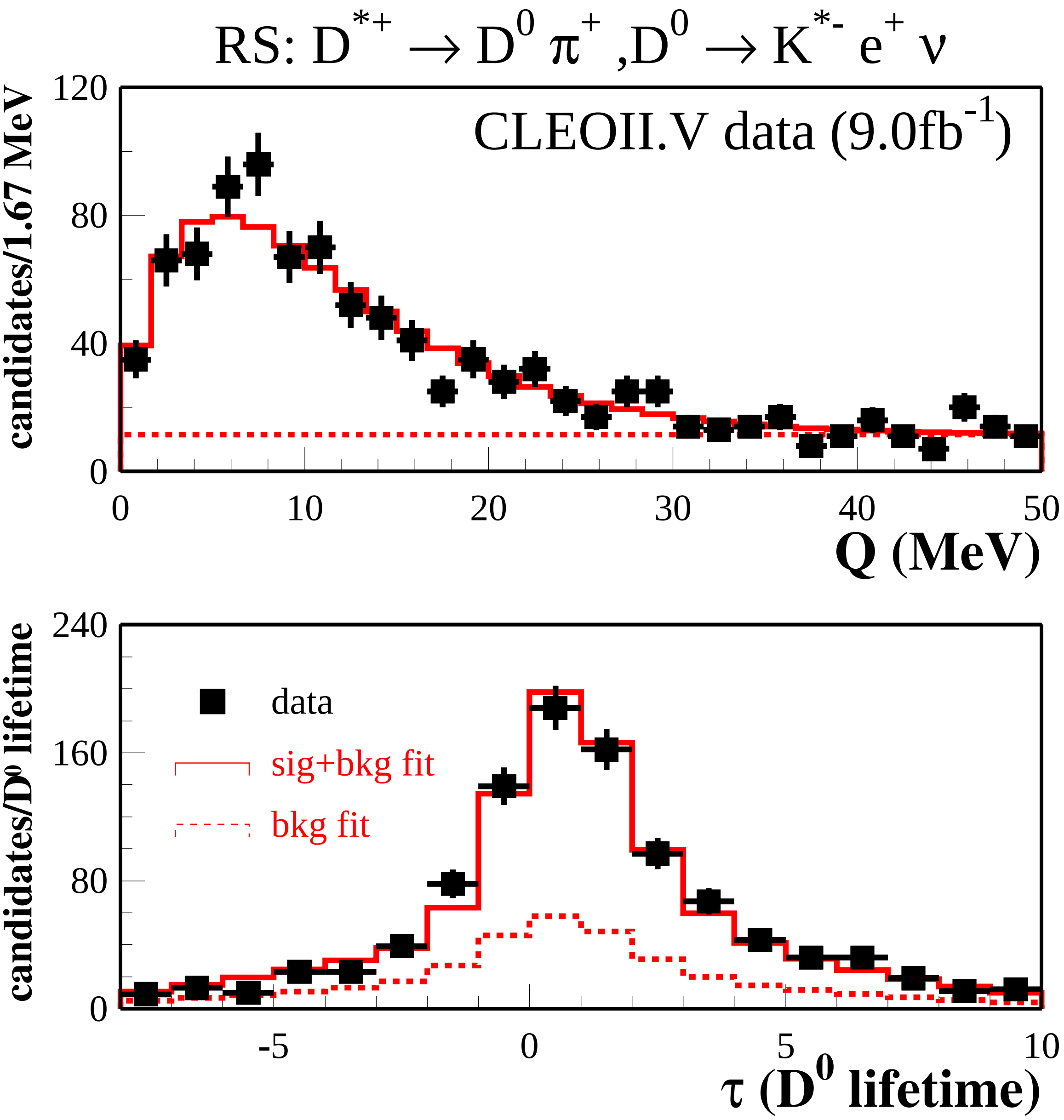

Figure 6.6: Projections from the RS fit to background using a flat function to describe the Q dimension. This is done as a means of approximating the variations of the parameters used to describe the RS backgrounds as a check of the systematics. A comparison of the RS flat function fit result with that of the threshold function used to determine the central value is shown in Figure 6.7.

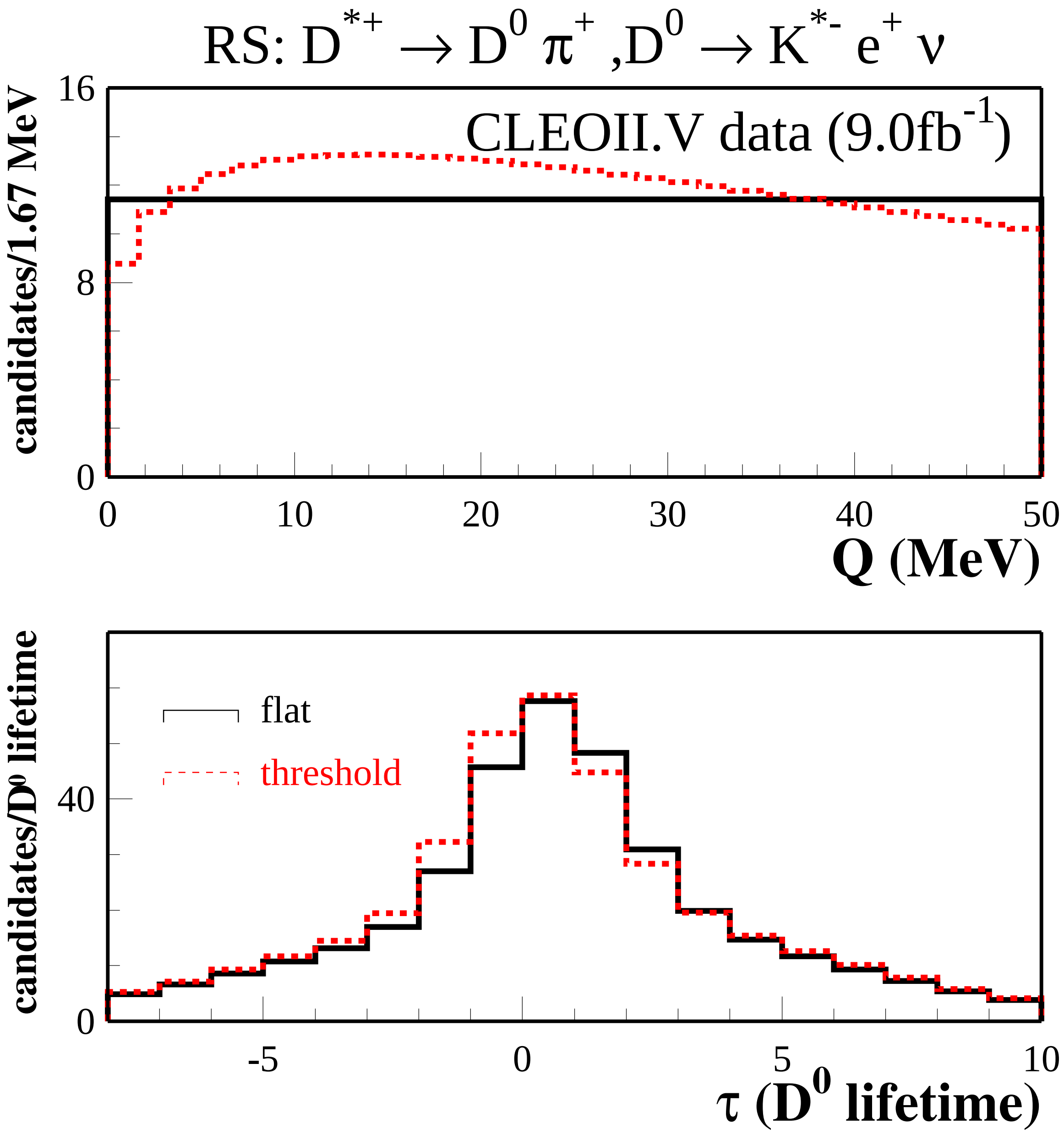

Figure 6.7: Comparison of Q and lifetime projections for the RS flat function fit to backgrounds with that of the threshold function used to determine the central value. Fits are done to check the systematic variations related to the functions chosen to represent backgrounds. Projections from the actual fits to RS data are shown in Figure 6.6.

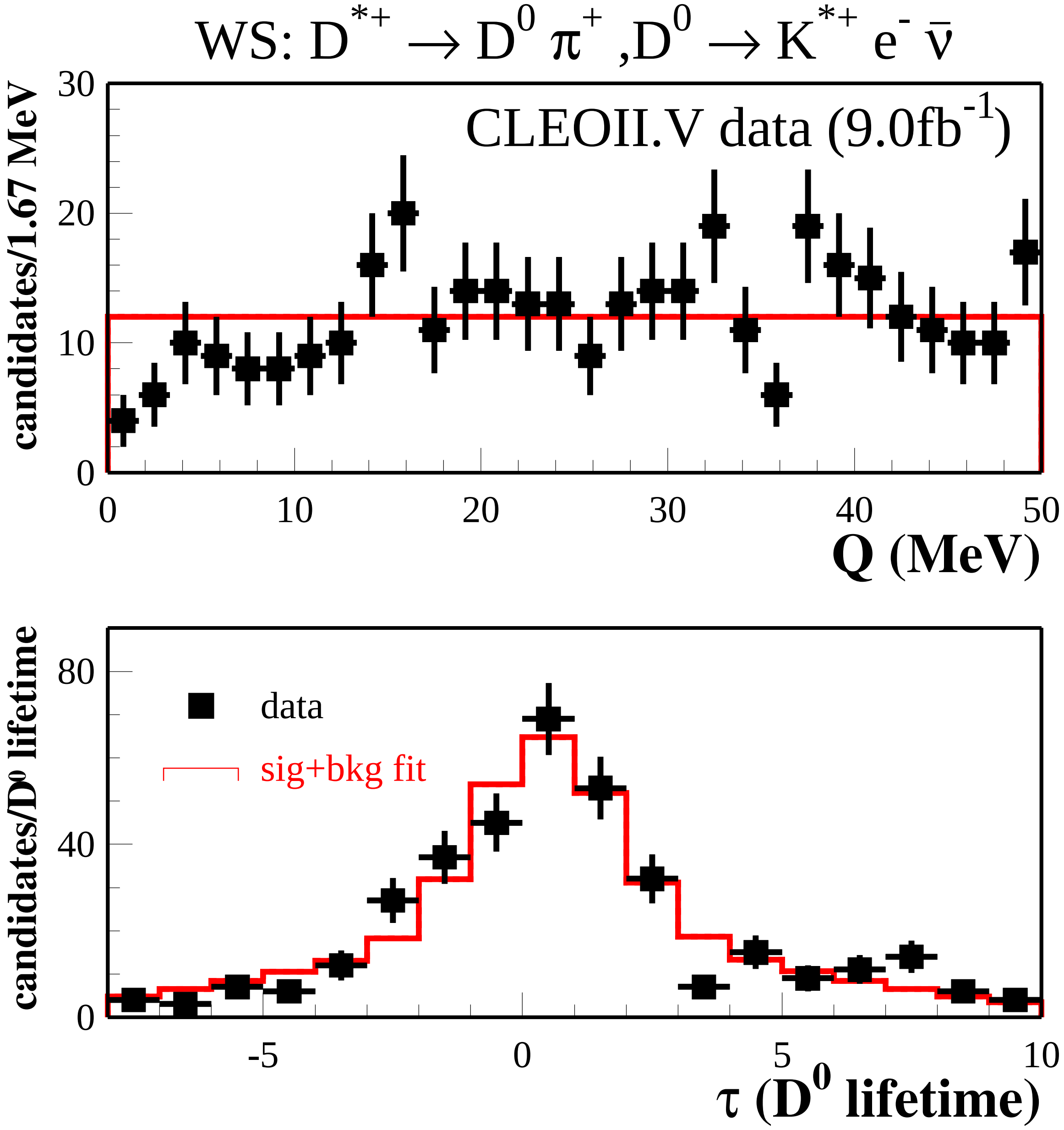

Figure 6.8: Projections from the WS fit to background using a flat function to describe the Q dimension. Performed as a means of approximating the variations of the parameters used to describe the WS backgrounds for a systematics check. A comparison of the WS flat function fit result with that of the threshold function used to determine the central value is shown in Figure 6.9.

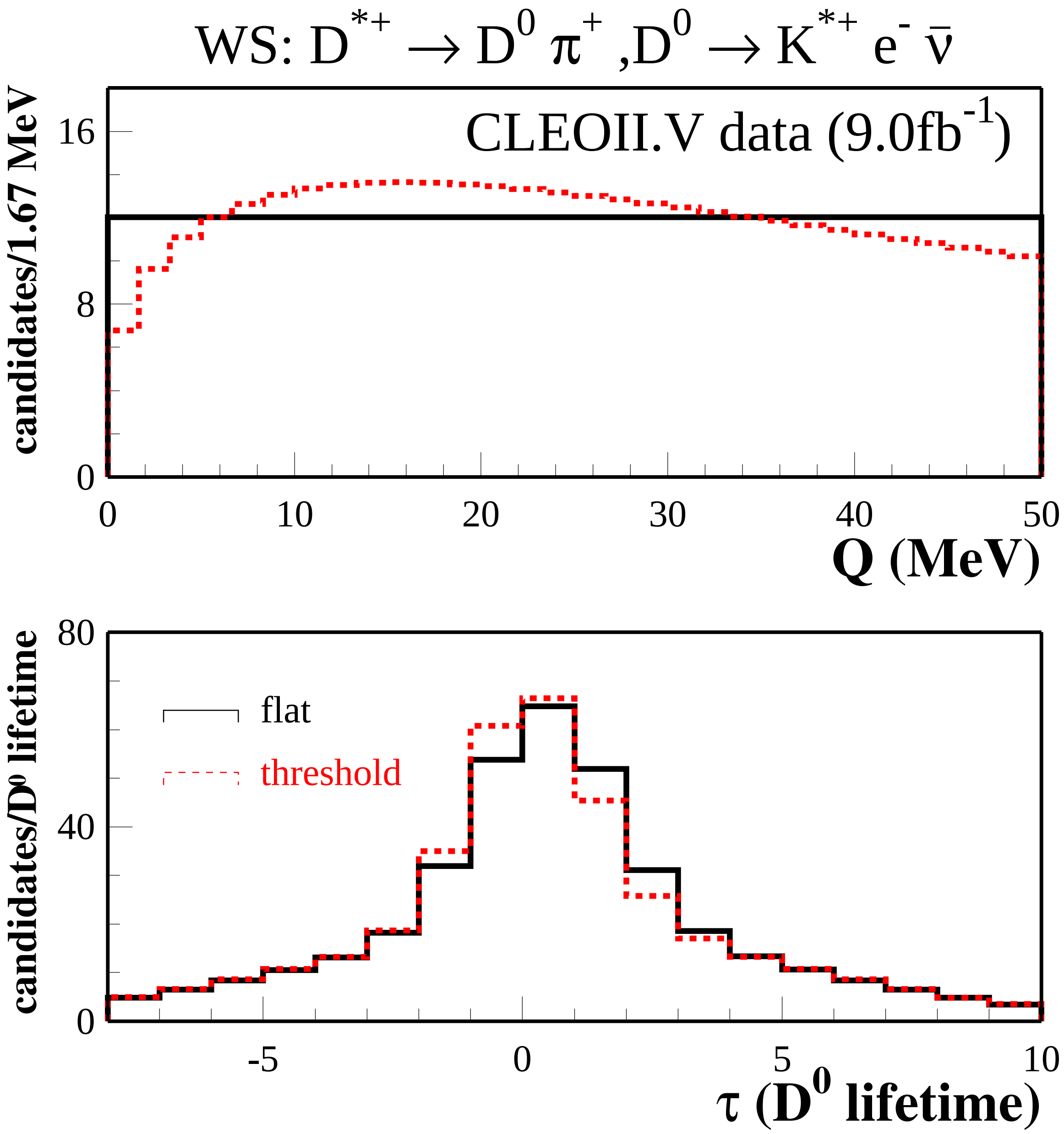

Figure 6.9: Comparison of Q and lifetime projections for the WS flat function fit to backgrounds with that of the threshold function used to determine the central value. Fits are done to check the systematic variations related to the functions chosen to represent backgrounds. Projections from the actual fits to WS data are shown in Figure 6.8.

Chapter 7

Conclusion

Using the more conservative result obtained with a constrained fit on the number of WS events, our limit on

$$R_{mix} = 0.00 + 0.31 \pm 0.31\%. \tag{7.1}$$

This corresponds to a 95% C.L. of $< 0.86\%$. The existing limit on R_{mix} using a semileptonic channel was set by E791 with the decay $D^0 \to Kl\nu$[63]. That limit is a 95% C.L. of $R_{mix} < 0.67\%$. A comparison of these two results along with limits on x and y from hadronic mode searches at CLEO and other experiments is shown graphically in Figure 7.1. Recall from Section 2.3 that

$$R_{mix} = \frac{1}{2}(x^2 + y^2). \tag{7.2}$$

Although the limit set in this analysis falls outside the existing limit, this is the first time that the channel $D^0 \to K^* e\nu$ has been used to set a limit on $D^0 - \overline{D}^0$ mixing. In addition, a search for $D^0 - \overline{D}^0$ mixing via the channel $D^0 \to Kl\nu$ is in progress at CLEO as of this writing. Combining this result with the result from the

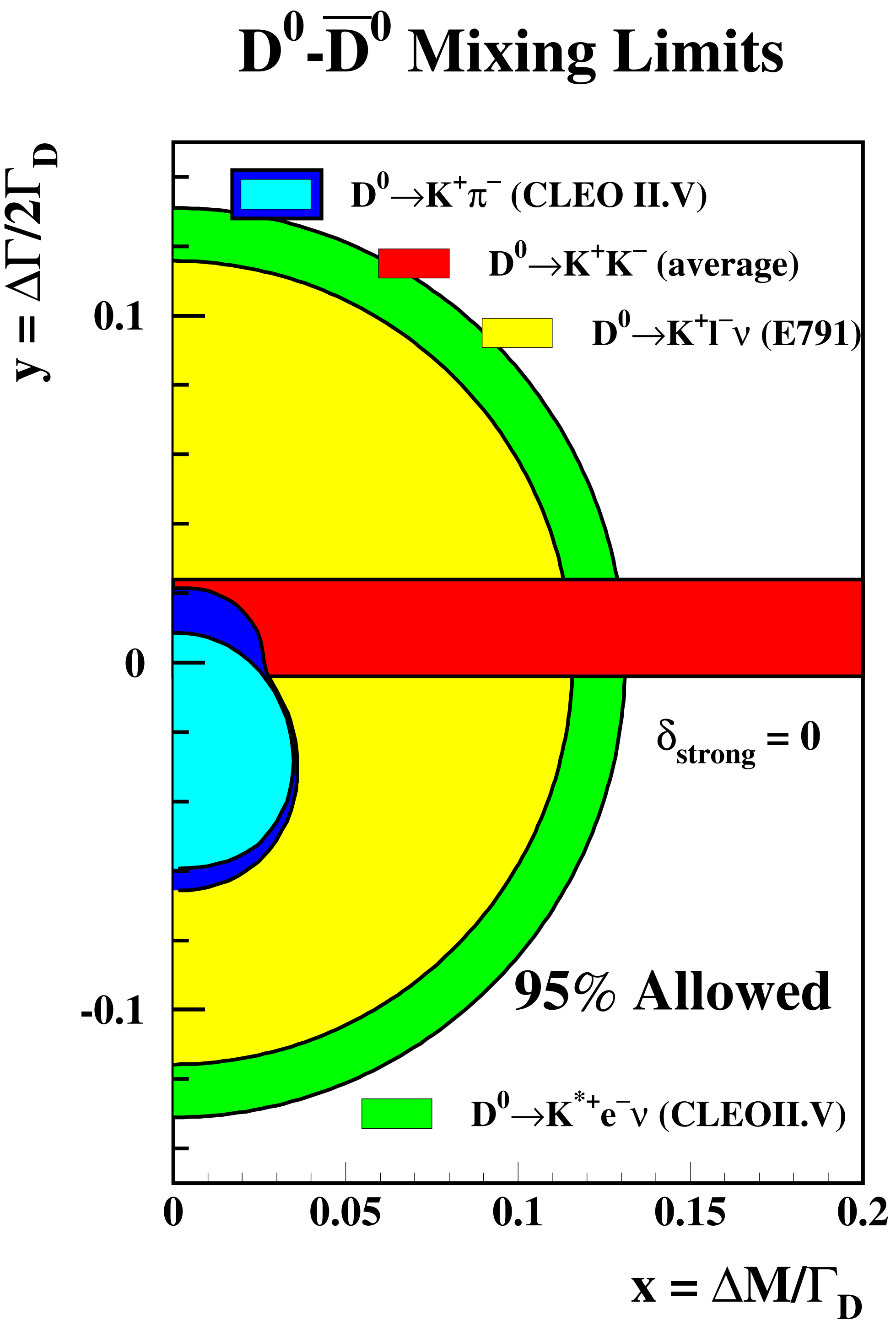

Figure 7.1: Summary of mixing limits. The large semicircles come from mixing limits set with searches in the semileptonic modes.

$D^0 \to Kl\nu$ channel should decrease the CLEO limit on R_{mix} since measurements of different semileptonic decay channels can be combined by averaging, leading to an improved measurement or limit on R_{mix} since wrong sign decays only arise through mixing in these decays[64].

It needs to be mentioned that the E791 95% upper limit on $R_{mix} < 0.67\%$ quoted above is based on a recalculation I made from the published value of $R_{mix} = 0.11^{+0.30}_{-0.27}$. The method used to determine the 95% upper limit in this analysis is different from that used in calculating the published E791 95% upper limit. The different methods are illustrated in Figure 7.2. Essentially, in both works, a Gaussian distribution of R_{mix} values of width $\pm\sigma$ is assumed. For this work, those values that fall below $R_{mix} = 0$, and are therefore unphysical, are excluded from the calculation of a 95% upper limit. The published 95% upper limit from E791 includes all values for R_{mix}. This recalculation is intended only to treat the results in the same manner.

One obvious improvement in the determination of the parameters x and y becomes evident upon examination of Figure 7.1. If an improved limit or, preferably, a non-zero central value measurement of R_{mix} with reasonable errors is made in a search for $D^0-\overline{D}^0$ mixing in a semileptonic channel, a semicircular band centered on zero would intersect the y band from the $D^0 \to K^+K^-$ (CP eigenstate analyses) world average allowing for limits to be set for both values of x and y independent of a measure of the strong phase (δ_{strong}).

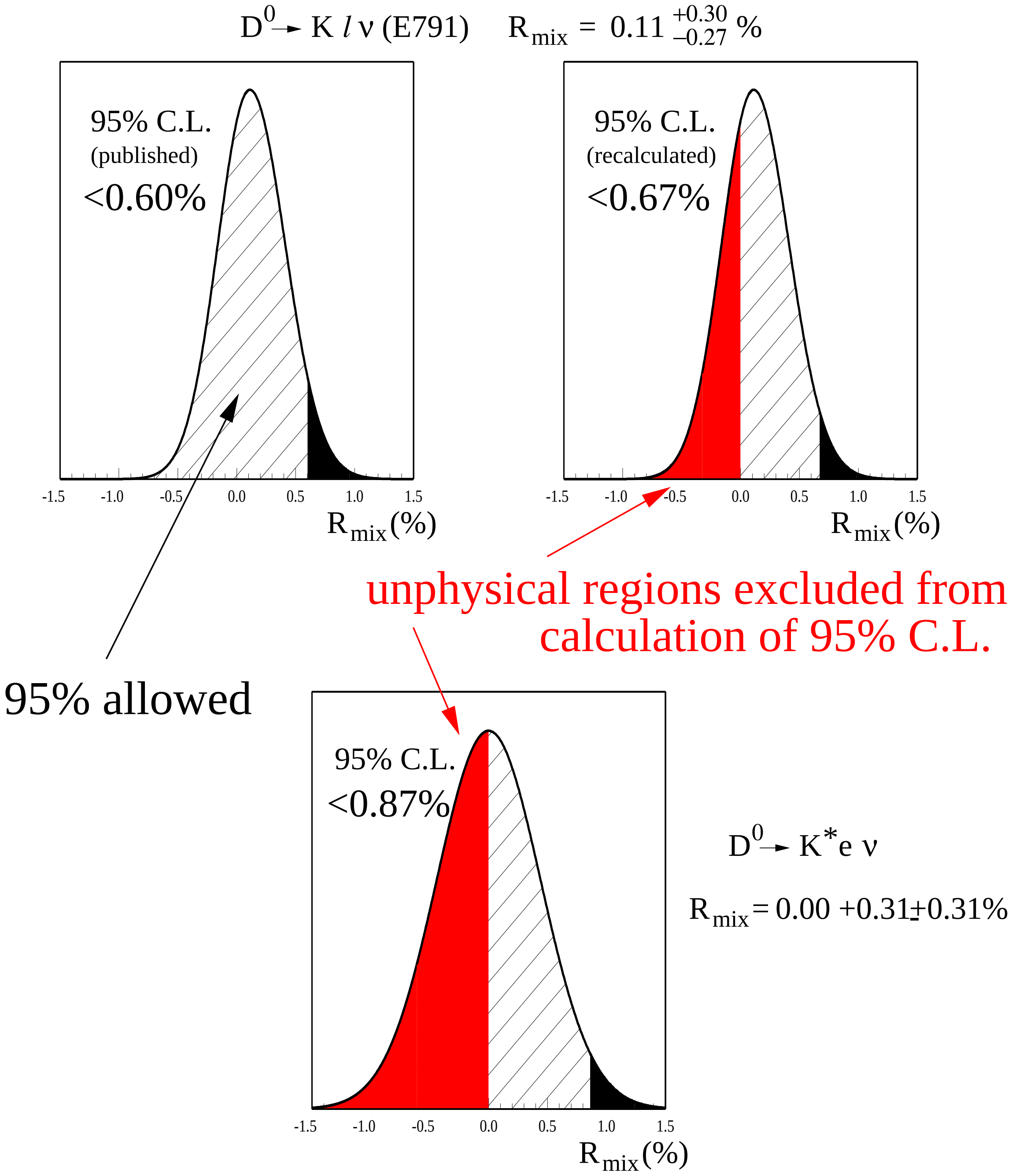

Figure 7.2: In both this work and that done at E791, a Gaussian distribution of R_{mix} values of width $\pm\sigma$ is assumed. For this work however, those values that fall below $R_{mix} = 0$, and are therefore unphysical, are excluded from the the calculation of a 95% upper limit The published 95% upper limit from E791 includes all values for R_{mix}. Therefore, I performed a recalculation of the 95% upper limit from the published E791 result of R_{mix} so the both results may be directly compared.

Appendix A

Derivation of quadratic ambiguity from mass constraint

To find the total momentum of the D^0 after finding its direction, we constrain the 4-vector to the mass of the D^0

$$P^2 = E^2 - \vec{P}^2 = M_{D^0}^2 \tag{A.1}$$

This is equivalent to

$$M_{D^0}^2 = (P_{\tilde{D}^0} + P_\nu)^2 = P_{\tilde{D}^0}^2 + P_\nu^2 + 2P_{\tilde{D}^0}P_\nu \tag{A.2}$$

Assuming a massless neutrino

$$P_\nu^2 = M_\nu^2 = 0 \qquad\qquad E_\nu = |\vec{P}_\nu| \tag{A.3}$$

and substituting

$$P_{\tilde{D}^0}^2 = M_{\tilde{D}^0}^2 \qquad\qquad P_{\tilde{D}^0}P_\nu = E_{\tilde{D}^0}E_\nu - \vec{P}_{\tilde{D}^0} \cdot \vec{P}_\nu \tag{A.4}$$

equation 4.7 becomes

$$M_{D^0}^2 = M_{\tilde{D}^0}^2 + 2(E_{\tilde{D}^0}E_\nu - \vec{P}_{\tilde{D}^0} \cdot \vec{P}_\nu). \tag{A.5}$$

Breaking the momentum vectors into transverse and longitudinal components with respect to the D^0 direction and rearranging

$$\frac{1}{2}(M_{D^0}^2 - M_{\tilde{D}^0}^2) = E_{\tilde{D}^0}|\vec{P}_\nu| - (p_{\tilde{D}^0}^t)(p_\nu^t) - (p_{\tilde{D}^0}^l)(p_\nu^l) \tag{A.6}$$

can be rewritten as

$$K + (p_{\tilde{D}^0}^l)(p_\nu^l) = E_{\tilde{D}^0}|\vec{P}_\nu| \tag{A.7}$$

with

$$K = \frac{1}{2}(M_{D^0}^2 - M_{\tilde{D}^0}^2) + (p_{\tilde{D}^0}^t)(p_\nu^t) \tag{A.8}$$

K is comprised of all known quantities. (p_ν^t can be determined using the opening angle of $\tilde{D}^0$ and D_{calc}^0.) Squaring both sides

$$[K + (p_{\tilde{D}^0}^l)(p_\nu^l)]^2 = E_{\tilde{D}^0}^2 \vec{P}_\nu^2 = E_{\tilde{D}^0}^2[(p_\nu^t)^2 + (p_\nu^l)^2] \tag{A.9}$$

and expanding

$$K^2 + (p_{\tilde{D}^0}^l)^2(p_\nu^l)^2 + 2K(p_{\tilde{D}^0}^l)(p_\nu^l) = E_{\tilde{D}^0}^2(p_\nu^t)^2 + E_{\tilde{D}^0}^2(p_\nu^l)^2 \tag{A.10}$$

This can now be written as a quadratic in terms of the only unknown quantity, p_ν^l

$$(p_\nu^l)^2[(p_{\tilde{D}^0}^l)^2 - E_{\tilde{D}^0}^2] + (p_\nu^l)[2K(p_{\tilde{D}^0}^l) + [K^2 - E_{\tilde{D}^0}^2(p_\nu^t)^2] = 0 \tag{A.11}$$

Appendix B

Comparison of eID to CEID

As a means of measuring the efficacy of my electron selection criteria(eID), I will compare it to one of the existing electron identification packages at CLEO. The most commonly used is the Cornell Electron Identification(CEID) which boils the process down to the assignment of one variable, R2ELEC[65]. R2ELEC is a measure of the probability that a particular track is an electron based on a likelihood derived from comparing seven track and shower characteristics of the candidate to distributions of those same variables for known electrons. These variables are SGELDI and E/P (defined on page 53), the time of flight, three CC shower description variables and the distance the track is from the shower matched to it. The user can choose a minimum R2ELEC value depending on the desired efficiency. Although, the greater the efficiency, the lower the overall yield (see Figure B.1 and B.2).

A large part of my time as a graduate student on the CLEO experiment was spent updating and running the existing CLEOII CEID software on the entire CLEOII.V dataset. For the CLEOII.V dataset, CEID was designed to cover only tracks of $p >$

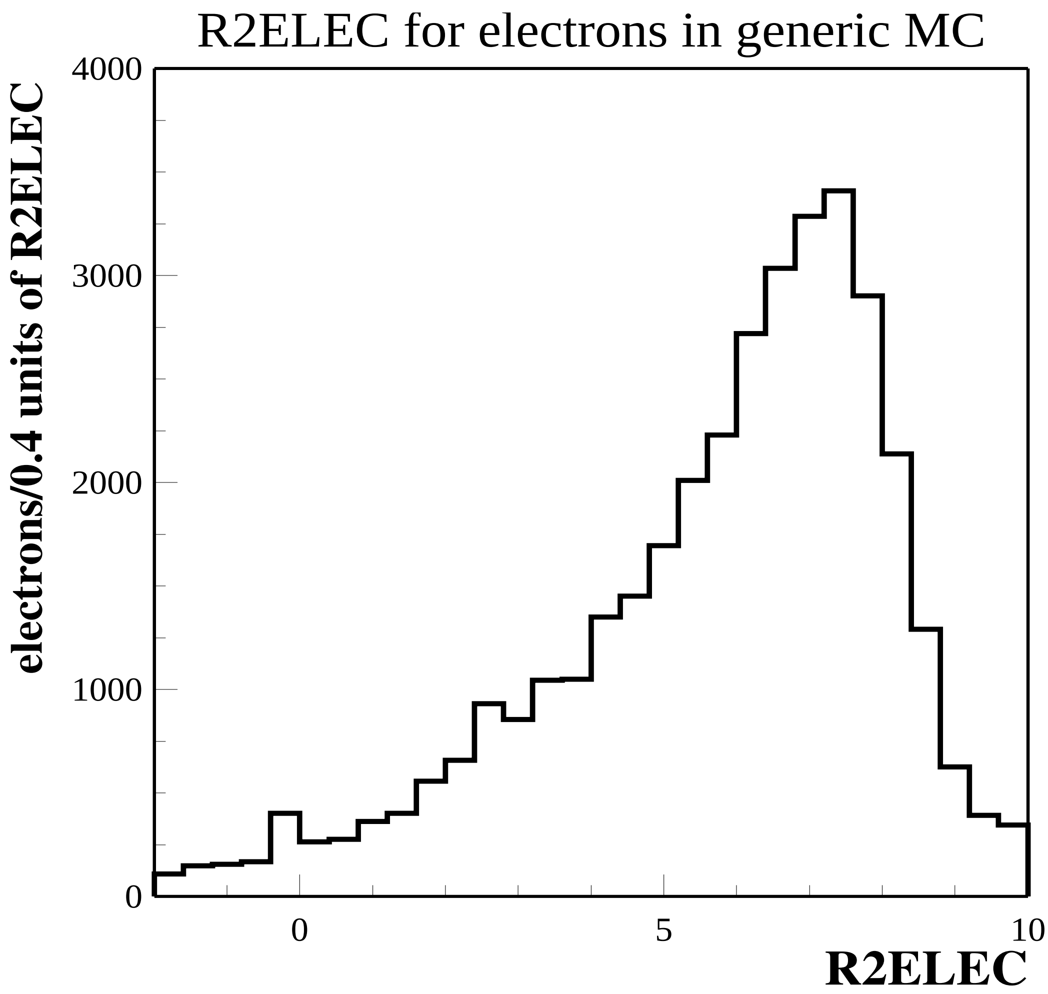

Figure B.1: Example of the R2ELEC distribution for use in the Cornell Electron Identification package. The higher the value of R2ELEC selected, the more likely the track is an electron. As the R2ELEC value chosen increases though, the overall yield of electrons selected drops. This plot is intended as a reference for the comparisons of yield, efficiency and fake rate between CEID and eID shown in Figures B.2 and B.3 on pages 131 and 132, respectively.

400 MeV because electron identification efficiencies below that momentum dropped precipitously. However, a significant fraction (30%) of the electrons from the $D^0 \to K^* e\nu$ decay lie below this lower limit so it was desirable to come up with an alternative method of selecting electrons. I will refer to my alternative method described above as eID.

How does eID compare with CEID? In an attempt to quantify this, I consider both the efficiency(η)

$$\eta = \frac{\text{\# of electrons passing eID}}{\text{Total \# of electrons in sample}} \tag{B.1}$$

and the fake rate(FR)

$$FR = \frac{\text{\# of non}-\text{electrons passing eID}}{\text{Total \# of particles passing eID}} \tag{B.2}$$

I use a sample of 47,000 signal MC events to determine the efficiencies and overall yields and a sample of 25 million generic MC events to determine the fake rates. In Figures B.2 and B.3 it's clear that both η, yield, and FR are dependent on the choice of R2ELEC, whereas eID is not. Along with a comparison of CEID and eID in Figures B.2 and B.3, I also include CEID plus eID for those electrons that fall below the minimum momentum for CEID, $p < 400$ MeV, as a comparison of eID and a hybrid of the two.

The efficiencies shown in Figure B.2 include the factor of 64% for those electrons that pass the $p > 330$ MeV and track quality cuts (i.e., two hits in $r - \phi$ and z silicon layers). Since R_{mix} is expected to be small[21], background suppression is

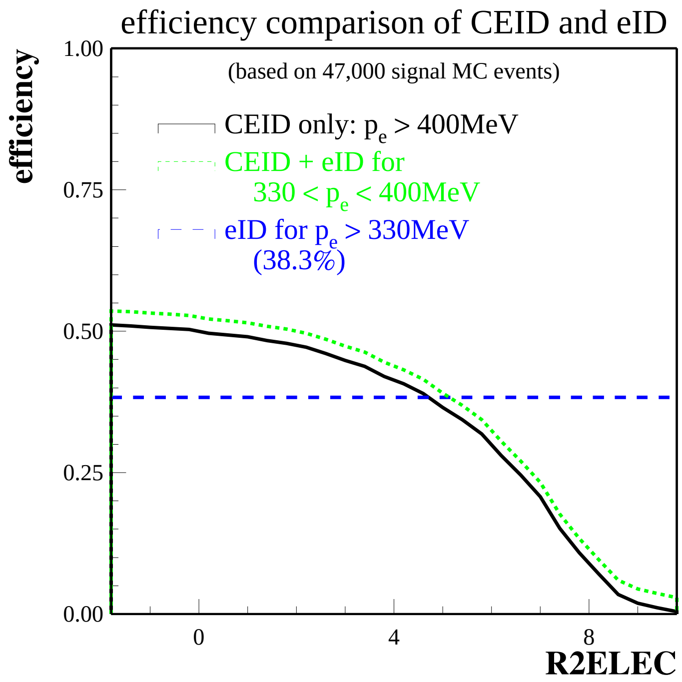

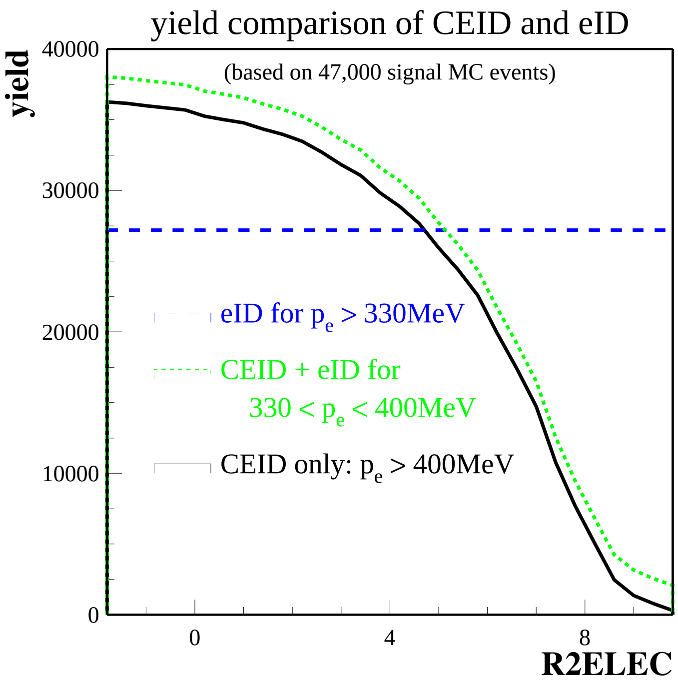

Figure B.2: Comparison of the efficiencies(top) and yields for the electron ID routine used in analysis(eID) and CEID. Included is also CEID plus eID for those electrons that fall below the minimum momentum for CEID, $p < 400$ MeV. Efficiencies include the factor of 64% for those electrons that pass the $p > 330$ MeV and track quality cuts.

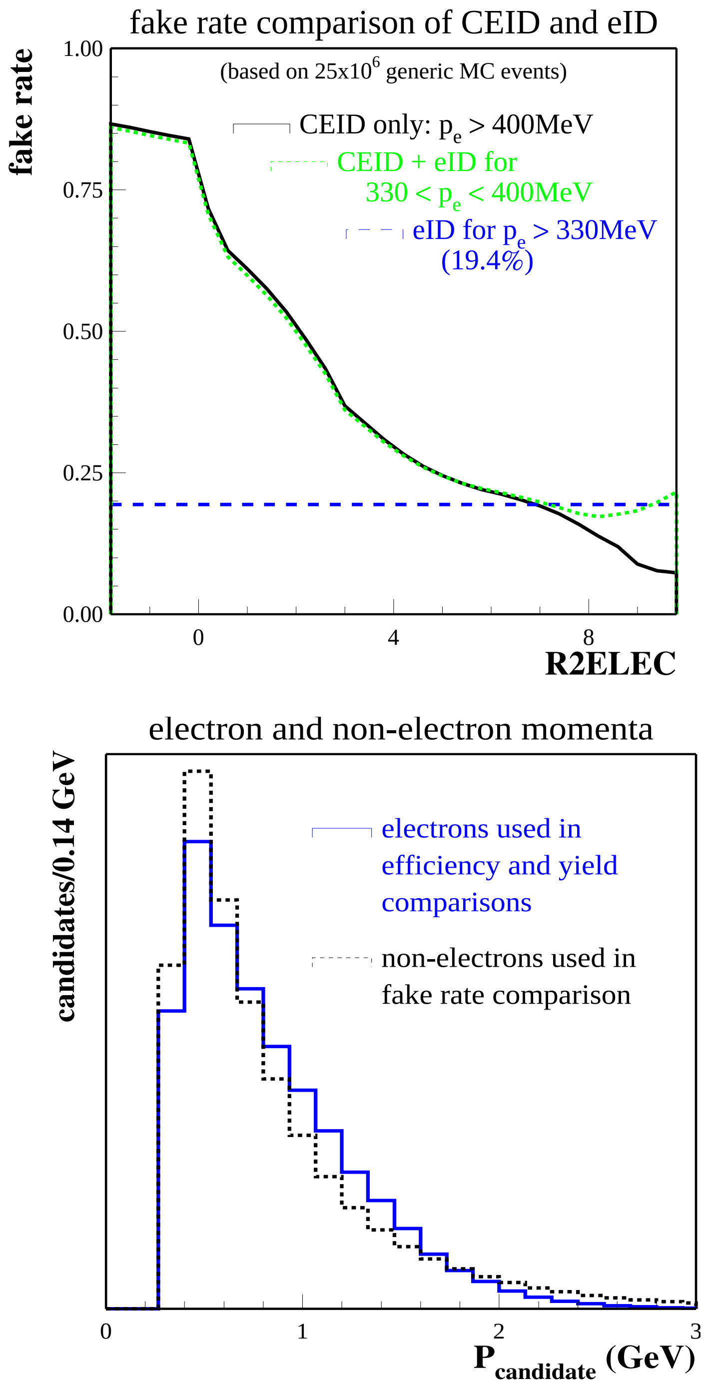

Figure B.3: Comparison of fake rates(top) for the electron ID routine used in analysis(eID) and CEID. Included is also CEID plus eID for those electrons that fall below the minimum momentum for CEID, $p < 400$ MeV. The bottom plot is a normalized comparison of the momenta of the electrons used in the efficiency and yield plots in Figure B.2 and the non-electrons used in the fake rate plot.

extremely important in discerning a WS signal. Also, due to the missing ν and the freedom this allows in event reconstruction, combinatorics play a significant role in the background profile. For these reasons, minimizing the electron fake rate is crucial. In most analyses, an R2ELEC value of 3.0 is taken when using CEID[54]. At R2ELEC = 3.0, CEID efficiency and yield are both 30% higher than eID but the fake rate of CEID is 80% higher. When $\eta_{\mathrm{CEID}} = \eta_{\mathrm{eID}}$ (R2ELEC≈5), the CEID fake rate is still roughly 25% higher than that of eID.

Bibliography

[1] Rolnick, W., *The Fundamental Particles and Their Interactions*, Addison-Wesley Publishing Company, Inc., (1994).

[2] Barnes, J., *Early Greek Philosophy*, Penquin Books, Ltd. (1987).

[3] Particle Data Group, D.E. Groom *et al.*, Eur. Phys. J. **C 15**, 1 (2000).

[4] E. Radermacher, Prog. Part. Nucl. Phys. **14**, 231 (1985).

[5] Frauenfelder, H., *Subatomic Physics*, Prentice-Hall, Inc. (1974).

[6] G. Arnison, *et al.*, Phys. Lett. **122B**, 103 (1983).

[7] Kane, G., *The Particle Garden*, Addison-Wesley Publishing Company, Inc. (1995).

[8] Griffiths, D., *Inroduction to Elementary Particles*, John Wiley & Sons, Inc. (1987).

[9] T.A. Armstrong, *et al.*, *Search for Charged Strange Quark Matter Produced in 11.5 A GeV/c Au + Pb Collisions*, **nucl-ex/9706004**.

[10] R. Bellwied, *Is Strangeness still interesting at RHIC?*, **nucl-ex/9810018**

[11] I. Bigi, *Studying CP Violation - Chances for a new alliance*, **hep-ph/0206261**.

[12] G. Buchalla, *Weak Decays Beyond Leading Logarithms*, **hep-ph/9512380**.

[13] A. Petrov, private communication.

[14] B. Winstein, *CP Violation in K^0 decays*, **hep-ph/9911026**.

[15] BABAR Collaboration, *Search for T and CP Violation in $B^0 - \overline{B}^0$ Mixing with Inclusive Dilepton Events*, **hep-ph/0202041**.

[16] BABAR Collaboration, *Measurements of Branching Fractions and CP-Violating Asymmetries in $B^0 \to \pi^+\pi^-, K^+\pi^-, K^+K^-$ Decays*, **hep-ph/0205082**.

[17] Belle Collaboration, *Observation of Mixing-induced CP Violation in the Neutral B Meson System*, **hep-ph/0202027**.

[18] Belle Collaboration, *Study of CP-Violating Asymmetries in $B^0 \to \pi^+\pi^-$ Decays*, **hep-ph/0204002**.

[19] O. Schneider, *$B^0 - \overline{B}^0$ mixing*, **hep-ph/0206171**.

[20] A.F. Falk, Y. Grossman, Z. Ligeti, A.A. Petrov, Phys. Rev. D **65**, 054034 (2002).

[21] CLEO Collaboration, R. Godang, *et al.*, Phys. Rev. Lett. **84**, 22 (2000).

[22] CLEO Collaboration, S.A. Dytman, *et al.*, Phys. Rev. D **64**, 111101 (2001).

[23] H. Nelson, *Compilation of $D^0 - \overline{D}^0$ Mixing Predictions*, **hep-ex/9908021**.

[24] S. Bergmann, *et al.*, *Lessons from CLEO and FOCUS Measurements of $D^0 - \overline{D}^0$ Mixing Parameters*, **hep-ph/0005181**.

[25] G. Raz, *Interpreting experimental bounds on $D^0 - \overline{D}^0$ mixing in the presence of CP violation*, **hep-ph/0205113**.

[26] J.D. Richman, Heavy-Quark Physics and CP Violation, Lectures at the 1997 Nato Advanced Study Institute, Les Houches, France. Elsevier Science B.V.(1998).

[27] CLEO Collaboration, S.E. Csorna, *et al.*, *Lifetime Differences, Direct CP Violation and Branching Fractions in D0 Meson Decays to K^+K^- and $\pi^+\pi^-$*, **hep-ex/0111024**.

[28] D. Asner, Thesis: "The Decay $D^0 \to K^+\pi^-$ and the Search for $D^0 - \overline{D}^0$ Mixing", University of California Santa Barbara.

[29] Fermilab E791 Collaboration: E. M. Aitala, *et al.*, *Branching Fractions for $D^0 \to K^+K^-$ and $D^0 \to \pi^+\pi^-$, and a Search for CP Violation in D^0 Decays*, **hep-ex/9711003**.

[30] FOCUS collaboration, *Search for CP violation in D^0 and D^+ decays* , **hep-ex/0005037**.

[31] CLEO Collaboration, $D^0 \to K_S^0\pi^+\pi^-$, submitted to Phys. Rev. Lett.

[32] CESR and CLEO Staff, CLNS **93/1265** (1993). http://www.lns.cornell.edu/public/CLNS/CLEO.html

[33] K.M. Reinish, *et al.*, *Structure of Reovirus Core Determined Via X-ray Crystallography*, Nature, Vol. **404**, 960-967 (2000).

[34] S. Desgreniers, *et al.*, *Studying Dense Materials by High Pressure X-ray Diffraction*, Phys. Rev. **B**, Vol 59, 8467(1999).

[35] Y. Kubota *et al.*, Nucl. Instrum. Methods Phys. Res. **A 320**, 66 (1992).

[36] A. Warburton, *et al.*, *Active cooling control of the CLEO detector using a hydrocarbon coolant farm*, Nucl. Instrum. Methods A **488** 451-465 (2002).

[37] T.S. Hill, Nucl. Instrum. Methods Phys. Res. **A 418**, 32 (1998); D. Peterson, Nucl. Phys. **B** (Proc. Suppl.) **54B**, 31 (1997).

[38] CLEO Collaboration, "The CLEOIII Detector: Design and Physics Goals", CLNS 94/1277.

[39] D. Asner, CBX98-26 (1998), CLEO internal document.

[40] K. Anikeev, *et al.*, *Scintillator Bar Quality Tests of the TOF System*, CDFR-5154, CDF internal note.

[41] D. Bortoletto, *et al.*, Nucl. Instrum. Methods Phys. Res. **A 320**, 114 (1992).

[42] C. Bebek, *et al.*, Nucl. Instrum. Methods Phys. Res. **A 302**, 261 (1991).

[43] R. Galik, CBX86-6 (1986); R. Galik, *et al*, CBX96-69 (1996), CLEO internal documents.

[44] K. Kinoshita, CBX90-23 (1990); R. Galik, *et al*, CBX90-30 (1990), CLEO internal documents.

[45] D. Cassel *et al.*, CSN83-333 (1983). CLEO internal document.

[46] http://lnson3.lns.cornell.edu/luminosity/luminosity.html

[47] F. Morrow, CSN90-297 (1990). CLEO internal document.

[48] A. Foland, CSN97-354 (1997). CLEO internal document.

[49] C. Prescott, CBX97-69 (1997). CLEO internal document.

[50] S. Roberts *et al.*, CBX96-103 (1996). CLEO internal document.

[51] R. Kutschke, CSN 95-340 (1995). CLEO internal document.

[52] R. Kutschke, CSN 94-335 (1994). CLEO internal document.

[53] D. Asner, CBX98-26 (1998). CLEO internal document.

[54] S-J. Lee, CBX01-57, (2001). CLEO internal document.

[55] H. Kroha, CBX 91-53, (1991). CLEO internal document.

[56] F. Morrow, CSN91-316, (1991). CLEO internal document.

[57] http://www-zeus.physik.uni-bonn.de/~brock/mn_fit.html

[58] CLEO Collaboration, S. Ahmed, *et al.*, Phys. Rev. Lett. **87**, 25 (2001).

[59] CLEO Collaboration, G. Brandenburg, *et al.*, Phys. Rev. Lett. **87**, 071802 (2001).

[60] D. Cinabro, K. Korbiak, *et al.*, Nucl. Instrum. Methods Phys. Res. **A 481**, 29-35 (2002).

[61] CLEO Collaboration, D. Cinabro *et al.*, Phys. Rev. E **57**, 1193 (1998).

[62] G. Moneti, private communication.

[63] E791 Collaboration, E.M. Aitala *et al.*, Phys. Rev. Lett. **77**, 2384 (1996).

[64] A. Petrov, private communication.

[65] B. Gittelman, CBX99-32 (1999). CLEO internal document.

ABSTRACT

A SEARCH FOR $D^0 - \overline{D}^0$ MIXING IN THE SEMILEPTONIC DECAY OF $D^0 \to K^* e\nu$

by

SEAN McGEE

December 2002

Advisor: Dr. David Cinabro

Major: Physics (High-Energy Experimental)

Degree: Doctor of Philosophy

Using the CLEOII.V dataset, we search for evidence of $D^0 - \overline{D}^0$ mixing through the decay of $D^0 \to K^* e\nu$ with the $K^{*\pm}$ decaying to $K^{*\pm} \to K^0_S \pi^\pm \to \pi^\pm\pi^\mp\pi^\pm$. A fit for wrong-sign events, $D^0 \to K^{*+} e^- \overline{\nu}$, gives an upper limit on $R_{mix} = \frac{N(D^0 \to \overline{D}^0 \to K^{*+} e^- \overline{\nu})}{N(D^0 \to K^{*-} e^+ \nu)}$ at a 95% C.L. of $< 0.86\%$.

AUTOBIOGRAPHICAL STATEMENT

SEAN McGEE

The year I was finishing my Bachelor's Degree in Chemical Engineering at Michigan State University, I happened upon a copy of Richard Feynman's biography "Surely You're Joking, Mr. Feynman!" while in the room of one of my housemates. It took no more than a few short chapters to become completely hooked. Much to the chagrin of my parents, upon graduation, instead of finding a career in Engineering, I decided to travel the country for a bit with the idea that I would eventually return to school to pursue a degree in Physics.

Upon returning to Michigan five years later, I discovered a fledgling High-Energy Physics group at Wayne State University that was willing to take me on as a graduate student. For most of my time as a student, I felt like some physics groupie who'd been lucky enough to receive a backstage pass. That eventually passed and now, 12 years later, I can see the fruit born of the idea that was planted long ago in my housemate's bedroom. Incidentally, that housemate is now my wife, so I blame her for all of it.